Journal of Manufacturing Processes 99 (2023) 848–897

Contents lists available at ScienceDirect

Journal of Manufacturing Processes

journal homepage: www.elsevier.com/locate/manpro

Review

On the application of in-situ monitoring systems and machine learning algorithms for developing quality assurance platforms in laser powder bed fusion: A review

Katayoon Taherkhani *, Osazee Ero, Farima Liravi, Sahar Toorandaz, Ehsan Toyserkani

Multi-scale Additive Manufacturing Lab, Department of Mechanical and Mechatronics Engineering, University of Waterloo, Canada

ARTICLE INFO

Keywords:
Additive manufacturing
Laser powder bed fusion
In-situ sensors
In-situ monitoring
Machine learning

ABSTRACT

Laser powder bed fusion (LPBF) is one class of metal additive manufacturing (AM) used to fabricate high-quality complex-shape components. This technology has significantly progressed over the last several years allowing the fabrication of high-value components for a broad range of applications, normally unmatched by other metal AM processes. However, the full adoption of LPBF to serial production is still challenging due to several barriers such as repeatability and reliability of final product quality. The main obstacle could be the high sensitivity of LPBF to environmental and process disturbances. Additionally, LPBF is governed by many process parameters. These factors profoundly affect the process, causing defects formation. To achieve high quality parts, trial and errors are conventionally carried out to obtain optimum parameters that result in good quality for a specific application. However, in recent years attention to the development of quality assurance platforms in LPBF has been the cornerstone of research and development. To this end, researchers have proceeded with three steps: 1) Gaining knowledge from the process by installing in-situ sensing equipment and collecting information from the process. 2) Understanding how the print parameters affect the process, analyzing in-situ datasets and developing defect detection algorithms, and 3) Developing real-time closed-loop control systems using the detection algorithms of Step 2 to automatically adjust the undesired phenomena in the process by changing the print parameters. Although valuable studies were published for the two first steps, the development of real-time controllers has remained challenging. Thus, this study aims to critically review the two first steps to provide insights for researchers into moving toward the development of the control system. In this study, in-situ sensing devices implemented in LPBF are categorized, explained in detail, and mapped to the literature. Then, a comprehensive review is conducted on the latest machine learning (ML) algorithms applied to the in-situ data of LPBF, such as supervised learning, unsupervised learning, and reinforcement learning. Additionally, a comprehensive discussion is provided on in-situ sensors and ML methods applied to LPBF. Lastly, this article specifies trends and future research outlook on this topic.

1. Introduction

The advent of additive manufacturing (AM) technology has played a transformational role in industrial application domains. AM is the process that involves constructing three-dimensional objects from digital three-dimensional (3D) models. During recent decades, significant advancement in AM has led to the use of its application in different industrial fields such as aerospace, automotive, biomedical, and energy [1].

AM has seven sub-categories, and one of them is laser powder bed fusion (LPBF), in which a laser beam scans a thin layer of material layer upon layer to selectively fuse regions of a powder bed based on the Computer-aided design (CAD) model or any 3D models [2,3].

LPBF process is a popular AM technology because of its versatility in choosing different types of materials [4–6]. Also, due to its ability to produce high-density and high-quality complex parts, LPBF is widely used in manufacturing Companies.

While the LPBF technique has significantly progressed, many fundamental challenges have remained unaddressed, like printing high-quality parts at mass production. Extensive research and various approaches were studied to improve the repeatability of the fabricated

* Corresponding author at: Multi-Scale Additive Manufacturing (MSAM) Lab, Department of Mechanical and Mechatronics Engineering, University of Waterloo, Waterloo, N2L 3G1, Ontario, Canada.
E-mail address: ktaherkhani@uwaterloo.ca (K. Taherkhani).

https://doi.org/10.1016/j.jmapro.2023.05.048
Received 21 November 2022; Received in revised form 9 May 2023; Accepted 13 May 2023
Available online 7 June 2023

Nomenclature

AI	Artificial Intelligence
AM	Additive Manufacturing
ANFIS	Adaptive Neuro-Fuzzy Inference System
ANN	Artificial Neural Network
CAD	Computer-Aided Design
CAE	Convolutional Auto Encoder
CCD	Charged-Coupled Device
CIS	Contact Image Sensor
CMOS	Complementary Metal-Oxide-Semiconductor
CNN	Convolutional Neural Networks
CT	Computed Tomography
CVAE	Conditional Variational Autoencoder
DBN	Deep Belief Network
DCB-MIR	Densely Connected Convolutional Block Architecture for Multimodal Image Regression
DCNN	Deep Convolutional Neural Network
DenseNet	Densely Connected Convolutional Networks
DL	Deep Learning
DoG	Difference of Gaussian
DSCNN	Dynamic Segmentation Convolutional Neural Networks
DSLR	Digital Single-Lens Reflex
DT	Decision Tree
DVRT	Differential Variable Reluctance Transducer
EMFs	Electric and Magnetic Fields
FBG	Fiber Bragg Grating
FF	Feed-Forward
FFT	Fast Fourier Transformation
FOV	Field of View
GD	Gradient Descent
GP	Gaussian Process
HoG	Histogram of Oriented Gradients
ICI	Inline Coherent Imaging
IDT	Interdigitated Transducers
IR	Infrared
KNN	K-nearest Neighbours
LPBF	Laser Powder-Bed Fusion
LSTM	Long Short-Term Memory
LWIR	Long Wavelength Infrared
MAPE	Mean Absolute Predictive Error
MB-RL	Model-Based Reinforcement Learning
MDP	Markov Decision Process
MF-RL	Model Free Reinforcement Learning
ML	Machine Learning
MLP	Multilayer Perceptron
MSE	Mean Squared Error
NIR	Near-Infrared
NN	Neural Network
OCT	Optical Coherence Tomography
OT	Optical Tomography
PCA	Principal Component Analysis
PI	Proportional–Integral
PID	Proportional–Integral–Derivative
PSD	Power Spectral Density
QA	Quality Assurance
ResNet	Residual Network
RF	Random Forest
RL	Reinforcement Learning
RMSE	Root Mean Square Error
RNN	Recurrent Neural Network
ROIs	Regions of Interest
SCNN	Spectral Convolutional Neural Networks
SeDANN	Sequential Decision Analysis Neural Network
SIFT	Scale-Invariant Feature Transform
SLM	Selective Laser Melting
SOM	Self-Organizing Map
SRAS	Spatially Resolved Acoustic Spectroscopy
ST-PCA	Spatially Weighted Principal Component Analysis
SVD	Singular Value Decomposition
SVM	Support Vector Machine
SWIR	Short-Wave Infrared
TIFF	Tagged Image File Format
TNN	Thresholding Neural Network
UTS	Ultimate Tensile Strength

parts through material characterization and post-processing; however, many issues have not been solved, such as predicting and controlling defects inside the products. One of the challenges to fabricate repeatable parts is the large number of parameters involved in the process that could affect its quality. Some parameters are not controllable, but they could also influence the quality of the process, such as gas flow pressure and powder uniformity. These parameters can adversely influence the quality, resulting in low repeatability. Quality assurance (QA) could be one solution to achieve high-quality AM products. The first step in moving toward QA is enhancing the knowledge of the process. As a result, in-situ sensors are installed to collect valuable datasets during the process, such as light intensity signals, melt pool images, acoustic signals, etc. Thus, real-time monitoring will help shed insight into the process and understand deviations in the process through data collected by sensors. However, gathering millions of data per layer creates a big data set that requires data mining algorithms for preprocessing and analyzing them. Thus, sensing, documenting, and analyzing the dataset during the real-time process are crucial. On the other hand, the quality assurance process must be automatically applied in a minimum amount of time. As a result, serial AM productions would be feasible in less time and at lower costs.

In this review article, all types of in-situ sensors with their characteristic either manually installed by researchers on their setups or commercially installed by LPBF vendors are categorized, discussed in-depth, and mapped to the literature in Section 2. In addition, these sensors are categorized into different groups, which is new compared to previously published papers. In the next section (Section 3), machine learning techniques applied to analyze the in-situ LPBF data will be explained in-depth with their hyper-parameters. In Section 4, a comprehensive discussion of Sections 2 and 3 is provided. Finally, the future research direction of LPBF will be covered in Section 5.

2. In-situ sensors used in LPBF for collecting real-time information

Various in-situ sensing sensors have been mounted in LPBF printers/machines to collect data from the process, which enhances knowledge about the process. In-situ sensors have been categorized into various groups based on their application and input/output [1]. The type of in-situ sensors and their mounting strategy will be discussed in Sections 2.1 and 2.2, respectively. In addition, in-situ commercial modules installed in LPBF printers/machines will be explained in Section 2.3.

2.1. Types

In-situ sensors have been classified into two major groups: radiative and non-radiative [1,7]. Fig. 1 represents the sub-categories of each group installed in LPBF.

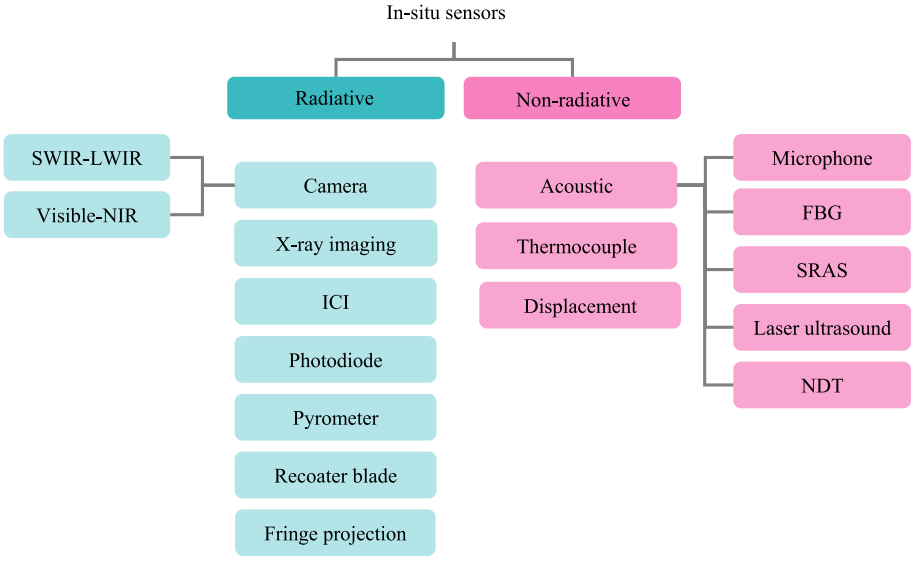

Fig. 1. Types of sensors used in LPBF to collect in-situ data.

- Radiative sensors sense/record radiative information. The radiative sensors can be classified based on their principles and outputs. According to Fig. 1, radiative sensors could be classified into the camera, X-ray imaging, inline coherent imaging (ICI), photodiode, pyrometer, the recoater blade sensor, and fringe projection [1].
- Non-radiative sensors could measure and then convert the physical behaviour of the process to an electrical signal. According to Fig. 1, non-radiative sensors used in LPBF could be categorized into the acoustic sensor, thermocouple, and displacement sensor [1].

Fig. 2 illustrates the volume of published papers using in-situ sensors. Since several studies have used multiple sensors in their work, all of them were considered separately in their category in Fig. 2. For example, if one paper highlighted the use of both the acoustic sensor and the photodiode, one publication was counted under the photodiode and one was considered under the acoustic sensor category in this figure. According to Fig. 2, most studies have used radiative sensors (281 papers), followed by non-radiative sensors (38 papers). Among radiative sensors, most of the papers are associated with the use of the visible-to-near-infrared (NIR) camera (127 papers), followed by the NIR to long-wavelength infrared (LWIR) camera (53 papers), X-ray imaging (31 papers), the photodiode (29 papers), the pyrometer (24 papers), the fringe projection (8 papers), the ICI (5 papers), and the scanner sensor (4 papers). Additionally, Fig. 2 implies that the use of non-radiative sensors is limited to the acoustic sensor (29 papers), thermocouple (4 papers), and displacement sensor (5 papers).

In the following sections, the detail of the sensors mentioned above will be discussed.

2.1.1. Radiative sensors

- Visible to near-infrared (NIR) camera

The visible to NIR camera is the most popular in-situ sensor to capture data from the LPBF process. This type of sensor has a wavelength range between 400 and 1100 (nm) that has been used to capture images/videos for monitoring different types of defects and the nature of the LPBF process, as listed in Table 1, which demonstrates the monitoring target of each published paper used visible to NIR camera.

Table 2 lists the characteristics of visible to NIR cameras used in some of the LPBF studies. For the first time, a group from K. U. Leuven University showed the feasibility of melt pool monitoring by installing a high-speed NIR CMOS camera on an in-house developed machine [8,10,23,52,53,115]. In Kruth's study, the CMOS camera was installed to capture 8-bit grey value images with 10 kHz frames per second [10]. The camera was also equipped with a custom-designed lens to provide a zooming function, leading to the elimination of f-Θ lens aberration. By combining the CMOS sensor and lens, images were captured with a field of view of 1280 × 1024 pixels [10,116]. However, 10 kHz frames per second means capturing data in every 100 μm × 100 μm with a 1000 mm/sec scan speed. But for instance, in cases with a melt pool radius of 150 μm, capturing images in every 100 μm results in inaccurate melt

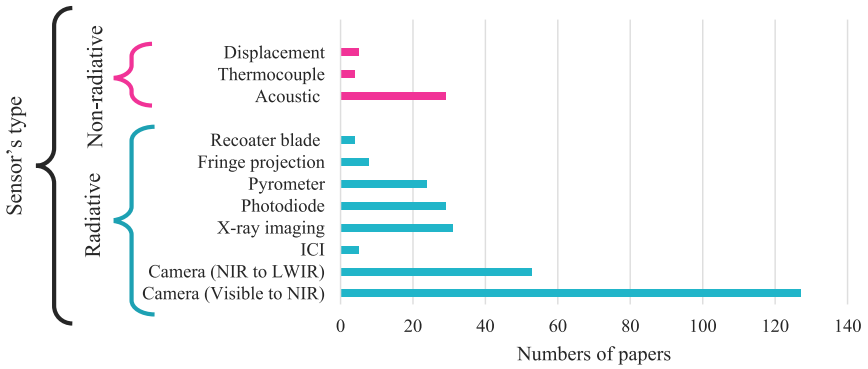

Fig. 2. Relative emphasis of in-situ sensors reported in the literature using LPBF.

Table 1
Mapping the literature on in-situ visible to the NIR camera installed in LPBF to monitor the process signature.

Prediction target	Publications	Prediction target	Publications
Geometry accuracy	[8–17]	Melt pool temperature	[18–22]
Deformation and distortion	[15,23]	Spatter and plume	[24–49]
Balling	[8,43,44,50,51]	Overheating	[51–57]
Delamination	[58,59]	Recoater blade defects	[59,60]
Porosity	[43,54,55,61–88]	Surface temperature	[89–91]
Overhang	[59,82,92–96]	Surface roughness	[17,97,98]
Melt pool dimensions	[10,12–15,20,22,39,99–106]	Anomaly detection	[55,107–110]
Track width continuity	[111,112]	Cooling rate	[22,113]
Residual heat effect	[114]		

pool information. As a result, Berumen et al. [8] added that the 10 kHz frame rate can be feasible by reducing the field of view, which resulted in capturing images every 10 μm. Recently, Kwon et al. [107] proposed a sophisticated method to capture images and document data. A high-speed camera was installed with a 1.3 M resolution on the WINFORSYS system. In the data acquisition system, images were cropped to 512 × 512 pixels with a frame rate of 2.5 kHz. To avoid delay errors between capturing images and saving their locations, the data acquisition system simultaneously gathered images and the location information. Then, locations were converted to the two 8-bit binary numbers (x and y- coordinates) and inserted into the upper left corner of corresponding images [107].

However, visible-NIR cameras face a fundamental challenge in capturing high-quality images in the dynamic melt pool [1]. To address the issue, many researchers used optical filters, illumination devices, calibration, and post-processing techniques. Niklas et al. [98] used a CMOS camera with 25 different Fabry Perot interference filters arranged in 5 × 5 mosaics to cover 2047 × 1088 pixels from the entire process. Additionally, an 875 nm short-pass filter was used to filter the spectral bands in the range of 600 to 875 nm. Jacobsmuhlen et al. [63] and Kleszczynski et al. [93] used an SVCam-hr29050, SVS-VISTEK monochrome CCD camera, while they applied different methods to improve the quality of captured images. Jacobsmuhlen et al. suggested the image calibration technique. Two lenses (tilt and shift) were added to the optical system (CCD camera Monochrome SVCamhr29050) to reduce the perspective distortion [63]. In Kleszczynski's method, indirect lighting sources were illustrated to capture high-resolution images [93]. Similarly, Gobert et al. [54] and Petrich et al. [55] coupled five illumination devices to the Nikon D800E DSLR camera to generate different lighting conditions. In total, eight images sequentially were taken from the process, which helped to extract features from different views. In addition, Demir et al. [117] and Vasileska et al. [105] proposed a solution to this challenge was placing lenses in the system. Demir et al. [117] used a three-lens configuration composed of two positive and a negative, whereas Vasileska et al. [105] installed a 120 mm focusing lens and optical filters to take images in the wavelength of 850–1000 nm.

Lane et al. [118] and Yeung et al. [114] added a linear translating lens (LTZ) to the high-speed Mikrotron EOSens 3CL camera. Lane et al. [106,119] upgraded the setup by using three different lenses: 1) linear translating lens (LTZ), 2) converging lens pair (CLP), and 3) custom imaging lenses (CIL). The laser reflected the light propagated through LTZ, CLP, and CIL lenses from an image to a camera. However, Yang et al. [99] and Fathizadan et al. [108] only used LTZ and CIL in their studies. Additionally, Scime et al. [43,44] and Zhang et al. [47] showed the effect of the post-processing technique to extract features from images. Scime et al. [44] convolved the captured images with six filters including Gaussian, Uniform Averaging Disk, difference of Gaussian (DoG), Oriented Edge Detectors, Oriented Line Detectors, and Streak Detectors. Each filter was used to detect specific features obtained by analyzing the convolved images. In another study, Scime et al. [43] calculated a scale-invariant feature transform (SIFT) of images captured during part fabrication under 36 process parameter combinations to create balling and keyhole porosity.

The visible-NIR camera has also been placed in machines to capture video imaging/ video from the process. Furumoto et al. [89] monitored the consolidation of metal by a mounted Photron FASTCAM SA5 high-speed camera to explore the effect of layer thickness. Caggiano et al. [65] used a DLSR camera with an additional zooming lens to capture video. In the next step, the video analysis was performed to extract images from deposition and scanning time. Then, features are extracted from the images through kernel-based convolution and non-linear activation. In another study, Colosimo et al. [59] used an Olympus I-speed 3 camera (CMOS sensor) with a 320 maximum number of frames in a video sequence. Then, videos were cropped out of any defocused areas. Zhang et al. [47] also applied the Kalman filter-based tracking method to the video images to extract the melt pool centroid location for obtaining information related to the melt pool, plume, and spatters. Spatter identification using video imaging was additionally discussed by, Tan et al. [26], Yin et al. [45], Nassar et al. [29], Bidare et al. [30,31], Andani et al. [33,120], Repossini et al. [40], Zheng et al. [49], Ly et al. [42], Liu et al. [34], and Yang et al. [39]. Besides spatter, Yang et al. [39] used video imaging to detect melt pool geometry, whereas Yuan et al. [111,112] and Gaikwad et al. [11] installed it to identify single-track features.

- Short-wave infrared (SWIR) to long-wavelength infrared (LWIR) camera

Infrared (IR) cameras work in the wavelength range of 1100 nm to 14 μm which are categorized into:

1) short-wave infrared (1 μm−3 μm),
2) mid-wave infrared (3 μm–5 μm), and
3) long-wavelength infrared (8 μm–14 μm).

Besides wavelength range, each type of camera has specific/unique features such as field of view, frame rate, and spatial resolution. The thermal/IR camera is mounted in LPBF systems to record the thermal behaviour of the process. Collected thermal images from IR are then analyzed to detect different process signatures as listed in Table 3 (e.g., spatter and plume [126–128], melt pool geometry [39,129,130], delamination [131,132], temperature measurement [133–137], dimension accuracy [138–140]).

Some of the IR cameras used in LPBF with their characteristics are summarized in Table 4. Bayle et al. [134] disclosed the use of NIR to LWIR camera (FLIR Phoenix RDAS with InSb sensor) to capture images from each 6.4 × 13.6 (mm^2) area with a spatial resolution of 100 μm/pixel. A 50 mm short-wavelength IR lens was also implemented to increase magnification and improve spatial. Final images were presented in the form of grey-scales which presented in black, white and grey colors in which the pixels convey light intensity information. Analyzing the captured grey-scales images resulted in the detection of ejected liquid droplets. The images were also used to disclose the trajectory, size, and speed of metal powder particles/droplets. Additionally, Doubenskaia et al. [139] expanded Bayle's study by extracting the shape of the melt pool from grey-scale images under the influence of different

Table 2
The characteristics of visible-NIR cameras manually placed in the LPBF system.

Reference	Camera type	Wavelength (nm)	Field of view (pixels)	Frame rate (kHz)	Spatial Resolution (μm/pixel)	Lens or filter	LPBF machine
Kleszczynski et al. [93]	CCD camera Monochrome SVCamhr29050	Unspecified	6842 × 6000	Not relevant to the application	19	A tilt and shift lens	EOS M270
Kwon et al. [107]	High-speed	450–900	Unspecified	2.5	20	–	WINFORSYS
Lane et al. [92] [106]	Mikrotron EOSens 3CL	850 ± 20	120 × 120	Up to 10	8	Linear Translating lens (LTZ) An 850 nm band-pass filter	AMMT
Yeung et al. [114]	Mikrotron EOSens 3CL	850 ± 20	120 × 120	Up to 10	8	An 850 nm band-pass filter	AMMT
Yang et al. [99,121] Fathizadan et al. [108] Milaat et al. [122]	Two cameras high resolution & high speed	850 ± 20	128 × 120	100	Unspecified	LTZ and CIL An 850 nm band-pass filter	AMMT
Mohr et al. [86]	DALSA Genie Nano-M4020	855–905	4112 × 3012	Unspecified	50	A 50 mm focus lenses linear translating z-lens	SLM280 HL
Yeung et al. [96]	High-speed CMOS	850 ± 20	120 × 120	100	8	An 850 nm band-pass filter	AMMT
Lane et al. [119]	Mikrotron EOSens 3CL	850 ± 20	120 × 120	Up to 10	8	1) Linear Translating lens 2) Converging Lens Pair 3) Custom Imaging Lenses	AMMT
Fox et al. [102]	High-speed CMOS	850 ± 40	256 × 256	30	20	An 850 nm band-pass filter	AMMT
Van Gestel [58]	PhotonFocus MV1-D1312-240-CL8 CMOS	400–1000	96 × 96	Up to 2	48 26 17	A focusing lens	In-house
Rombouts et al. [115]	High-speed CMOS	400–950	Unspecified	0.250	Unspecified	An optical filter	Concept Laser M3 Linear
Forien et al. [87]	MC1362, Mikrotron	780–820	256 × 256	1	17	A 780–820 nm bandpass filter	Aconity3D
Hooper [22]	Photron FASTCAM SA5	750–900	128 × 128	100	20	A 700–950 nm bandpass filter	Renishaw AM250
Demir et al. [117]	CCD camera and acA2500-14 gm	400–700 700–1100	1288 × 964	0.68	3.75 2.2	Three focus lenses	In-house
Snow et al. [66]	Nikon D800E	Unspecified	5000 × 5000 9000 × 4183	Not relevant to the application	50 15	A 28 mm *f*/2.8 A 105 mm *f*/2.8	3DSystems ProX 320
Vasileska et al. [105]	Ximea xiQ USB Vision	850–1000	1280 × 1204	1.2	14	A 120 mm focusing lens and two optical filters	In-house
Yuan et al. [111,112] Gaikwad et al. [11]	10-bit Mikrotron EOsens MC1362	400–720	256 × 256	1	14	–	Aconity3D
Jacobsmuhlen et al. [63,94]	CCD camera Monochrome SVCamhr29050	Unspecified	6000 × 4000	Not relevant to the application	25–35	A tilt and shift lens	EOS M 270
Kruth et al. [10] Craeghs et al. [23,53] Clijsters et al. [52] Berumen et al. [8]	NIR CMOS	400–1000	1280 × 1024	10	10	A custom-designed lens	In-house
Foster et al. [123] Gobert et al. [54] Petrich et al. [55]	Nikon D800E	Unspecified	5000 × 5000 9000 × 4183	Not relevant to the application	50 15	A 28 mm *f*/2.8 A 105 mm *f*/2.8	EOS M280
Barrett et al. [28]	FPS1000	470–625	1280 × 720	Unspecified	18–24	An 18 mm lens	EOS M290
Barrett et al. [27]	FPS 1000HD	Unspecified	1280 × 720	Unspecified	253	An 18 mm lens	EOS M290
Grasso et al. [57] Colosimo et al. [59] Yan et al. [124]	Olympus I-speed 3 camera	Unspecified	1280 × 1024	0.300	150	A SIGMA 105 mm macro lens	RenishawTM AM250
Colosimo et al. [72]	2 Cameras High resolution High-speed (An ISPEED 220)	Unspecified	Unspecified	>10 to 20 204	20 100	A 25-mm lens	In-house
Lu et al. [73,74]	Nikon D500 DLSR	Unspecified	~6000 × 4000	Unspecified	10–13	–	SLM 500HL
Scime et al. [43]	Photron FASTCAM Mini AX200	Unspecified	1024 × 1024	6.4	6.2	–	EOS M290

(*continued on next page*)

Table 2 (*continued*)

Reference	Camera type	Wavelength (nm)	Field of view (pixels)	Frame rate (kHz)	Spatial Resolution (μm/pixel)	Lens or filter	LPBF machine
Scime et al. [44,110]	Unspecified	Unspecified	1280 × 1024	Unspecified	290–340	–	EOS M290
Pagani et al. [15]	Unspecified	Unspecified	1280 × 1024	Unspecified	125	–	EOS M290
Ye et al. [32]	FASTCAM Min	700–1000	1024 × 1024	50	Unspecified	A 700- 1000 nm band-pass filter	In-house
Zhang et al. [51]	Photron Fastcam Mini AX200	250–800	1024 × 428	2	11.7	A cutoff filter	In-house
Zhang et al. [41]	Unspecified	350–800	~ 1026 × 1026	2	11.7	A 350–800 nm cut-off from	In-house
Eschner et al. [35,37]	Two Phantom v1210	Unspecified	512 × 256	60	40	A noise cancellation filter (Gaussian)	In-house
Yang et al. [38]	Pco.dimax HS4	Unspecified	2000 × 2000	up to 3	11	A narrow band-pass interference filter	Dimetal-100
Aminzadeh et al. [16,64,68]	8.8-megapixel USB digital	Unspecified	2160 × 4096	Unspecified	7	High focus lenses	In-house
Abdelrahman et al. [83] Gaikwad et al. [9] Imani et al. [84]	Nikon D800E	Unspecified	7360 × 4912	–	45, 67 (horizontally) 47, 88 (vertically)	–	EOS M280
Niklas et al. [98]	Ximea MQO22HG-IM-SM5X5-NIR	600–975	2047 × 1088	0.17	409 (horizontally) 217 (vertically)	A 25 different Fabry Perot interference filters 875 nm short-pass filter	In-house
Yin et al. [46]	Phantom® CMOS	810 ± 10	512 × 320	100	3.92 (horizontally) 5.70 (vertically)	A zoom lens system A Thorlabs® narrow bandpass filter of 808 nm	In-house
Furumoto et al. [89]	Photron FASTCAM SA5 model 1300 K C2 high-speed video	Unspecified	–	10	768–648	–	In-house
Tan et al. [26]	Pco.dimax HS4	290–1100	468 × 624	0.3	Unspecified	An optical filter	DiMetal-100
Yin et al. [45]	CMOS high-speed (Phantom v2012)	810 ± 10	512 × 320	100	3.92 (horizontally) 5.70 (vertically)	A zoom lens	In-house
Nassar et al. [29]	Phantom v1212 monochrome	405 ± 10	512 × 512	37.5	28	A Nikon 200 mm f/4 lens cut-off filter 405 nm bandpass filter	ProX-320
Bidare et al. [30]	Photron Fastcam Mini UX100 monochrome	400–1000	1280 × 616	8	10	C-mount QiOptiq Optem Fusion lens	In-house
Bidare et al. [31]	Phantom V2512 monochrome	632 ± 10	768 × 368	40	28	A band-pass filter	In-house
Andani et al. [33,120]	Fastcam 1024 PCI	Unspecified	1024 × 1024	6 3	17	–	SLM 280HL
Repossini et al. [40]	Olympus I-speed 3	400–700	1280 × 1024	1	150	Tamron SP 17–50 mm F/2.8 lens	Renishaw AM250
Liu et al. [34]	AOS SPRI-F	Unspecified	900 × 700	1	14	An optical filter	DiMetal-100
Zheng et al. [49]	i-SPEED 71 high-speed CMOS	300–1100	106 × 762	20	–	–	In-house
Ly et al. [42]	Photron SA-X2	400–1000	384 × 264	100	5	microscope optics (Mitutoyo 10×/0.28NA, Infinity K2)	In-house
Cheng et al. [103]	MCS640 LumaSense	670	640 × 480	0.06	65.9 (horizontally) 82.2 (vertically)	–	Concept Laser M2
Yang et al. [39]	High-speed Photron	Unspecified	1024 × 256 512 × 128	2–10-24	Unspecified	–	EOS M270
Pacher et al. [101]	Ximea xiQ USB Vision	350–1000	1280 × 1024	1.2	14	A 1000 nm short pass filter A 650 ± 40 nm bandpass filter A 120 mm focusing lens	In-house
Mazzoleni et al. [19,20]	Ximea xiQ USB Vision	400–1000	304 × 304	1.2	14	A 1000 nm short pass filter A 650 ± 40 nm bandpass filter A 120 mm focusing lens	In-house
Vasileska et al. [105]	Ximea xiQ USB Vision	350–1000	1280 × 1024	1.2	14	A 1000 nm short pass filter An 850 nm bandpass filter A 120 mm focusing lens	In-house
Bertoli et al. [113]	Shimadzu HPV-X	808 ± 10	Unspecified	250	Unspecified	An 808 band-pass filter	In-house
Mahmoudi et al. [109]	two high-resolution CMOS	Unspecified	1300 × 1000	0.250	24	–	ProX™ DMP 100

(*continued on next page*)

Table 2 (*continued*)

Reference	Camera type	Wavelength (nm)	Field of view (pixels)	Frame rate (kHz)	Spatial Resolution (μm/pixel)	Lens or filter	LPBF machine
Vallabh et al. [18]	Nova S12, Photron	550 620	128 × 48	30	20	Optical bandpass filters	EOS M290
Li et al. [61]	IDT: NX4-S3	Unspecified	128 × 128	10	13.68	–	In-house
Ma et al. [21]	High-speed Dual-wavelength	780 ± 2 905 ± 2	1024 × 1024	3	20	Two narrow-band filters	In-house
Lin et al. [24]	Mikrotron EoSenS 3CL	850 nm	128 × 128	2	8	Bandpass filter	AMMT
W. Zhang et al. [25]	Phantom v2512 CMOS	900	1280 × 800	up to 1000	14.6	Short pass filter	In-house
Vasileska et al. [125]	Ximea xiQ USB Vision	850–1000	1280 × 1204	1.2	14	FEL0850 optical filter	In-house
Feng et al. [78]	sCMOS	900	2000 × 2000	10	125	Band-pass filter	EOS M290
Gaikwad et al. [79]	Photron FASTCAM SA	700–950	128 × 128	100	25	Bandpass optical filter	In-house
Williams et al. [80]	ATLAS system	950	128 × 128	20	31.5	Narrow band pass filter	In-house

Table 3
Mapping the literature on in-situ IR camera installed in LPBF to monitor the process signature.

Prediction target	Publications	Prediction target	Publications
Geometry accuracy	[138–140]	Temperature measurement	[133–137]
Cooling rate	[130,137,141,142]	Surface roughness	[127,143]
Delamination	[131,132]	Deformation and distortion	[144,145]
Porosity	[71,72,76,77,126,127,146–150]	Emissivity	[133,151]
Overhang	[152]	Inhomogeneity	[148]
Melt pool dimensions	[39,129,130,143,153]	Crack	[128]
Spatter and plume	[126–128,154,155]	Stress analysis	[149]
Overheating	[156]	Effect of print parameters	[157]

parameters such as scanning velocity, laser power, beam diameter, and laser influence.

Krauss et al. [148,158] and Schilp et al. [144] placed an Infratec Variocam hr head IR camera working in the wavelength ranges of 8–14 μm on EOS M270. Also, an uncooled micro-bolometer detector and a telephoto lens with a resolution of 640 × 480 pixels were added to the optical system to allow for a field of view (FOV) of 18° (horizontal) and 13.5° (vertical). The in-situ information was analyzed to monitor temperature gradients and thermal inhomogeneity [144].

Thombansen et al. [156] proposed a new approach to increase the frame rate of the IR camera image acquisition system. In the first step, the images were taken from the area of 150 × 150 (mm^2) with 1000 × 1000 pixels. To this end, 150 images should be captured per second, which is not practically feasible. Accordingly, the IR imaging system was coupled with the processing laser by which new images were captured with the frame rate of 1 kHz. Furthermore, focused detection was discussed to take images with a temporal resolution of 10 μs, which continuously monitored the temperature.

Moylan et al. [147] explained the use of infrared (IR) thermography by converting the emissivity and imaged temperatures to true temperatures for the entire build plate, which could validate the high-fidelity multi-physics models. Lane et al. [95,137] completed Moylan's study by analyzing the high-temperature melt pool region and correlating it to the physics of the process. In addition, the NIST image calibration function was applied to avoid any aberrations [159]. Similar hardware was used in Heigel's research [130,145].

Besides, Baumgartl et al. [131] captured video imaging by installing the PYROVIEW thermographic camera above the process chamber of the SLM 280HL system at an angle of 60° to the substrate plate. The IR camera captured in-situ images with a spectrum range of 4.8–5.2 μm. Up to 50 images were captured per second, and overall, 4,314 RGB colour images were taken from the process. Images were then used to extract melt pool geometry, delamination, and spatters.

Thermal video imaging was analyzed to monitor temperature by Plotnikov et al. [136], Alldredge et al. [142], Jalalahmadi et al. [154], Lough et al. [150], Mohr et al. [86], Williams et al. [71], Foster et al. [127], and Bamberg et al. [76], whereas in Yakout's study [132], video imaging was used to detect spatter. An ImageIR® 8300 hp., Infratech thermal camera was placed to capture video imaging in this study. The hardware system includes three components: 1) an InSb detector, 2) an F/6 lens set, and 3) an infrared observing window of a germanium wafer. The InSb detector was sensitive to the wavelength ranges of 2.0 μm to 5.7 μm. An F/6 lens set captured thermal images with a minimum distance of 300 mm and with a field of view of 58 × 46 mm. Finally, a germanium wafer was placed to filter out the spatter. Additionally, customized thermal imaging software (IRBIS 3, Infratech) was offered for temperature calibration [132].

- Inline coherent imaging (ICI)

Inline coherent imaging defines as a category of optical coherence tomography (OCT). Fig. 3 demonstrates the schematic of the OCT module in which, first, a low-coherence super-luminescent diode (SLD) generates the fiber-coupled broadband light. The generated light transfers through an isolator to prevent unwanted back reflection, and it is then divided by a 50/50 coupler into two parts to pass into the sample arm and reference arm.

(i) The sample arm's light co-axially transfers to the powder bed surface and is back-reflected to the spectrometer phase.
(ii) The reference arm's light transfers to a polarization controller, collimator, and dispersion-matching elements for compensating the change in polarization and dispersion. Then, it will be co-axially back-reflected into the spectrometer phase.

The back-reflected lights are recombined by the splitter, transmitted through the collimator and dispersive elements (TG), and received by the spectrometer. Since path differences could result in different interferences, the camera is used to record and send the interferences spectrometer to the computer for calculating the intensity map

Table 4
The characteristics of IR/thermal cameras placed in the LPBF system.

Reference	Camera type	Wavelength range (μm)	Field of view (pixels)	Frame rate (Hz)	Spatial resolution (μm/pixel)	Lens or filter	LPBF machine
Thombansen et al. [156]	Unspecified	1.03–2.1	256 × 256	1000	150	A focusing lens	In-house
Mohr et al. [138]	ImageIR8300	2–5	160 × 224	600	420	–	SLM280 HL
Mohr et al. [133]	ImageIR8300	2–5	160 × 224	100	420	A 25 mm objective lens	SLM280HL
Mohr et al. [141]	ImageIR8300	2–5	160 × 200	600	420	A 25 mm objective lens	SLM280HL
Mohr et al. [86]	ImageIR8300	2–5	192 × 176	900	100	A 100 mm focal lens	SLM280HL
Yakout et al. [132]	ImageIR8300	2–5.7	640 × 512	200	15	An F/6 lens set	OmniSint 160 (OmniTek)
Jalalahmadi et al. [154]	Unspecified	8–12	128 × 128	1313	760	25 mm focal length f/2.3 lens	EOS M290
Baumgartl et al. [131]	PYROVIEW 640G/50 Hz/ 25° × 19°/compact	4.8–5.2	1280 × 768	50	Unspecified	–	SLM 280 L
Doubenskaia et al. [139] Bayle et al. [134]	FLIR Phoenix RDAS with InSb sensor	3–5	64 × 136	2031–3556	100	A 25 mm lens	Phenix PM100
Yavari et al. [135]	FLIR A35X	7.5–13	320 × 256	60	~31.6	–	Renishaw AM250
Plotnikov et al. [136]	FLIR A65	3–12	640 × 512	30	7.5–13	–	EOS M290
Foster et al. [127]	FLIR SC8200	3–5	Unspecified	346.7	100	A 25 mm germanium lens	Renishaw AM250
McNeil et al. [128]	FLIR SC8200	3–5	10 × 10	173	100	A 25 mm germanium lens	Renishaw AM250
Lough et al. [150]	FLIR SC6201	0.9–1.7	80 × 80	2500	130	–	Renishaw AM250
Lough et al. [149]	LIR SC6201	0.9–1.7	80 × 80	2500	130–135	A 1.45 ± 0.05 μm filter	Renishaw AM250
Williams et al. [71]	FLIR A35	Unspecified	320 × 256	60	~31.6	–	Renishaw AM250
Raplee et al. [126]	FLIR SC8200	3–5	Unspecified	742 500	350, 200 (horizontally) 250, 167 (vertically)	A 25 mm germanium lens	Renishaw AM250
Molnar et al. [152]	IRC 912	1.35–1.6	360 × 126	1800	33.5 (horizontally) 49.8 (vertically)	A band-pass filter	EOSM270
Heigel et al. [130,145]	IRC 912	1.35–1.6	360 × 126	1800	34 (horizontally) 52 (vertically)	A band-pass filter	AMMT
Colosimo et al. [72]	FLIR X6900sc	3–5	Unspecified	1004	200	–	In-house
Lane et al. [137]	Extended sensitivity range InSb camera	1–2.7	360 × 128	1800	36 (horizontally) 53.3 (vertically)	A 50 mm IR lens and filters	EOS M270
Ozel et al. [160]	HFR	1.35–1.6	360 × 128	2000 10,000 24,000	36	A thermography filter	EOS M270
Yang et al. [39]	IFR	1.35–1.6	360 × 128	1800	36	–	EOS M270
Liu et al. [157]	FLIR A655sc	7.5–14.0	640 × 480	200	325	ZnSe window	Renishaw AM250
Oster et al. [161]	Goldeye CL-033 TEC1	SWIR	640 × 512	301	100	–	SLM 280 HL
Lough et al. [162]	A FLIR SC6201	SWIR	640 × 512	2585	130 (horizontally) 135 (vertically)	A bandpass filter	Renishaw AM250
Krauss et al. [148,158] Schilp et al. [144]	Infratec Variocam hr head	8–14	640 × 480	50	250	A 50 mm telephoto lens	EOS M270
Estalaki et al. [146]	FLIR SC6201	1.45 ± 0.05	640 × 512	2500	135	Band-pass filter	Renishaw AM250
H. Zhang et al. [163]	Dual wavelength	0.55, 0.62	128 × 48	30	20	Band-pass filter	EOS M290

[164–167].

Various versions of OCT were introduced in the time domain [168,169] and Fourier domain [170,171]. Each domain has its features and application, but the Fourier domain OCT is less sensitive to noise than the time-domain one [172]. Inline coherent imaging (ICI) is one category of inline SD Fourier domain OCT technique mainly applied in biomedical [164]. The ICI technique was placed in the LPBF systems to predict the melt pool dimension [173], geometry accuracy [166], overhang structure [167], inhomogeneity [174], and distortion [174].

Neef et al. [174] installed the PRECITED IDM sensor on EOS M250 to investigate topology information of powder and melted material. Firstly, the mentioned ICI system recorded the sequential surface topology. Then, the captured ICI images were explored to detect the distortion. This study proposed a possible method to evaluate the layer surface quality; however, the measuring range of sensors was established experimentally by first providing a profile of distance to the deflection mirror. The accidental point of measuring for a single scan in the y-axis direction. The measuring range enabling covering of the maximum lateral region while minimizing the difference between the two distance parameters was used for measuring the range selection. Then, Kanko et al. [166] and Fleming et al. [175] expanded the approach by capturing dynamic data on microsecond timescales. In Kanko's study, monitoring the geometry and molten pool dimension was investigated during the change of process parameters. The results disclosed that

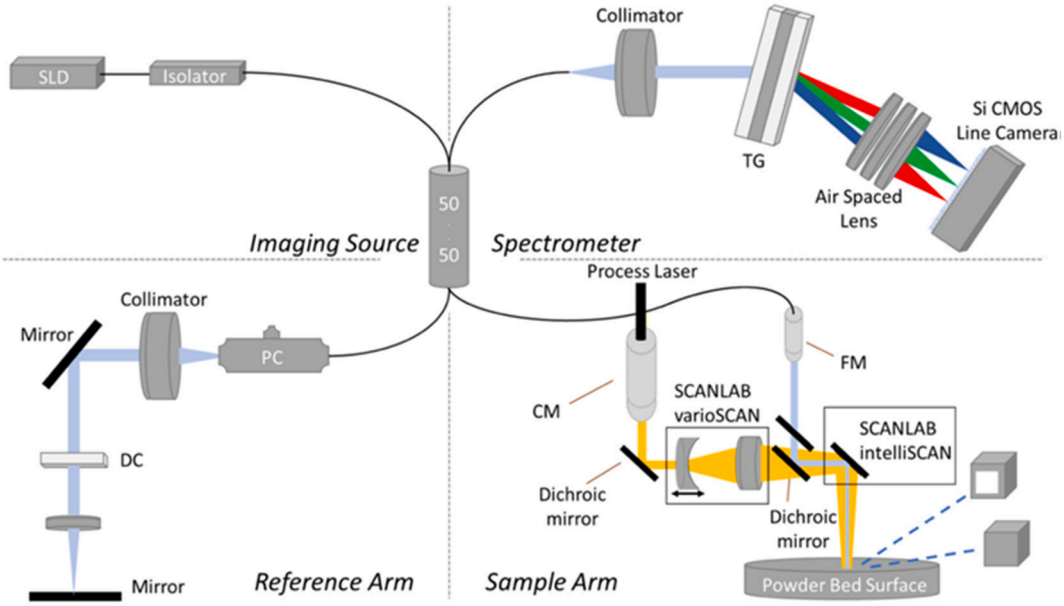

Fig. 3. The OCT module.
(Source: Republished with permission of Elsevier, from [167])

monitoring the height and longitudinal size of the melt pool, as well as light intensity, led to the prediction of porosity, balling, and surface irregularities [166]. However, Fleming et al. used ICI to monitor surface roughness. Additionally, surface roughness was measured by DePond et al. [167] by visualizing the effect of laser power on surface roughness and unsupported overhang structure. Lough et al. [173] also showed the use of optical emission spectroscopy (OES) hardware to monitor melt pool dimension.

- X-ray diffraction imaging

In X-ray diffraction imaging, firstly, the energy source produces an X-ray beam filtered to reduce the scatter and low-energy rays and maximize high-energy rays. The filtered beam is then passed through the objects and reflected. The reflected beam produces a diffraction pattern detected by photographic film [176].

The application of X-ray imaging sensors in LPBF was explored by Zhao et al. [177], Sinclair et al. [178], Leung et al. [179], Calta et al. [180,181], Lhuissier et al. [182], Gould et al. [183], Martin et al. [184], Forien et al. [87], Guo et al. [185], and Chen et al. [186]. For the first time, Zhao [177] used X-ray imaging in the LPBF process in which Harmonic polychromatic X-rays passed through the sample, as demonstrated in Fig. 4. The diffracted signal was then captured by the diffraction detector. The analyzed X-ray imaging disclosed the effect of laser power on the melt pool dimension, keyhole mode, and particle motions. Also, the sensory data revealed information about the cooling and phase transformation rates.

Other studies used a polychromatic X-ray beam to penetrate the sample, and the transmitted signal was converted to visible light, which was then recorded by a high-speed camera. The images were mostly studied to identify porosity, spatter, deformation, and stress analysis, as mapped to the literature in Table 5.

More information about the Harmonic polychromatic X-rays energy, X-ray detector type, and any additional filters that were mounted in the LPBF system are summarized in Table 6.

- Photodiode

A photodiode is a light-sensitive semiconductor diode that produces an electrical current when it absorbs photons. Photodiodes are commonly used in optical communication [206,207] and photography [208,209]. The photodiode also has applications in the LPBF process to sense thermal radiation and light emission. The thermal information is analyzed to detect various process signatures as listed in Table 7.

For the first time, Kruth et al. [10] and Berumen et al. [8] installed the photodiode to monitor reflected intensity signals by collecting the emitted mean radiation from the melt pool in the visible- NIR wavelength ranges. The combination of photodiode and camera provided complementary information to study the dimensional accuracy. Clijsters et al. [52], Craeghs et al. [53], and Van Gestel [58] placed the photodiode and the camera to monitor overheating. Van Gestel [58] installed a Thorlabs PDA36A photodiode and two CMOS cameras to capture light intensity signals and melt pool images, respectively. The captured information was then analyzed to reveal information about melt pool size, intensity, and shape [58]. Additionally, in other applications, the photodiode was set up to discuss the plasma behaviour of the melt pool. Okaro et al. [219] and Jayasinghe et al. [212] disclosed how three photodiodes' complex arrangements could monitor thermal radiation and plasma emission. The module was comprised of three photodiodes with a 100 kHz sampling time. The first photodiode (700–1050 nm) was installed to detect plasma emission, the second photodiode (1080–1700 nm) was used to detect thermal radiation, and the third photodiode was placed to measure the intensity of the laser beam. Table 8 lists the wavelength and sampling time of photodiodes used in the LPBF literature. Also, Table 8 specifies any additional filters/lenses added to the in-situ monitoring system.

- Pyrometer

A pyrometer is a remote-sensing device that could measure the temperature by receiving thermal radiation from an object. Each pyrometer consists of an optical system and a detector. Firstly, the optical system collects the light emitted from the targeted objects. After that, the light is conveyed to the sensitive detector [224]. By Stefan-Boltzmann's law, thermal radiation received by the detector is used to calculate the final temperature of the target. Pyrometer was originally developed to collect radiation in a specific bandwidth called a one-colour pyrometer.

Since, in LPBF, the material is fused by thermal energy, many experts have focused on the application of the pyrometer to measure

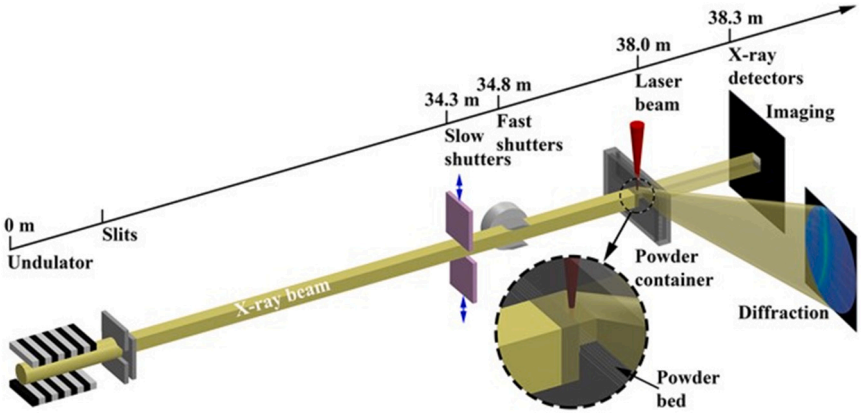

Fig. 4. The schematic of the high-speed X-ray imaging [177].
(Open access CC BY 4.0 license)

Table 5
Mapping the literature on in-situ X-ray imaging installed in LPBF to monitor the process signature.

Prediction target	Publications	Prediction target	Publications
Geometry accuracy	[177,187]	Deformation and distortion	[188,189]
Spatter and plume	[179,183,186,190–196]	Cooling rate	[177]
Porosity	[87,129,177–186,190,195,197–202]	Stress analysis	[203,204]
Melt pool dimension	[129,183]	Melting behaviour	[205]

Table 6
The detailed characteristics of X-ray imaging implemented in the LPBF system.

References	Harmonic polychromatic X-rays energy (keV)	X-ray detector type	Additional lens	LPBF machine
Zhao et al. [177] Guo et al. [185,193,199]	24.4	High-speed camera	A relay lens An objective lens	In-house
Bidare et al. [187]	Unspecified	Ophir Spiricon SP928	–	In-house
Calta et al. [180,201]	24	pco.dimax S4CMOS	Infinity-corrected tube lens	In-house
Wakai et al. [129]	Unspecified	PCI2000S CCD	–	In-house
Calta et al. [181]	24	PIMAX4:1024i iCCD	Long working distance objective lens tube lens	In-house
Leung et al. [179]	55	High-speed CMOS	3 Custom-made optics	In-house
Leung et al. [195]	55	Miro 310 M	Custom-made optics	In-house
Lhuissier et al. [182]	95	pco.edge 5.5 sCMOS	Mitutoyo long-working distance Objectives	In-house
Gould et al. [183]	25.4	Visible: Photron FastCam SA-Z IR: Telops Fast M3K	– A magnification lens	In-house
Martin et al. [184]	7.4	Photron SA-X2	An objective lens	In-house
Chen et al. [186]	30	Photron FASTCAM SA-Z	4 × magnification long working distance objective lens	In-house
Paulson et al. [197]	25	IR: Telops Fast M3K	1× magnification lens	In-house
Uhlmann et al. [203]	98.02	Perkin-Elmer XRD1621 2D detector	–	Aconity MINI
Schmeiser et al. [204]	98.02	Perkin-Elmer XRD1621	–	In-house
Vallejos et al. [188]	Unspecified	PerkinElmer XRD 1621	–	SLM 280
Choo et al. [189]	115	Perkin-Elmer XRD 1621	–	SLM 280
Parab et al. [190]	24.4	UI-5240CP-M-GL CCD	An objective lens	In-house
Hojjatzadeh et al. [198]	24	Photron FastCam SA-Z	A 10× objective lens	In-house
Bobel et al. [200]	24.4	Photron FastCam SA-Z	An objective lens	In-house
Sinclair et al. [178]	30	STCAM SA-Z	A 4× magnification	In-house
Sun et al. [191]	55.6	PILATUS3X 2 M CdTe pixel array	–	In-house
Voisin et al. [192]	100.135	GE amorphous silicon area detector	–	Concept Laser M2
Hojjatzadeh et al. [202]	24.7–25.3	High-speed	A 10× magnification	In-house
A. Young et al. [196]	24	High-speed Photron FastCAM SA-Z	–	In-house

temperature, such as Islam et al. [50], Bayle et al. [134], Forien et al. [87], Haines et al. [225], Pavlov et al. [226], Zouhri et al. [227], and Renken et al. [228].

For example, Gaikwad et al. [11] used the infrared pyrometer to capture data with a sampling rate of 100 kHz. Bayle et al. [134] explored the use of a pyrometer with a temperature range, wavelength range, spatial resolution, and sampling time of 1100–3500 K, 1.001–1.573 μm, 800 μm, and 50 μs, respectively. Haines et al. [225] used a pyrometer with wavelength ranges of 1.58 to 1.80 μm. Islam et al. [50] reported the placement of a pyrometer outside the optical path with a diameter range

Table 7
Mapping the literature on the in-situ photodiode of LPBF to monitor the process signature.

Prediction target	Publications	Prediction target	Publications
Geometry accuracy	[8,10,210,211]	Density measurement	[212]
Porosity	[117,213–218]	Balling	[58]
Overheating	[52,53,58]	Drift layer	[82]
Abnormal process	[213,219]	Emissivity	[151]
Hardness	[220]		

of 15 mm. Renken et al. [228] and Pavlov et al. [226] placed the pyrometer with a shorter wavelength. Renken et al. [228] used the Optris SN 8029001 pyrometer with a wavelength range from 850 to 1000 nm, and Pavlov et al. [226] installed a two-colour pyrometer with a wavelength range of 900–1200 nm.

Although the use of the one-colour pyrometer provides valuable information about the process, collecting an accurate temperature could be challenging in some situations, for instance, when:

- Objects that are too small to fill the perspective view,
- The existence of dust, plume, or spatters in the environment that blocks the line of sight, and
- The change of the process zone emissivity when an alloy or surface condition changes that require re-calibration of the pyrometer.

Thus, to overcome these problems, a two-colour pyrometer, also called a ratio pyrometer, was introduced [229]. It employs two detectors, operating at two different wavelengths λ_1 and λ_2 to detect the same target. The ratio of the thermal radiation collected at these two wavelengths is given, in the Wien approximation of the Planck radiation law, which relates a blackbody's temperature to the maximum intensity of its thermal radiation. It is derived from the Planck radiation law which describes the spectral distribution of the intensity of thermal radiation emitted by a blackbody at different wavelengths. The Wien approximation is obtained by considering the Planck radiation law behaviour for short wavelengths, where the exponential term in the formula plays a significant role [230]. It can be shown that this ratio is a function of temperature and is independent of emissivity [231]. In LPBF, the application of the two-colour pyrometer was investigated by Gutknecht et al. [228], Furumoto et al. [90,232], Mitchell et al. [233], Wakai et al. [129], Smoqi et al. [234], Vallabh et al. [18], and Hooper [22]. Furumoto et al. [90,232] placed a two-colour pyrometer with two infrared detectors: 1) an InAs detector with sensitivity ranges of 1 μm- 3 μm and 2) an InSb detector with sensitivity ranges of 3 μm- 5.5 μm. In Gutknecht's study, a two-colour pyrometer with a wavelength range of 1450–1800 nm was placed [235], whereas Smoqi et al. [234] installed the Stratonics two-colour pyrometer with the wavelength of $\lambda_1 = 720$ nm and $\lambda_2 = 900$ nm. Although the study of Hooper [22], and Vallabh et al. [18] were mentioned in the visible- NIR section, their setup was based on the two-colour pyrometer. Hooper [22] implemented a two-wavelength imaging setup based on the pyrometer to measure accurate temperature where unknown emissivity was involved like during the transition of material from powder to liquid. With this setup, Hooper [22] was able to collect data at a high frame rate of 100,000 fps; however, the recording time was limited to 3 s. Then, Vallabh et al. [18] address this challenge by developing a new system to record data from 50 layers at high framerates of >30,000 fps during the fabrication of fatigue specimens. Vallabh's system included a 50:50 beam splitter to divide the light path into two different directions for capturing melt pool images at two wavelengths ($\lambda 1 = 550$ nm and $\lambda 2 = 620$ nm).

As above-mentioned, a pyrometer is typically designed to measure temperature; however, other process signatures were also predicted using a pyrometer, as presented in Table 9.

In the literature, the adoption of a pyrometer and other sensors has been discussed to detect overheating [156], porosity [233], and overhang structures [237]. Thombansen et al. [156] used the combination of a pyrometer and IR camera to generate a melt pool temperature map, and then the map was interpreted to predict overheating. Chivel et al. [237] installed a pyrometer and a CCD camera for recording the temperature, resulting in an understanding of the impact of temperature on the overheating and overhang layer. Mitchell et al. [233] installed the Stratonics two-colour pyrometer to record intensity light at a wavelength of 750 nm and 900 nm, which was finally analyzed to identify porosity. Table 10 will specify the characteristics of pyrometers which were used in the LPBF studies.

- Fringe projection

A fringe projection is a non-contact technique to measure surface 3D information. A fringe projection includes a projector and camera(s). First, the projector produces a sequence of fringe patterns that are projected on the object's surface. Then, the irradiated fringe patterns are captured by the camera(s) from different views. Additionally, two

Table 8
The sampling frequency and wavelength of photodiodes used in the LPBF studies, as well as any additional filters/lens.

References	Wavelength (nm)	Sampling time (kHz)	Additional equipment	LPBF machine
Kruth et al. [10] Berumen et al. [8]	400–1000	10	–	In-house
Van Gestel [58]	350–1100	100	Amplifier 0–70 (dB)	In-house
Okaro et al. [219] Jayasinghe et al. [212] Egan et al. [213]	700–1050 1080–1700	100	Focusing lens	Renishaw 500 M
Taherkhani et al. [214] Schwerz et al. [216]	750–900	60	–	EOS M290
Clijsters et al. [52]	780–950	10,000	Optical filter	In-house
Craeghs et al. [53]	400–900	20	Optical filter	In-house
Demir et al. [117]	800–1700	1000	Optical filter	In-house
Nadipalli et al. [210]	400–1100 1200–1800	100	– Low pass filter (DMLP1180)	In-house
Yadav et al. [82]	NIR	100	Focus lens	SLM 280
Dunbar et al. [151] Montazeri et al. [221]	520–530	100	520 and 530 band-pass filters	ProX 200
Bisht et al. [211] Coeck et al. [218]	1150–1800	Unspecified	1150 nm high-pass filter	In-house
Artzt et al. [222]	NIR	100	–	SLM 280
Pandiyan et al. [223]	350–1100 800–1700 visible and NIR	3000	The bandpass filter of 1070 nm ± 2 nm low-pass optical filter a short-pass optical filter	In-house
Zhang et al. [220]	Unspecified	Unspecified	The bandpass filter of 750–950 nm	Beijing E-plus 3D Company

Table 9
Mapping of the literature on in-situ pyrometer installed in LPBF to monitor the process signature.

Prediction target	Publications	Prediction target	Publications
Temperature measurement	[11,50,87,90,134,225,226,228,232,235]	Distortion	[236]
Overheating	[156]	Density measurement	[227]
Overhang	[237]	Porosity	[233,234]
Anomaly detection	[109]	Melt pool temperature	[238]

Table 10
The characteristics of pyrometers used in the LPBF studies.

References	Type	Wavelength (nm)	Sampling time (kHz)	Temperature range	LPBF machine
Gaikwad et al. [11]	Infrared	1600–1800	100	Not calibrated; hence not converted to a temperature scale	Aconity3D
Forien et al. [87]	Kleiber KGA 740LO	1600 ± 100	100	Not calibrated; hence not converted to a temperature scale	Aconity3D
Haines et al. [225]	Kleiber KG740-LO	1580–1800	10	Not calibrated; hence not converted to a temperature scale	Aconity 3D Mini
Gutknecht et al. [235]	Two-colour	1450–1800	12.5 but digitalized at only 2	500–2500 °C	In-house
Islam et al. [50]	Thyssen Laser-Technik TCS	Unspecified	Unspecified	400–1400 °C	EOS M270
Furumoto et al. [90,232]	Two-colour	Below 1600	0.01–100	400–2200 °C	In-house
Mitchell et al. [233]	Two-colour	750–900	6–7	1100–2800 °C	ProX DMP 200
Wakai et al. [129]	Two-colour ThermeraNIR	$\lambda1 = 800$ $\lambda2 = 975$	0.05	1300–2400 °C	In-house
Smoqi et al. [234]	Two-colour Stratonics	$\lambda1 = 720$ $\lambda2 = 900$	0.8	Not calibrated; hence not converted to a temperature scale	EOS M280
Kozjek et al. [238]	Two-colour PrintRite3D	Unspecified	100	Unspecified	LASERTEC 12 (DMG MORI)

calibrations (effective wavelength and machine vision) steps are required to achieve high-precision measurements. The fringe projection technique has been used in LPBF to measure the height map of the powder bed/printed slice by B. Zhang et al. [239–241], Land et al. [242], Kalms et al. [243], Dickins et al. [244,245], and H. Zhang et al. [246]. B. Zhang et al. [239] placed the Qumi Q5 projector 560 mm above the powder bed. Also, one DSLR camera with a 50° angle with the projector and a combination of 18–55(mm) lenses were installed. The whole system was placed on top of the machine chamber based on their experimental design. Then, B. Zhang et al. [240,241], and Land et al. [242] upgraded the hardware by using the Point Grey Flea3 camera with a resolution of 4096 × 2160 pixels and a 50 mm Edmond Optics Part lens to achieve better height resolution. In this configuration used, the camera was mounted above (in the chamber) powder bed and the projector was installed on top of the machine chamber at a 30° angle. Land et al. [242] used the former hardware design with a projector and cameras mounted on top of the build chamber but verified that the spatial frequency of the irradiate fringe patterns is the most significant factor in determining the resolution of the height map [242]. Additionally, H. Zhang et al. [246] placed LightCrafter 4710 EVM G2 DLP projector with a resolution of 1920 × 1080 pixels and an FL3-U3-120S3C-C 12 MP CMOS camera on top of the EOS M290 machine (outside of the chamber), while Kalms et al. [243] and Dickins et al. [244,245] used more than one camera which was all mounted in the chamber along with the projector placed on top of the machines to reveal more information about the process. Kalms et al. [243] installed two 6-megapixel CCD cameras. Dickins et al. first used two 18 MP DSLR cameras [244] and then upgraded the system using four Basler ace acA572–17 μm cameras [245].

- Recoater blade-mounted sensor

Only limited studies were explored using the recoater blade sensor to gather 2D high spatial resolution in LPBF. Barrett et al. [247] placed a Keyence LJ-V7060 profilometer above the recoater to show surface mapping before and after the melting, disclosing the potential of scan sensors to identify the lack of fusion defects. Pedersen et al. [248] used a contact image sensor (CIS) unit on the recoater with an optical resolution of 2400 (dpi) over a length of 297 mm. Pedersen et al. [248] then applied image correction and geometry reconstruction techniques to calibrate the captured images. In the following work of Pedersen et al. [248], Tan Phuc et al. [249] used similar hardware to synchronize the recoater speed with the image acquisition system. Tan Phuc et al. [249] estimated the height map and discussed that the CIS approach could detect irregularities along the vertical direction. Additionally, Fischer et al. [250] installed a recoater blade line camera to acquire high-resolution images of the build area with a width of 97.76 mm at a resolution of 5.97 μm/pixel and a recoater speed of 100 m/s. The system was able to detect discernable line widths as small as 12.4 μm.

2.1.2. Non-radiative sensors

This type of sensor sense and measure the physical properties of the process. Non-radiative sensors installed in LPBF are categorized into acoustic sensors, thermocouples, and displacement sensors, according to Fig. 1.

- Acoustic sensors

Since balling effect, porosity formation, and residual stress could influence the sound dynamics, acoustic sensors have been used for monitoring the LPBF process. Different types of acoustic sensors have been placed in the LPBF system [251], such as:

A. Microphones and transducers,
B. Laser ultrasound,
C. Fiber Bragg gratings (FBG),
D. Spatially resolved acoustic spectroscopy (SRAS), and
E. Surface acoustic waves sensors

Acoustic sensors could also be categorized based on their frequency

range into 1) below 20 Hz (infrasound), 2) 20 Hz- 20 kHz (human hearing ranges), and 3) above 20 kHz (ultrasound).

In the following sections, the detail of each acoustic sensor and its application in LPBF will be explained.

A. Microphone and transducer

A microphone could be indicated as an acoustic to the electric transducer enabling the conversion of the air pressure variations of the sound wave to an electrical signal. Different types of microphones are available such as piezoelectric, ribbon, condenser, and dynamic. The essential component of each microphone/transducer is a diaphragm. The schematic of the basic microphone is demonstrated in Fig. 5(a). As shown in Fig. 5(a), when the sound wave hits the diaphragm, it will vibrate. The vibration is transferred to the magnet via a coil/piezo-electric, leading to producing an electrical current.

Additionally, when a pressurized fluid escapes through a leak, it generates acoustic noise. This type of acoustic noise could be transmitted by air or solid objects. When noise is transmitted by air, it is called airborne noise, whereas when it is transmitted by a solid object, it is known as structure-borne noise. The air-borne noise is mostly recorded by a microphone with a sampling frequency range of up to 50 kHz, while the structure-borne noise is measured by piezoceramic transducers. The basic piezoceramic transducer is shown in Fig. 5(b).

State-of-the-art studies employing microphone/transducer sensors in LPBF are reviewed in the following studies. Ye et al. [2] placed a PCB microphone with a sampling frequency range of 500–90,000 Hz. The collected signal was then transferred to the frequency domain for further analysis. However, Kouprianoff et al. [252] applied short-time Fourier transformation (STFT) to analyze the AE signal. Filters were also used to eliminate the noises during recording. After filtering and transformation of the signal, the difference in amplitude of frequencies was reported to be an indicator of a lack of fusion in the LPBF process. In another research, Pandiyan et al. [253–255] used a low-pass Butter-worth filter of 100 kHz to record the frequency range of up to 100 kHz for failure mode (no pore, balling, keyhole, and lack of fusion) detection in LPBF. Rieder et al. [256,257] and Park et al. [258] investigated the application of an ultrasound transducer in LPBF for the detection of phenomena such as surface dynamics, residual stress, balling, and porosity level, respectively. Structure-borne acoustic emissions (SBAE) were measured in the study of Eschner et al. [259,260] by Q-WT-190232 piezoceramic sensor and Pandiyan et al. [223] by PICO HF-1.2 with a sensitivity range of 500–1850 kHz. The objective in the former study was to classify the porosity, and in the latter is to classify the conduction and failure modes. The type, sampling frequency, and additional filters of microphones used in the LPBF studies are summarized in Table 11.

B. Laser ultrasound

A laser ultrasound (LU) sensor consists of a pulse generation laser, a continuous-wave detection, an interferometer, and processing electronic hardware. Firstly, the pulse generation laser sends the ultrasonic wave to the surface by which the surface wave is created. The surface displacement is measured with the laser detector. Then, the scattered or reflected light is collected by the interferometer and transferred to the electronic hardware, as shown in Fig. 5(c). Laser ultrasound sensors were utilized in the study of Everton et al. [261–264] and Xu et al. [265]. Everton et al. used a class IV Q-switched Nd: YAG laser with a 200 mJ energy pulse and repetition rate of 20 Hz to generate an ultrasonic wave at the wavelength of 1064 nm. The receiver laser wavelength was narrowed down to 1550 ± 10 nm with filtering. Recently, Xu et al. [265] used a pulsed laser with a maximum pulse energy of 2.12 mJ to generate an ultrasonic pulse with a wavelength of 1064 nm. The wave with a duration of 1.5 ns and a frequency operation of 2 kHz was generated.

C. Fiber Bragg gratings (FBG)

The fiber Bragg gratings (FBG) sensor is another type of acoustic sensor used in LPBF to monitor acoustic emission. A normal fiber string has a uniform reflective index along the length; however, the reflectivity of FBG changes periodically in a specific zone of the fiber string. When the wave hits the FBG, the wavelength with a similar wavelength as gratings is back-reflected to the input. Other waves pass through the length of FBG (Fig. 5(d)). The behaviour of the reflected and transmitted waves could disclose useful information in terms of wavelength shifts that can be translated to the temperature and stress deviation in the location of the fiber string that gratings are created. This type of sensor was placed in LPBF systems by Shevchik et al. [266] and Wasmer et al.

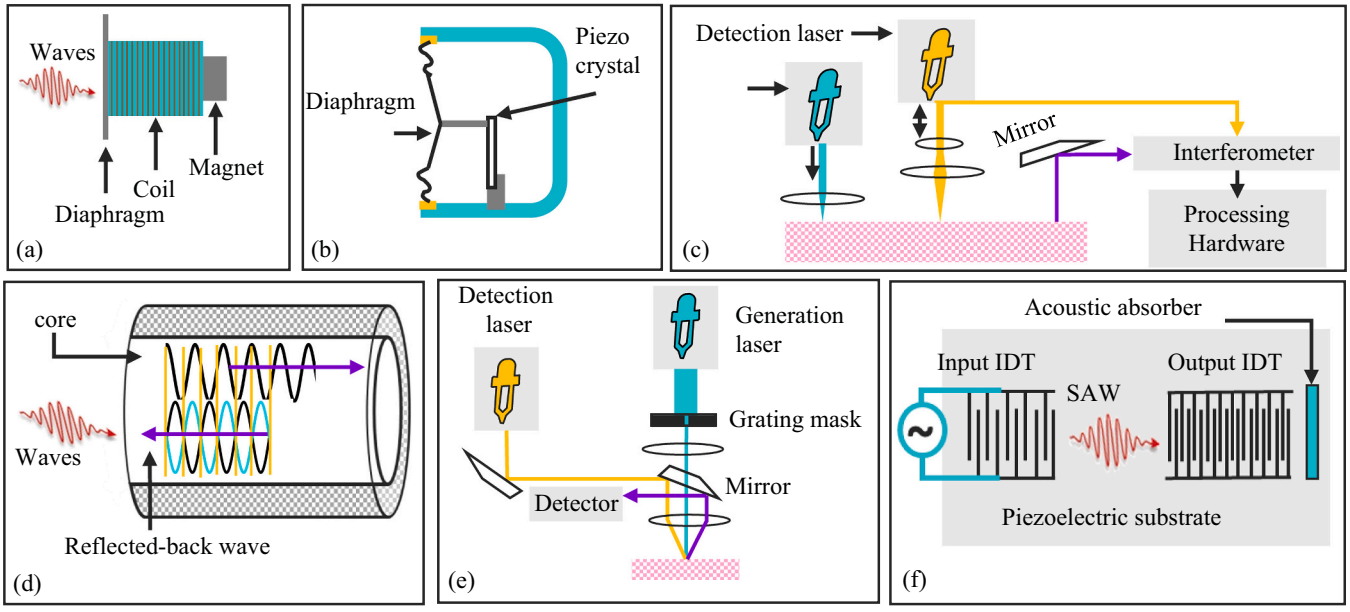

Fig. 5. The 2D schematic of the a) basic dynamic microphone.
(Source: Redrawn and adapted from [1]), b) piezoceramic transducer, c) laser ultrasound, d) FBG, e) SRAS, and f) surface acoustic waves sensors (Source: Redrawn and adapted from [276])

Table 11
The type, sampling frequency, and additional filters of microphones used in the LPBF studies.

References	Type of sensor	Sampling frequency (kHz)	Filter	LPBF machine
Ye et al. [2]	3780C1 PCB microphone	0.5–90	Butterworth frequency bandpass	In-house
Plotnikov et al. [136]	Three R-15a	100	8th order Butterworth high-pass filter	EOS M290
Kouprianoff et al. [252]	ICP	102.5	Low cut-off frequency 1500 Hz	EOS M280
Pandiyan et al. [253–255]	PAC AM4I	Up to 100	Low-pass Butterworth	In-house
Rieder et al. [256,257]	Ultrasound transducer	10,000	–	EOS M 270
Eschner et al. [259,260]	Q-WT-190232 piezoceramic	4000	–	In-house
Pandiyan et al. [223]	PICO HF-1.2	0.5–1850		In-house

Table 12
The detailed information on SRAS sensors used in the LPBF studies.

References	Laser type	Q switched laser wavelength (nm)	Energy pulse (μJ)	Repetition rate (kHz)	Detector laser wavelength (nm)	Additional equipment	LPBF machine
Smith et al. [269]	AOT-YAG-10Q	1064	50–150	1–12.5	532	20 mm objective Band-pass filter	ReaLizer SLM50
Smith et al. [270]	AOT-YAG-10Q	1064	50–150	1–6.25	532	–	Renishaw AM 250
Hirsch et al. [272]	AOT-YAG-10Q	1064	50–150	1–6.25	532	–	ReaLizer SLM50
Dryburgh et al. [271] Williams et al. [273]	AOT-YAG-10Q	1064	50–150	2	532	–	ReaLizer SLM50

[267,268]. Wasmer et al. [268] mounted the FBG and a 1547 + 0.01 (nm) narrow-band filter on the Concept M2 machine. The reflected signal was digitized with a sampling frequency rate of 1 MHz.

D. Spatially resolved acoustic spectroscopy (SRAS)

In the SRAS technique, the setup includes the pulse generation laser, continuous-wave detection laser, and grating mask. The generation pulse laser generates the acoustic waves which are passed through an optical amplitude grating and imaged onto the sample surface. This incident causes the creation and propagation of acoustic waves, such as Rayleigh waves, with a frequency of f_s. On the other hand, the detection laser is used to probe the frequency (f_s) of surface perturbation which will be reflected in a knife-edge detector, as depicted in Fig. 5(e). Regarding the LPBF studies using SRAS, works done by Smith et al. [269,270], Dryburgh et al. [271], Hirsch et al. [272], and Williams et al. [273] could be pointed out. In their setup, a compact Q-switched laser generated the wave at the wavelength of 1064 nm. The wave was passed through a grating mask, imaged to the sample surface, and back-reflected to the detector laser. More details about the properties of sensors applied in the abovementioned studies are listed in Table 12.

E. Surface acoustic waves sensors

The surface acoustic waves sensor consists of a piezoelectric substrate, input IDT, output IDT, voltage source, and acoustic signal detector. Input and output IDTs are placed on the opposite side of the substrate, as shown in Fig. 5(f). The voltage source generates a voltage that is passed to the input IDT. The input IDT converts the voltage to an acoustic Rayleigh wave. This wave is then transferred to the output IDT by the piezoelectric surface. Any fluctuation in the material characteristics results in a change in acoustic wave velocity or amplitude which will be transferred to the signal detection circuit through the output IDT [274]. Slotwinski et al. [275] used the surface acoustic waves sensor to detect porosity in LPBF. In Slotwinski's study [275], a piezoelectric element was used having a nominal diameter of 12.7 mm with a commercial 5 MHz contact transducer.

- Thermocouple

A thermocouple is an electrical device to measure temperature. The thermocouple consists of two dissimilar electrical wires known as cold and hot junctions, as shown in Fig. 6. The cold junction is connected to the known temperature body, which is the reference, while the hot junction is attached to the body of unknown temperature. In proportion to the temperature difference between the two junctions, electric and magnetic fields (EMFs) are being developed, which are correlated back by using a reference table to measure the temperature of the unknown body. Reference tables are unique for each type of thermocouple [251].

The thermocouple is sensitive to a wide range of temperatures (−200 °C to +2000 °C) and is robust to shock and vibration. On the other hand, it is vulnerable to corrosion and noise. Thermocouples are mostly used with a combination of other sensors in LPBF. Dunbar et al. [278] used a combination of thermocouple and displacement sensors, while Van Belle et al. [279] implemented both thermocouple and strain gauges sensing to record the temperature evolution and strain variation, respectively. Sensors were connected to a FRONTDAQ data acquisition device. The experimental results were then used to validate the numerical model. Mohr et al. [133] used a combination of an IR camera

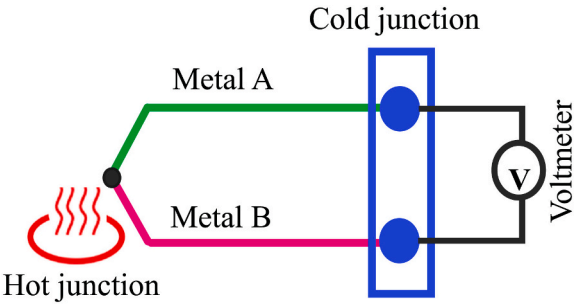

Fig. 6. The simple schematic of the thermocouple.
(Source: Redrawn and adapted from [277])

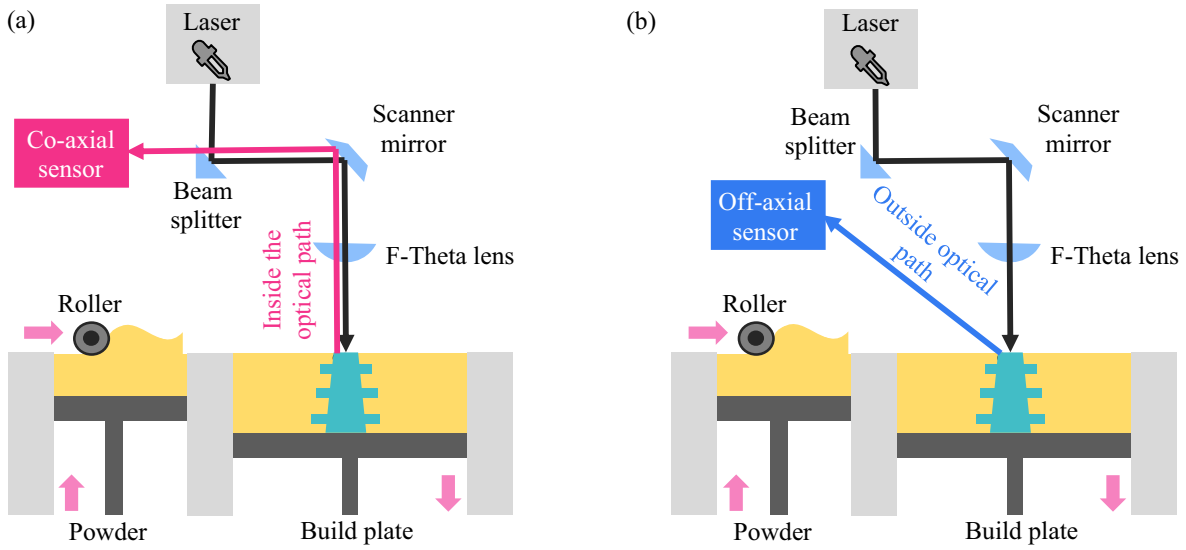

Fig. 7. The position of a) co-axial and b) off-axial sensors.

and four K-type thermocouples. The thermocouples' responses and IR images were then used to measure the emissivity of bulk and powder surfaces.

- Displacement and strain gauge

A displacement sensor is a device that calculates the distance between the sensor and objects [280] based on two different methods: 1) contact and 2) non-contact. The contact-based sensor has not been used in the AM process. Although non-contact sensors are more implemented in the LDED process [281,282], Dunbar et al. [278] mounted a displacement sensor and thermocouple on the EOS M280 system to detect distortion. The work compared the numerical results and experimental measurements. Williams et al. [283] also installed a laser displacement sensor parallel to the building substrate of the AM250 machine at a vertical distance of 95 mm from the top surface.

A strain gauge is a type of displacement sensor that converts force, pressure, tension, and weights into electrical resistance, which will then be measured. When external forces are applied to an object, stress and strain could be measured by a strain gauge to disclose information about deformation. Limited studies have investigated the effect of stress and deformation in LPBF using this sensor. Van Belle et al. [279] and Havermann et al. [284] placed a strain gauge to measure stress, and Hehr et al. [285] used it to identify deformation.

2.2. Mounting strategy

During the part fabrication, AM monitoring systems document the build process and capture information. Several main types of sensing equipment have been widely installed in LPBF systems to measure relevant parameters, as discussed in Section 2.1. It should be considered that the mounting strategy of sensors is highly influential in the monitoring process. Two types of mounting strategies are used to set up sensors: “co-axial” and “off-axial”. The co-axial sensor is positioned in the direction of the power source (laser), while the off-axial sensor is placed outside the optical path, as represented in Fig. 7. Additionally, data is transferred through different paths into these sensors. The data captured by the co-axial sensor is passed through the optical components (Fig. 7(a)); however, the off-axial sensor collects the data with a given angle of view (Fig. 7(b)).

Fig. 8 (a) demonstrates the volume of papers associated with co-axial and off-axial sensor setup in the melt pool monitoring assessments used in the LPBF process. 319 reports have been published since the first use of in-situ sensors to monitor the LPBF process in 2006. Among them, 102 and 217 papers were respectively reported using co-axial and off-axial sensor arrangements. According to Fig. 8 (b), the camera (visible to NIR and NIR to LWIR), pyrometer, and photodiode sensors have been installed both co-axially and off-axially. Based on the principle, optical inline coherence imaging was co-axially implemented, whereas X-ray imaging, fringe projection, scanner, acoustic, thermocouple, and displacement sensors were installed off-axially.

Table 13 categorizes different co-axial and off-axial sensor arrangements used in LPBF classified by sensor type to monitor various kinds of process signatures.

2.3. Commercially available sensors[1]

Various commercial modules are developed to capture in-situ data using different melt pool monitoring sensors. Most of these in-situ data require offline processing. Available sensors commercially mounted on the LPBF systems are designed by EOS, SLM solution, GE Additive, Renishaw, Trumpf, Sigma Additive Solutions, and Stratonics Inc (Table 14). Each of these modules will be explained below:

2.3.1. EOS

EOS has introduced two modules:

1- EOSTATE Melt pool Monitoring consists of co-axial and off-axial photodiodes. These photodiodes capture light intensity signals with the wavelength range and sampling frequency of 750–900 nm and 60 kHz, respectively. EOSTATE monitoring software is also designed to detect signal disturbance by three statistical algorithms (Absolute Limits, Signal Dynamics, Short Term Fluctuations) [289].

2- EOSTATE Exposure optical tomography includes an integrated sCMOS camera system with a resolution of 2560 × 2160 pixels to capture powder beds' images. The camera uniformly takes 10 images per second. Then, all 10 captured images are merged as one image. After that, the final image is correlated with intensity. EOSTATE exposure OT software is also introduced to identify any thermal deviation [289].

[1] This section is partially reproduced from the previous publication of authors [1] with permission from the publisher conveyed through Copyright Clearance Center, Inc.

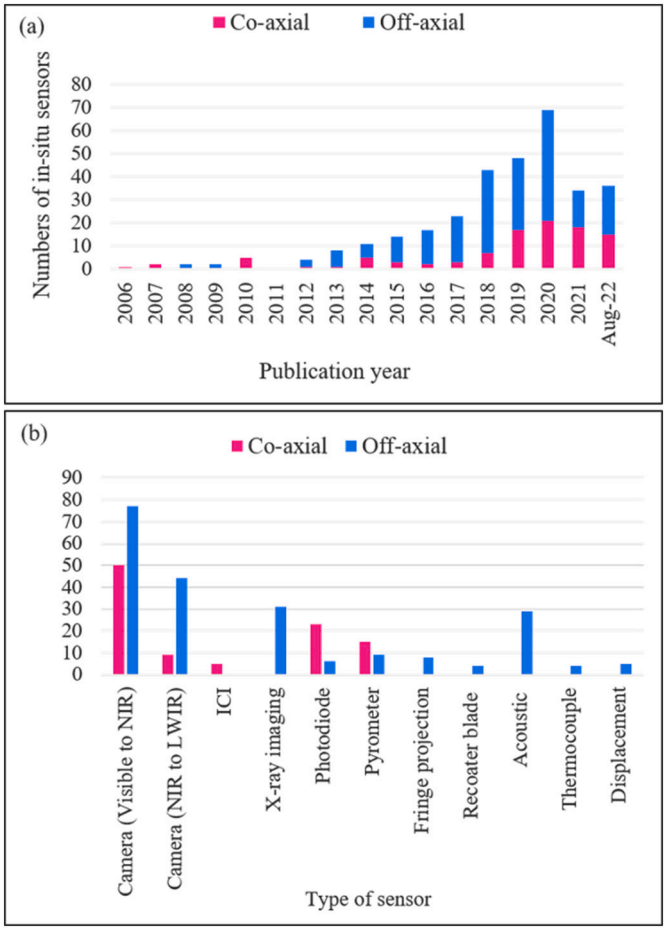

Fig. 8. (a, b) Relative emphasis of in-situ sensors arrangements based on their types reported in the LPBF literature.

2.3.2. SLM Solution

SLM Solution has introduced three modules:

1- Melt pool monitoring (MPM) consists of a co-axial pyrometer with a frequency rate of up to 100 kHz. The data is recorded and saved layer by layer and is immediately available for offline analysis after print [290].
2- Laser power monitoring (LPM) includes a co-axial camera to continuously record TARGET and ACTUAL laser output emitted from LPBF. Thereby, any existing deviations are recorded and displayed [291].
3- A layer control system (LCS) also includes an off-axial camera to continuously check the accuracy of each powder layer by detecting potential coating irregularities [292].

2.3.3. GE Additive (Concept Laser)

Concept Laser developed two modules:

1- QM melt pool 3D module consists of a co-axial photodiode and a high-speed CMOS camera to measure the average melt pool intensity and the melt pool area with a resolution of up to 35 μm. The sampling rate of the photodiode is 50 kHz, while the sampling rate of the camera is 15 kHz. Then, QM Melt pool 3D software could be used to map the emissions data to geometry [293].

2- QM coating includes a high-speed camera to capture images before and after layer deposition. Then, two steps are used to control the powder dose factor. In the first step, an intelligent algorithm measures the difference between images. After that, the analyzer investigates whether the powder is sufficient or not. This factor could be increased or reduced, or a new coating could be applied [293].

2.3.4. Renishaw

Renishaw has introduced the InfiniAM module, which includes MeltVIEW and LaserVIEW systems. The MeltVIEW system includes co-axial visible and infrared photodiodes to capture emissions from the melt pool, which can be used to detect build anomalies. The LaserVIEW system has a co-axial infrared photodiode to measure the input intensity of the laser. The LaserVIEW operates in two modes: 1) standard speed and 2) high speed. In the standard-speed mode, the system captures the energy in every laser pulse at a frequency rate of 100 kHz, which could then be analyzed to identify deviation or drift. In the high-speed mode, the data is collected with a frequency rate of 2 MHz which reveals the rising and falling edges of every laser pulse. Tracked temporal behaviour of each laser pulse is then analyzed by programming tools to identify the evolution of the melt pool dynamics [294].

2.3.5. Trumpf

Trumpf develops two monitoring modules:

1- Powder Bed Monitoring includes an off-axial camera for monitoring the melt pool, powder bed, and part geometry. Additionally, another phase is designed to analyze images by comparing them with the computer-aided design (CAD) model [295].
2- Melt Pool Monitoring monitors the melt pool during the fabrication and records the optical fingerprint of each process using special high-speed sensors. The system also has analysis software to present a graphical display of any deviation, such as a hot or cold melt pool [295].

2.3.6. Sigma Additive Solutions

The company has developed the PrintRite3D module including Sensorpak that comprises four sensors:

1) Photodiode which is off-axially placed with the field of view (FOV) of the entire build plate.
2) Photodiode, which is co-axially placed.
3) High-speed, single wavelength pyrometer which is off-axially installed with a 6 μs response time and field of view of approximately 1 mm.
4) The final sensor measures X and Y signals to finally visualize in-situ data in a 3D thermal point cloud. No clear information is available about it in the public domain.

All sensory data was collected by a DAQ module running at 50 kHz. Additionally, two software are developed for the analysis called “Inspect” and “Contour”. The Inspect software is designed to determine quality metrics and to identify suspicious patterns layer by layer [296]. The Contour software is developed for real-time monitoring and reconstruction of the part geometry to compare the result with the CAD model [297].

2.3.7. Stratonics Inc.

ThermaViz provides precise temperature measurement using a two-wavelength imaging pyrometer that collects data with a frame rate of 25 frames/s. The optical system resolution, the field of view, and temperature are respectively in the range of 10 μm/pixel to 1 mm/pixel, 5 mm to 500 mm, and 1000 °C to 2500 °C. Then, image processing software is provided to measure different melt pool behaviours such as melt pool thermal behaviour, peak and average temperature, solidification contour and dimensions, and heating and cooling rates [298].

Table 13
Mapping of the literature on in-situ sensors of LPBF to monitor the process signature.

Types	Equipment	Co-axial sensor arrangement	Off-axial sensor arrangement
Radiative	Camera Visible to NIR	Abnormal process [107–109] Geometry accuracy [8–11] Deformation [23] Balling [8] Delamination [58] Porosity [61,79,81,83–88] Overhang [92,96] Melt pool dimension [10,22,99–101,105,106] Overheating [52,53] Track width continuity [111,112] Residual heat effect [114] Melt pool temperature [18–22] Anomaly detection [286] Spatter [24,25] Cooling rate [22]	Porosity [54,55,62–78] Delamination [59] Overhang [59,82,92–95] Overheating [51,54–57] Recoater blade [59,60] Surface temperature [89,90] Balling [44,50,51] Spatter and plume [26–49] Surface roughness [97,98] Distortion [15] Dimension accuracy [12–17] Melt pool dimension [12–15,39,102–104] Anomaly detection [108,110] Cooling rate [113]
	Camera NIR to LWIR	Overheating [156] Melt pool dimension [143] Surface roughness [143] Dimension accuracy [138] Temperature measurement [133] Spatter and plume [154] Cooling rate [141]	Delamination [131,132] Dimension accuracy [139,140] Temperature measurement [134–137] Emissivity [133,151] Porosity [71,72,76,77,126,127,146–150] Inhomogeneity [148] Spatter and plume [126–128,155] Overhang [152] Surface roughness [127] Crack [128] Melt pool dimension [39,129,130,153] Deformation and distortion [144,145] Stress analysis [149] Cooling rate [130,137,142] Print parameters [157]
	Optical inline coherence imaging	Geometry accuracy [166] Melt pool dimension [173] Inhomogeneity [174] Distortion [174] Overhang structure [167]	–
	X-ray imaging	–	Geometry/dimension accuracy [177,187] Cooling rate [177] Porosity [87,129,177–186,190,195,197–202] Melt pool dimension [129,183] Spatter [179,183,186,190–196] Deformation [188,189] Stress analysis [203,204] Melting behaviour [205]
	Photodiode	Abnormal process [213,219] Geometry/Dimension accuracy [8,10,210] Overheating [52,53,58] Drift layer [82] Balling [58] Porosity [117,213–217] Part density [212] Hardness [220] Overhang layer [237] Overheating [156]	Emissivity [151] Geometry/Dimension accuracy [210,211] Porosity [216,218]
	Pyrometer	Temperature measurement [11,87,225,226,228,235] Anomaly detection [109] Distortion [236] Part density [227] Melt pool temperature [238]	Surface temperature [50,90,134,232] Porosity [233,234]
	Fringe projection	–	Height map of the powder bed/ printed slice [239–246]
	Powder bed scanner sensor	–	Height map [249] Porosity [247] Overheating and balling [2]
	Acoustic	–	Porosity [252,253,264–273,254,287,288,255,258–263] Process parameters [136] Part density [287] Residual stress [279]
Non-radiative	Thermocouple	–	Emissivity [133] Temperature measurement [71,133]
	Displacement	–	Distortion [278] Process parameters (layer thickness) [283] Strain measurement [279,284] Deformation [285]

Table 14
Commercial sensors mounted on LPBF machines.

Developer	Module Name	In-situ sensor	Mounting strategy	Monitored items	Publication	Type of detection
EOS	EOSTATE Melt pool	Two photodiodes	Co-axial Off-axial	Melt pool	Taherkhani et al. [214,217]	Porosity
					Schwerz et al. [216]	Porosity
					Harbig et al. [299]	Anomaly detection
					Ren et al. [300]	Anomaly detection
					Ren et al. [300]	Anomaly detection
	EOSTATE Exposure OT	Camera	Off-axial	Powder bed thermal map	Bamberg et al. [76]	Cold and hot spots
					Yadav et al. [301]	Drift layer
					Gobert et al. [302]	Print parameters
					Höfflin et al. [303]	Hatching distance
					Schwerz et al. [216]	Spatter
					Dursun et al. [304]	Overhang
					Pauzon et al. [305]	Contour scanning
					Zenzinger et al. [77]	Cold and hot spots
					Feng et al. [78]	Porosity
SLM Solution	Melt pool monitoring	Pyrometer	Co-axial	Melt pool	Artzt et al. [222]	Porosity
					Artzt et al. [306]	Contour scanning
					Alberts et al. [307]	Density measurement
	Laser power monitoring	Camera	Co-axial	Powder bed	–	–
	Layer control system	Camera	Off-axial	Powder bed	Ansari et al. [308]	Porosity
GE Additive (Concept Laser)	QM melt pool 3D	Camera Photodiode	Co-axial	Melt pool	Lapointe et al. [309]	Print parameters
					Klein et al. [310]	Porosity
					Toeppel et al. [311]	Density measurement
					O'Loughlin et al. [312]	Porosity
	QM coating	Camera	Off-axial	Build surface	Boos et al. [313]	Anomaly detection
					–	–
Renishaw	InfiniAM	Two photodiodes	Co-axial	Melt pool	Egan et al. [213]	Porosity
						Abnormal process
					Egan et al. [314]	Porosity
					Liu et al. [315]	Porosity
					Keaveney et al. [316]	Powder discontinuously
Trumpf	Powder Bed Monitoring	Camera	Off-axial	Powder bed and part geometry	Belloli et al. [317]	Deformation
					Colosimo et al. [318]	Geometry accuracy
	Melt Pool Monitoring	Camera	Off-axial	Weld pool and fusion process	–	–
Sigma Additive Solutions	PrintRite3D	Two photodiodes pyrometer	Co-axial Off-axial	Different monitoring possibilities	Kozjek et al. [238]	Melt pool temperatures
					Donegan et al. [319]	Porosity
					Megahed et al. [320]	Surface temperature distribution and melt pool dimensions
Stratonics Inc.	ThermaViz	Imaging pyrometer	Off-axial	Melt pool	Smoqi et al. [234]	Porosity
					Mahmoudi et al. [109]	Anomaly detection
					Karayagiz et al. [321]	Thermal measurements

3. Application of machine learning algorithms in defect detection

The adoption of LPBF to serial production is challenged by a lack of standards and proper quality assurance platforms. Like all conventional methods, serial production needs to be supported by reliable quality assurance setups. One solution could be developing a closed-loop control system to fully monitor and adjust the final product in a real-time manner. As a first step in developing the closed-loop control system, the in-situ dataset should be analyzed to provide real-time information about the process. In this regard, many researchers have analyzed the various types of in-situ data using statistical methods to detect process signatures and process windows that result in defects, such as porosity, material ejection, geometry distortion, and rapid temperature fluctuation [8–10,23,52,89,90]. In the following paragraphs, some of these studies will be reviewed.

To detect porosity, Abdelrahman et al. [83] cropped and normalized in-situ images and then applied a level set segmentation. Zenzinger et al. [77] and Bamberg et al. [76] developed the commercialized system for EOS known as exposure optical tomography (OT) by which cold and hot spots were identified from the statistical analysis of in-situ images and then corresponded to the nominal and abnormal areas.

Plasma plumes and spatters were identified in the research of Lane et al. [137] and Grasso et al. [155]. Lane et al. [137] converted the thermal video into temperature value and then showed how the calculated temperature gradient could be used to identify the spatter ejection. Grasso et al. [155] discussed using a bi-level thresholding method to extract plume and spatter information.

Finding the accurate geometry was also explored by Kruth et al. [10] and Craeghs et al. [53]. Kruth et al. [10] developed a PID controller to stabilize the melt pool dynamics by controlling the laser power. Craeghs et al. [53] developed a PI controller by correlating laser power and photodiode signal. The signal collected by the photodiode was converted to the Fourier domain and fitted to the second-order polynomial. Three PI controllers were designed and applied with bandwidths of 3600, 660, and 95 (rad/s) to control the laser power. Craeghs et al. [53] disclosed the effectiveness of the intermediate PI controller (660 rad/s) in enhancing the geometrical accuracy and surface roughness.

Temperature monitoring was implemented by Doubenskaia et al. [139], Lott et al. [322], Thombansen et al. [156], etc. Doubenskaia et al. [139] and Thombansen et al. [156] showed the effectiveness of the spatial map technique, while Lott et al. [322] applied a spot diagram and fast Fourier transformation (FFT).

Despite the valuable outcome achieved in of aforementioned studies, there are still many challenges, such as the size of in-situ data, storage of the in-situ data, and commercial real-time processing, which should be assessed to improve the quality. To address these challenges, the application of machine learning algorithms in LPBF has been discussed in recent years. The machine learning (ML) technique is a type of artificial intelligence (AI), that predicts data patterns by learning from the processes. Machine learning algorithms can be classified into three main groups:

1) Supervised learning,
2) Unsupervised learning, and
3) Reinforcement learning

Supervised learning and unsupervised learning algorithms are widely used in the LPBF process; however, reinforcement learning is applied only in limited studies to provide a quality assurance platform in the LPBF. Each of these methods includes several sub-categories, as represented in Fig. 9.

Fig. 10 represents the number of published studies using ML methods in LPBF. As demonstrated in Fig. 10(a), the use of supervised learning (79 %) is more popular than unsupervised learning (19 %) and reinforcement learning (2 %). Fig. 10(b) demonstrates the volume of papers associated with each sub-category. These algorithms will be comprehensively discussed in the following sections.

3.1. Supervised learning

The supervised learning algorithm is trained to map input data (X) to labeled output (Y). The training phase is repeated until the model can detect the pattern/relationship between input and output. The model is then tested by a new and unseen dataset, known as a test phase. Supervised learning is divided into classification (will be discussed in Section 3.1.1) and regression techniques (will be explained in Section 3.1.2). Each technique includes a different methodology and application to analyze the dataset.

3.1.1. Classification

Classification is a task to map the input variables (X) to discrete output variables (Y). Recent classification algorithms applied to the LPBF in-situ dataset are support vector machine (SVM), shallow and deep neural network (NN), adaptive neuro-fuzzy inference system (ANFIS), K-nearest neighbours (KNN), and random forest (RF). Table 15 lists some of these techniques applied in the LPBF process by highlighting their application to detect defects and flaws. The First column of Table 15 represents the above-mentioned algorithms and its second column is mapping the publication to the algorithm. Finally, the following columns list the detection target of each algorithm and publication.

In the following sections, the above-mentioned algorithms will be reviewed and their application in LPBF will be discussed.

- Support vector machine (SVM)

SVM is applied to classify the dataset by line/ hyperplane in 2D/ N-dimensional spaces. The optimum line/hyperplane is selected to provide the maximum distance between data points of different classes. The SVM easily classifies linear data ((a)) given by [329]:

$$f_{w,b}(x) = sgn\left(w^T x_i + b\right) = \begin{cases} w^T x_i + b \geq 1 \; x \geq 0 \\ w^T x_i + b \leq 1 \; x < 0 \end{cases} \quad (1)$$

where x_i, w, b are input, weight vector, and bias. However, more complex datasets (Fig. 11 (b), (c), and (d)) are classified by adding kernel functions to the model for transforming the dataset into the required form in a higher dimension. Different kernel functions are introduced, such as nonlinear, polynomial, radial basis, sigmoid, etc. For example, the data distribution presented in Fig. 11 (b), Fig. 11(c), and Fig. 11(d) need, respectively 2nd-order polynomial, 3rd-order polynomial, and radial basis kernel to accurately classify the data [329].

In LPBF, the SVM algorithm was used by Scime et al. [43], Gobert et al. [54], Ye et al. [2], and Petrich et al. [55]. Scime et al. [43], Gobert et al. [54], and Petrich et al. [55] applied SVM to identify defects in in-situ images. Scime et al. [43] analyzed the images from the melt pool of IN718 metal powder for fabrication by EOS M290. A SIFT feature extraction technique was calculated to extract the input images based on predetermined 36 process parameter combinations to create the desirable condition, balling effect, and keyhole porosity. The images were then converted into a standard vector format or histogram of oriented gradients (HoG) under three different contrast adjustments. The images were scaled using gamma values to create different contrasts. The final fingerprint consisted of nine segments related to different gradient fields which were created in different melt pool regions. After that, t-distributed Stochastic Neighbor Embedding was used to reduce data dimension, and multi-class SVM was applied to classify the input into five various melt pool types (desirable, balling, keyhole, etc.). A classification accuracy of 85.1 % was reported for 10-fold cross-validation to support the feasibility of the SVM algorithm by comparing the detection

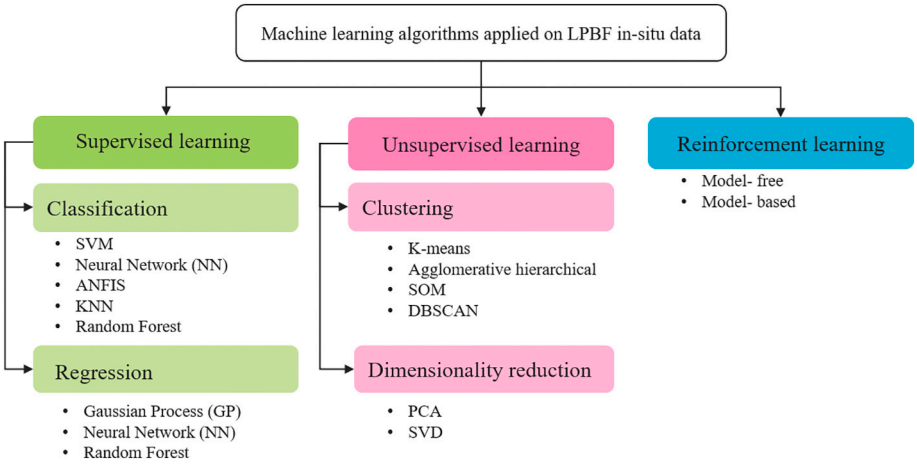

Fig. 9. Sub-categories of machine learning algorithm applied to in-situ data of LPBF.

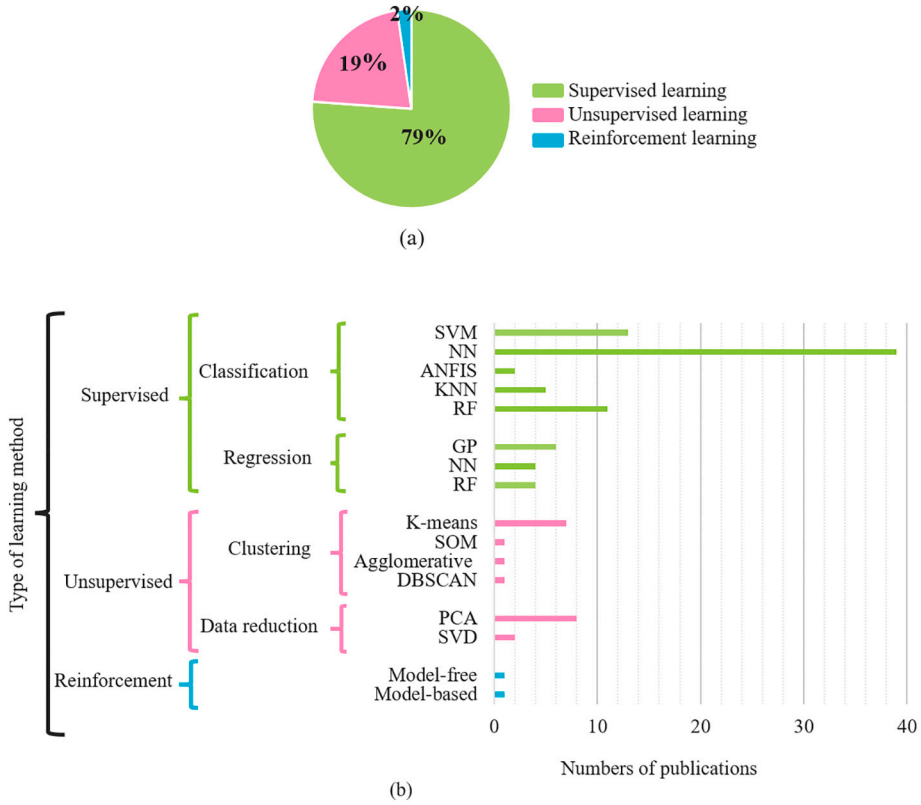

Fig. 10. (a, b) Relative emphasis of machine learning method in the literature using LPBF.

with ex-situ morphology information [43].

Besides, Ye's study showed the application of SVM to identify abnormal processes [2]. Although Ye's focus was to apply a deep belief network (DBN) on the acoustic signal in three stages 1- raw data, 2- the frequency domain calculated by power spectral density (PSD), and 3- after denoising (band-pass filter from 500 to 90,000 Hz) in the frequency domain, the multilayer perceptron (MLP) and linear kernel SVM were also applied for comparison. Each algorithm was trained to predict overheating, normal, and balling regions created by variations in scanning speed and laser power. The final result showed that although SVM works better for detection after post-processing, the algorithm has poor identification compared to DBN when applied to raw data. Thus, the DBN has more efficiency in detecting defects from the raw data without any feature extraction and data pre-processing [2]. However, in the case of the availability of more time for the user to apply FFT and denoising methods, SVM would be suggested. While in another similar study carried out by Li [61], DBN yielded better performance when compared with SVM and back propagation neural network (BPNN) with a classification accuracy of 99.59 % validated using the x-ray computed tomography (CT) method.

The SVM model was also applied to the in-situ data of two commercial photodiodes placed on the SLM 280 system by Yadav et al. [82]. The mean and median of both signals for each layer were calculated and fed to SVM with six kernels, including linear, cubic, quadratic, Medium Gaussian, Fine Gaussian, and Coarse Gaussian. These SVM models with different hyperparameters were optimized using the Bayesian method, and in the end, linear SVM was selected as the best model with an accuracy of 98.8 % for photodiode 1 and 99.2 % for photodiode 2. Then, the linear SVM was used to classify the drift (hotspot), which are layers with high temperatures, and non-drift layers. Although no more information was revealed due to the confidentiality of the research, it is reported that photodiode 2 was more sensitive compared to photodiode 1 to identify drift layers for ALSi7Mg0.6 [82].

- Neural network (NN)

An artificial neural network is a series of calculations to recognize relationships in the input(s)-output(s) pairs. Fig. 12(a) shows a basic neural network with one input layer, hidden layers, and one output layer. The computational device of the neural network is neurons/nodes which are connected by weights. Weights are used to transfer the input dataset (X) to the neuron (Fig. 12(b)). Then, neurons feed the weighted input dataset to an activation function (f). According to the application, different types of activation functions could be used, such as linear, Tanh, rectified linear unit (Relu), and sigmoid. In each iteration, the target is estimated, and an error between the estimated target and labeled output is calculated. The error is minimized in a backward pass by updating the weights.

Various neural network models are introduced and categorized based on their complexity, structure, and applications, such as feedforward (FF), multilayer perceptron (MLP), and deep learning (DL). MLP and DL algorithms were used to predict flaws in LPBF. The MLP network was applied to predict overheating [2] and porosity [2,265]. Deep-MLP model is also applied in the study of Kwon et al. [107] to classify melt pool images created by different laser powers. The result showed that by dropping the number of nodes and increasing the depth of the network (increasing the number of hidden layers in the neural network), even the images with blurred edges achieved satisfactory results. The model had a weak performance on the leave-one-out evaluation; however, the algorithm was able to find abnormal processes by simultaneous classification of various melt pool shapes.

Recently, the application of deep learning neural networks has achieved more attention in LPBF. Similar to the shallow neural network, the deep neural network is used to extract the relation between the input and labeled output dataset. One of the most popular types of DNN used in LPBF is convolutional neural networks (CNN). The schematic of the CNN model is represented in Fig. 12(c). Each CNN includes feature extraction and classification phases. The Feature extraction phase

Table 15
Classification models used to predict LPBF process signature.

Model		Reference	Detected output type																		
			Porosity	Spatter	Balling	Plume	Delamination	Geometry feature	Overheating	Overhang	Surface roughness	Geometry distortion	Track features	Recoater blade	Part density	Abnormal process	Fatigue life	Powder classification	Surface topology	Drift layers	Part failure
		[43]	*	*	*																
		[2]			*				*												
		[54]	*						*												
		[55]							*												
		[82]																		*	
		[109]	*																		
SVM		[84]	*																		
		[47]		*		*															
		[323]				*															
		[324]																*			
		[325]															*				
		[61]	*																		
		[11]						*													
		[2]				*			*												
		[84]	*																		
	MLP	[66]	*																		
		[259]	*																		
		[236]										*									
		[265]	*																		
		[70]	*																		
		[266]	*																		
		[65]	*																		
		[66]	*																		
		[326]	*																		
		[111]											*								
		[112]											*								
		[107]														*					
		[110]														*					
		[108]														*					
		[47]		*		*															
		[48]		*																	
	CNN	[26]		*																	
		[9]											*								
Neural		[327]																			*
Network		[97]									*										
		[98]									*										
		[82]							*	*				*							
		[60]												*							
		[140]						*													
		[14]						*													
		[236]										*									
		[254]	*		*																
		[227]													*						
		[100]						*													
	SNN	[266]	*																		
	DBN	[2]			*				*												
		[61]	*																		
	Depth wise-separable CNN	[131]		*			*														
	Conditional Auto Encoder	[326]	*																		
		[108]														*					
	TNN	[26]		*																	
	VAEs	[255]	*		*																
	RNN	[11]						*													

(*continued on next page*)

Table 15 (*continued*)

Model	Reference	Detected output type																		
		Porosity	Spatter	Balling	Plume	Delamination	Geometry feature	Overheating	Overhang	Surface roughness	Geometry distortion	Track features	Recoater blade	Part density	Abnormal process	Fatigue life	Powder classification	Surface topology	Drift layers	Part failure
DSCNN	[70]	*																		
	[223]	*																		
LSTM	[163]																	*		
	[328]															*				
ANFIS	[84]	*																		
	[109]	*																		
KNN	[11]						*													
	[234]	*																		
	[79]	*																		
	[287]									*				*						
	[197]	*																		
RF	[146]	*								*										
	[288]	*																		
	[109]														*					
	[80]	*																		

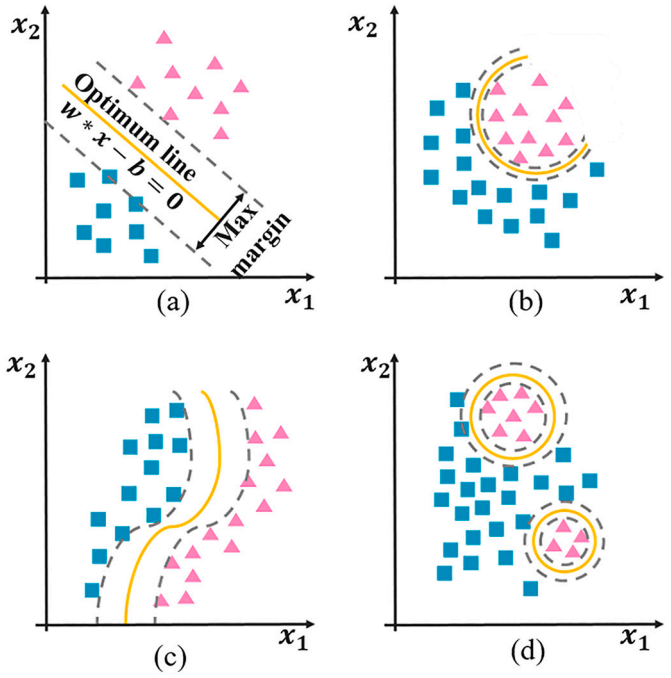

Fig. 11. The schematic of support vector machine (SVM) method: maximum margin for (a) linear, (b) 2nd-order polynomial, (c) 3rd-order polynomial, and (d) radial basis distribution of data.

consists of the convolution and pooling layers.

- In convolutional layers, filters are convolved with the original input to generate a feature map.
- In pooling layers, outputs of neurons at previous layers are combined into a single neuron to reduce data dimensions. Pooling could be applied in either way max-pooling (selecting the maximum value of the previous layer outputs) or average pooling (selecting the average value of the previous layer outputs).

In the second phase of CNN, known as classification, operations denoted as flatten, fully connected, and softmax are used. The flattening layer is applied to convert all the 2D feature map arrays into a single vector. The vector is then fed to the fully connected layer in which every neuron connects to every neuron in another layer. Finally, the softmax function is used as the activation function in the output layer of the model to predict a multinomial probability distribution. Besides weights and biases, other parameters and hyperparameters involved in CNN should be optimized to achieve a satisfactory result, such as filter size, stride, padding, learning rate, etc. An optimization algorithm is executed iteratively by comparing various solutions till a satisfactory solution is found. Many optimization algorithms were recommended with different features, for instance, mini-batch gradient, momentum, Gradient descent (GD), Root Mean Squared Propagation (RMSprop), and Adaptive Moment Estimation (ADAM) (refer to [330] for more information). After training the model, the accuracy of the training, validation, and test dataset must be verified to avoid underfitting (high bias) and overfitting (high variance) in the model. Underfitting happens when the model performs poorly on the training data. To remove underfitting, some strategies could be used, like an increase in model complexity and the duration of the training, an increase in the number of input features, and noise removal. On the flip side, overfitting happens when a model is closely aligned to the training data, but its performance against test data is poor. The possible suggestions to reduce overfitting could be regularization, data augmentation, dropout regularization, early stopping, input normalization, etc.

Although the numbers of convolutional layers, pooling layers, nodes,

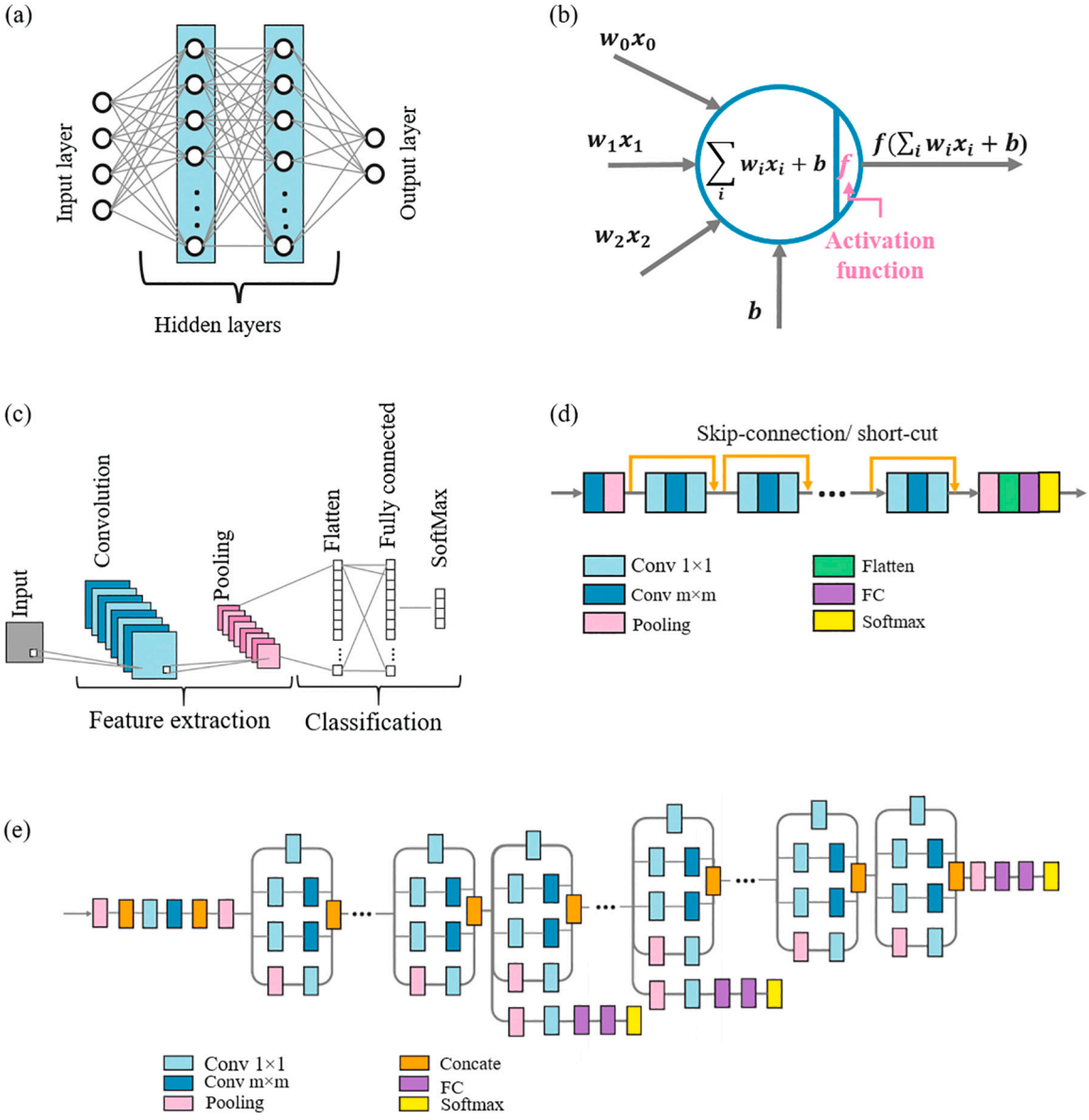

Fig. 12. The simple architecture of representative a) neural network, b) neural network node, c) CNN, d) ResNet, and e) Inception network.

and other parameters could be used arbitrarily, some CNN models were also introduced with fixed parameters such as AlexNet, VGG-16, ResNet, and Inception network. The architecture of AlexNet and VGG-16 is similar, but they differ in the number of convolution and pooling layers, neurons, size, and the number of filters, etc. For example, the former has 8 layers including 5 convolutional layers and 3 fully connected layers, while the latter has 16 layers, all of which are convolutional except for the last three fully connected layers. Also, AlexNet has a smaller number of filters in each layer compared to VGG-16. Thus, VGG-16 is more computationally expensive but has the capability to learn a more complex and diverse set of features [331]. The simple architecture of ResNet and Inception networks are shown respectively in Fig. 12(d) and Fig. 12(e). As demonstrated in Fig. 12(d), skip-connections are used in the design of ResNet to avoid vanishing gradient, which is one of the challenges of deep networks where the gradients computed during back-propagation become extremely small, making it difficult for the network to learn. Another challenge of deep networks is the computational time which could be solved by the Inception network since 1×1 convolution blocks are used to minimize computation load (Fig. 12(e)).

A more complex network such as bi-stream CNN and LSTM was also applied to the LPBF in-situ data inspection cases. As an illustration, bi-stream CNN consists of two series of kernel-based convolutional layers in which multiple feature maps could be extracted simultaneously (Fig. 13(a)). The comprehensive extracted feature help to accurately map input distribution to output classes. Long short-term memory (LSTM) is a type of sequence model. A sequence model can be used when the type of input or output are sequences of data such as audio data and video recognition. LSTM includes a unit with a memory cell (Fig. 13(b)) to keep information in memory for a long time which allows the network to learn longer-term dependencies.

In terms of the application of deep neural networks in LPBF, Zhang et al. [47], Caggiano et al. [65], Shevchik et al. [266], and Ansari et al. [308] used CNN to predict porosity. In the study of Zhang et al. [47], Caggiano et al. [65], and Shevchik et al. [266] porosities were created by changing print parameters, while in the study of Ansari et al. [308] intentional voids were added to the design of the coupons.

In Zhang's study, high-speed images were captured during the fabrication of stainless steel 316 L single tracks under the variation of laser power to create a keyhole, melt pool temperature, plume, and spatter. Then, images were fed into two models (SVM with RBF kernel

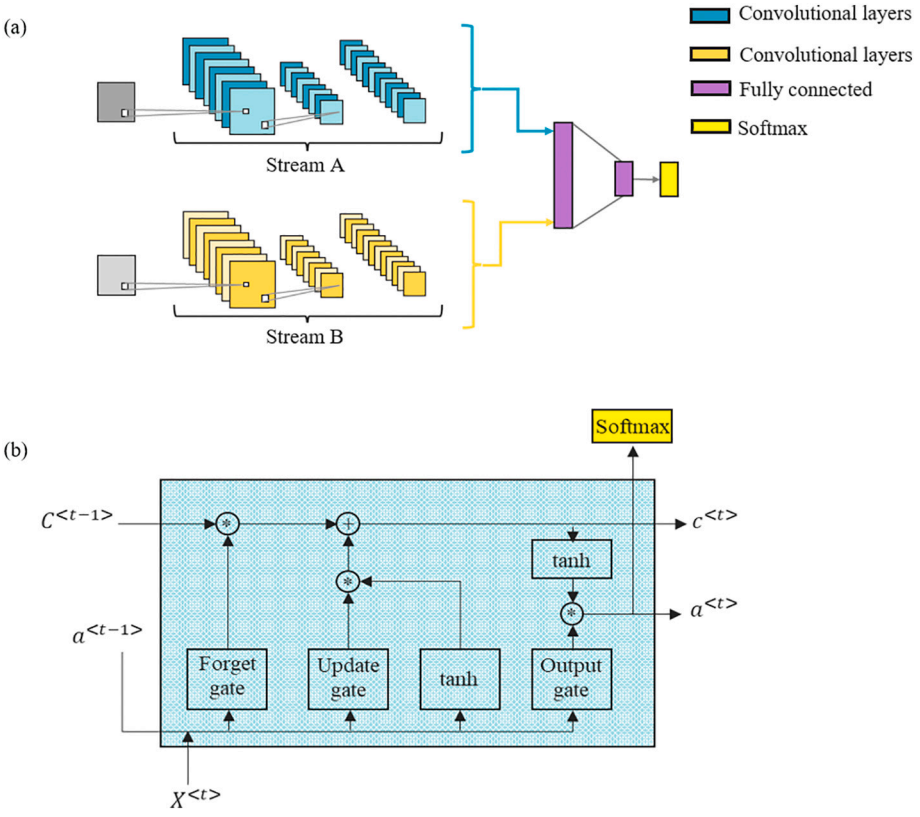

Fig. 13. The simple architecture of representative a) bi-stream CNN and b) one LSTM unit.

and CNN). The kernel size and pooling strategy of the CNN model were optimized using the AlexNet method. The comparison indicated that although SVM was trained with the extracted data, the CNN method classified features with higher accuracy. CNN also reduced the computational time of feature extraction and selection [47].

Caggiano et al. [65] applied a bi-stream DCNN model (Fig. 14) to the images extracted from the video which was recorded during the LPBF process. First, two images were extracted after material deposition and before laser scanning. Then, various feature maps from the collected images were extracted using kernel functions. After that, 840 images were selected to train the model, and 360 images were used to test the model, achieving an accuracy of 99.4 % to detect porosity, which was validated using an offline microscope image to verify the microstructural detail and confirm the defect types.

In the study of Ansari et al. [308] before applying the CNN model to the in-situ images, various preprocessing methods were applied to prepare the raw dataset for feeding into the network, including data labeling and augmentation. Ansari et al. [308] captured melt pool images from the fabrication of the coupon, including intentional voids, using the SLM Layer control system. Then, the captured images (2889 images) were labeled using both the CAD design and XCT scan of the fabricated parts. Since the porosity images were less than the non-porosity images, the data had a class imbalance which adversely affected the performance of the model. Thus, the porosity images were augmented by width shift range, height shift range, vertical flip, horizontal flip, and “nearest” fill mode to increase the minority class. After that, data was fed into the CNN model and all hyperparameters were optimized with an ADAM optimizer. The final result confirmed that using the balanced dataset improved the precision from 89 % to 97 % and recall from 85 % to 97 %. Ertay et al. [326] and Shevchik et al. [266] compared the result of CNN with other types of DNN, whereas Snow et al. [66] and Y. Zhang et al. [327] used a hybrid neural network. Ertay et al. [326] compared CNN and conditional variational autoencoder (CVAE) that were trained based on melt pool physics and CT-scan data. Thus, in Ertay's study in-situ sensor was not used. Fathizadan et al. [108] also used another type of autoencoder named convolutional autoencoder (CAE). The network was applied to extract the main feature of melt pool images, and then the extracted features were plugged into an agglomerative clustering algorithm which will be discussed in Section 3.2.1. Shevchik et al. [266] compared CNN with a statistical convolutional neural network (SCNN). First, a fiber Bragg grating (FBG) sensor was used to capture acoustic data. The sensor was off-axially installed on Concept M2 at a distance of 20 cm away from the melt pool. In addition, the cubical sample with CL20ES stainless steel powder was printed under three scanning speed conditions (50, 79, and 132 J/mm3) to provide three levels of energy input. Then, the Daubechies wavelet and principal component analysis (PCA) was applied to prepare data for training the CNN and SCNN models. The result of SCNN, with four convolutional and four pooling layers, was more accurate than CNN in classifying the features. The results mapped each energy input to the associated defects, with the highest energy input (132 J/mm^3) leading to keyhole defects of approximately 30μm, a reduced energy input (79 J/mm^3) causes the keyhole defects to disappear, leaving behind a small number of defects caused by lack of fusion and residual gas porosity. At the lowest energy input of 50 J/mm^3, the main type of defect is associated with inadequate bonding or insufficient fusion, manifesting as large, cavern-like voids that vary in size from 10 to 100 μm.

The performance of this study can be improved by installing a more sensitive acoustic sensor and applying more powerful filters. In Snow's study [66], neural network (NN) and CNN models were used to identify the lack of fusion defect created in virgin Ti-6Al-4V parts. First, a 36.3-megapixel DSLR camera (Nikon D800E) and various lightening conditions were placed on a 3DSystems ProX 320 to capture six images M1-M6 from 81 cylindrical coupons in each layer. These six images were included i) three images after the new powder was added to the build plate (referred to as “post-recoat”), and ii) three images after the laser scanned the layer (referred to as “post-scan”). The captured images from 20 coupon samples (individually and in the form of dimensional tiles)

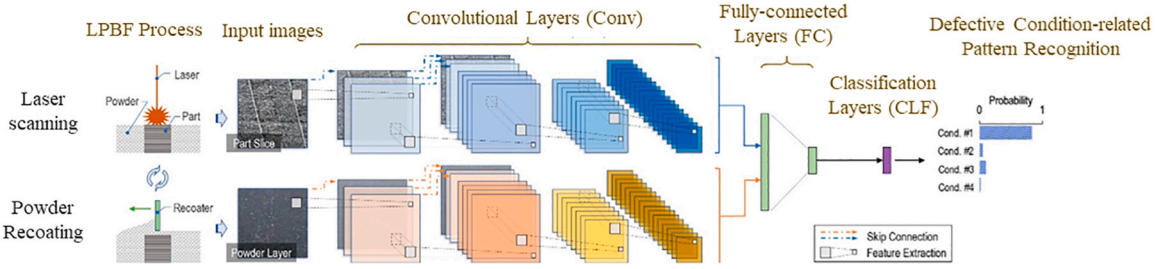

Fig. 14. Bi-stream DCNN to detect defects induced by improper SLM process conditions using before laser scanning (powder bed) and after laser scanning (fused layers) images.
(Source: Republished with permission of Elsevier, from [65])

were selected and labeled, by XCT using a custom automated defect recognition (ADR) algorithm [54,55] as nominal and anomaly and then fed into a series of NN and CNNs models. In the beginning, each model was trained separately, and results were compared through a confusion matrix demonstrating the accuracies of 69–78 % and 56–66 % for CNN and NN, respectively. Then, the hybrid method was suggested to improve the detection accuracy by feeding the outputs of CNNs and NNs to another shallow neural network with one hidden layer including five neurons. The new approach resulted in an accuracy of 93.5 %. Then, another build was fabricated to test the model, which showed an accuracy of 87.3 % [66].

Another hybrid NN model was used by Y. Zhang et al. [327] to predict part failure in terms of geometric incompleteness, cracking, and warping in the design phase. As demonstrated in Fig. 15, STL files were firstly voxelized using the binvox model with the size of 128 × 128 × 128 pixels. Then, the voxelized design was trained with model 1 (shown in Fig. 15) to decide whether the design was (label "1") or not printable (label "0") using a fully connected network. If the output of model 1 failed (output 1 = 0), then it was redirected to model 2 to predict the failure area (red colour in the final part). Model 2 was generally similar to model 1; however, it was designed based on the reshaping multi-dimensional layer by adding a transposed convolutional layer. The transposed convolutional layers were then concatenated with the initial convolutional layers. The proposed method was tested by fabricating 196 samples for training and 49 samples for testing. These samples were printed by three machines (EOS 270, AM 400, and AM 250) and with four different materials (Inconel 625, Maraging steel, ALSi10MG, and SS 316 L). The validation samples were selected randomly, and accuracy was used to validate the performance of model 1, and intersection over union (IoU) was selected to evaluate model 2. The results indicated that the proposed hybrid ML model could accurately predict the failure of the design.

Pandiyan et al. [223] and H. Zhang [163] also used a combination of CNN and LSTM models. Pandiyan et al. [223] applied them to predict the lack of fusion, keyhole, and conduction mode, while H. Zhang [163] used them to identify surface topology. In the study of Pandiyan et al. [223], first, input data, including three different wavelengths of intensity signal and acoustic signal (collected in different window lengths) were fed into the CNN model. The design of CNN consisted of five convolutional layers and a kernel size of 16, as shown in Fig. 16. Then extracted features were passed into the LSTM with one recurrent layer including ninety hidden states. Finally, the fully connected layer and a classifier were added to the network design to predict the lack of fusion, key-hole, and conduction mode. In total, 91 thousand parameters were trained by 900 epochs in 4.5 h with stochastic gradient descent and a momentum optimizer. Additionally, batch normalization, shuffling,

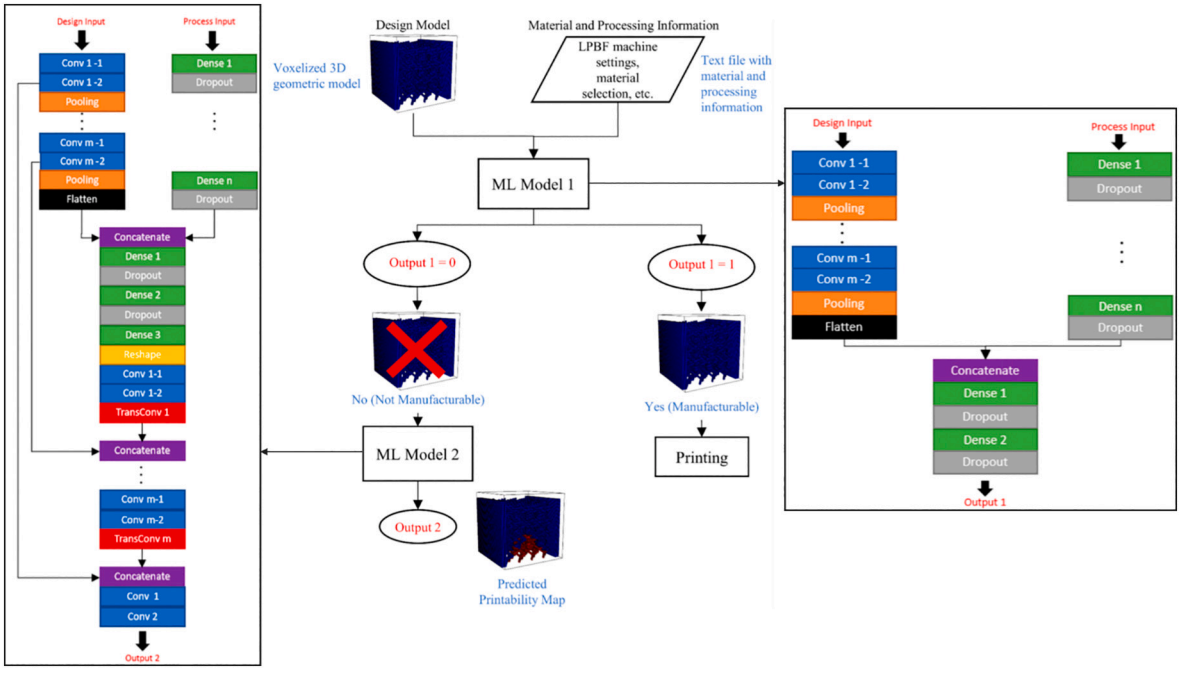

Fig. 15. Flowchart of the hybrid system developed in the study of Y. Zhang et al. [327] to identify part failure.
(Source: Republished with permission of Elsevier, from [327])

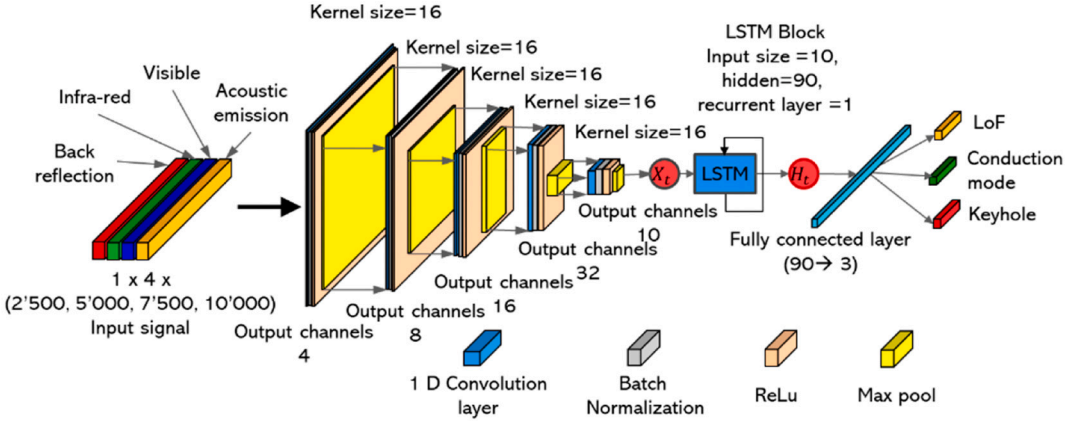

Fig. 16. The hybrid architecture of CNN-LSTM [223].
(Open access CC BY 4.0 license)

weight normalization, and dropout of 0.2 were considered to reduce overfitting and speed-up training time. The result of the confusion matrix indicated that the overall accuracy ranged from 95.9 % to 100 %, depending on the type of class.

In the work of H. Zhang et al. [163], two cameras captured images displaying the signatures of melt pools, including the intensity, area, and temperature, during the creation of IN718 fatigue bars. The process started with the installation of an off-axial high-speed camera, which was used to obtain laser scan data that was then analyzed using a ResNet 34 framework. This analysis extracted the spatial distribution of the melt pool signatures, including its area, intensity, and temperature. In the next phase, images from the coaxial single-camera two-wavelength imaging pyrometry (STWIP) system were examined to determine the melt pool profiles, which were then linked to the extracted melt pool signatures. The surface topography of the fatigue test samples was evaluated using an in-situ fringe projection profilometry (FPP) system. A long short-term memory (LSTM) neural network was then created to associate the recorded melt pool signature with the surface topology. The results were evaluated using the Random Forest Gini impurity method, yielding an accuracy of 92.88 % (relative prediction error) in the prediction of surface topology (the relative height difference between the fused layer and powder layer) while using only temperature signatures, compared to cases involving area and intensity signatures together with temperature or solely.

Gaikwad et al. [9] addressed thin-wall prediction using ML algorithms and in-situ monitoring data. Ti-6Al-4V thin-wall were created by changing build orientation (0°, 30°, 60°, and 90° to the direction of the recoater blade) and aspect ratio (ranging from 36 to 183). In-situ images were taken and then analyzed to extract features such as flaws in the part. On the other hand, after the process, XCT was used to extract the quantifier matrix, including the thin-wall thickness, density, edge smoothness, and discontinuity for each orientation. The quantifier matrices were aggregated to Mahalanobis-squared distance. Then, in-situ optical images (input) and Mahalanobis-squared distance (output) were fed into a CNN model to predict the thin-wall quality. To validate the result, the Pearson correlation coefficient (ρ) between the XCT scan signatures and CNN predictions was used, and the result showed a correlation of 85 % to 98 % [9]. Although this work has made significant progress in predicting the fault by reducing the steps required for part quality inspection, different part designs and variations in the print parameters were not considered.

Measuring surface roughness with the use of the CNN model was addressed in the study of Niklas et al. [98] and Knaak et al. [97]. Niklas et al. [98] trained the CNN model with the pair of hyperspectral images and the actual value of surface roughness measured by the Keyence VK X1050 confocal microscope. The convolutional network was comprised of four convolutional layers and a fully connected layer. ADAM and Nesterov-accelerated Adaptive Moment Estimation (NADAM) as optimizers and mean absolute error (MAE) as a loss function were used. Knaak et al. [97] applied CNN to extract features for the next step of their study, which will be discussed in Section 3.3. Spatter and delamination predictions were discussed by Baumgartl et al. [131]. In Baumgartl's study, a thermographic camera was off-axially installed on SLM 280HL with an angle of 60° to the substrate plate. Thermographic images were taken during the fabrication of H13 steel specimens. Then, the images were trained using a depthwise-separable neural network to predict defects. Spatter and delamination were manually chosen for the training of the network. The proposed network was validated by accuracy, sensitivity, precision, and Cohen's Kappa score. The average balanced accuracy of the model to predict spatters and delamination was 96.80 % from 10-fold validation. Besides, the network was evaluated with a heat map to detect the position of the defect. The advantage of the suggested model was its short computational time without using powerful hardware. Also, the model eliminated the use of X-ray or CT-scan [131].

Additionally, another hybrid neural network was used to predict distortion by Francis et al. [236]. Francis et al. [236] applied the CAMP-BD model, including CNN and ANN to predict distortion using thermal information and print parameters, respectively. Francis et al. printed a Ti-6Al-4V disk with a 5 mm thickness and a diameter of 45 mm. During the fabrication, thermal images were recorded using a co-axial, dual-wavelength pyrometer (Fig. 17. a). Then, thermal information and process parameters (Fig. 17. b) were fed into the CAMP-BD model to provide a final pointwise distortion prediction (Fig. 17. c) by using an Adam optimizer for updating the model weights and using a batch size of 512 along with ReLU activation function in all layers except the final output layer. The result demonstrated that the model could predict the distortion, and the model leads to convergence after 260 epochs with an RMSE of 24 μm [236].

Yadav et al. [82] recently identified five types of defects by applying two CNN models on pre and post-exposure images taken from each layer of the print during the fabrication of three different geometries (cubic overhang, cylindrical overhang, and specimen with inner groove). Then, both pre- and post-images were used to extract three different scale blocks (20 × 20, 75 × 75, 150 × 150 pixels) from the same center. Scale 1 (20 × 20 pixels) was set to identify part hopping[2] and overheating, whereas scale 2 (75 × 75 pixels) and scale 3 (150 × 150 pixels) were chosen to label recoater streaking and uneven powder spread, respectively. As demonstrated in Fig. 18(a), scale 1 was firstly trained in the CNN 1, and if the CNN 1 could label it as part hopping, the block was

[2] The area of the part which is above the powder spread and not fully covered by the powder spread.

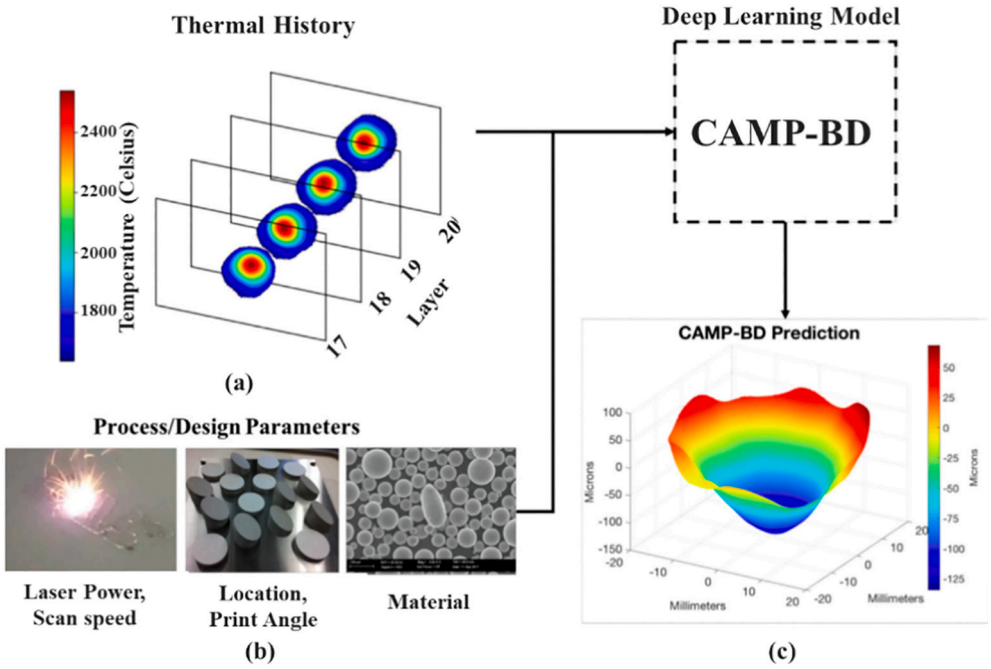

Fig. 17. Distortion prediction for the additively manufactured disc: a) thermal history per layers, b) design and process parameters, and c) CAMP-BD distortion predictions.
(Source: Republished with permission of Elsevier, from [236])

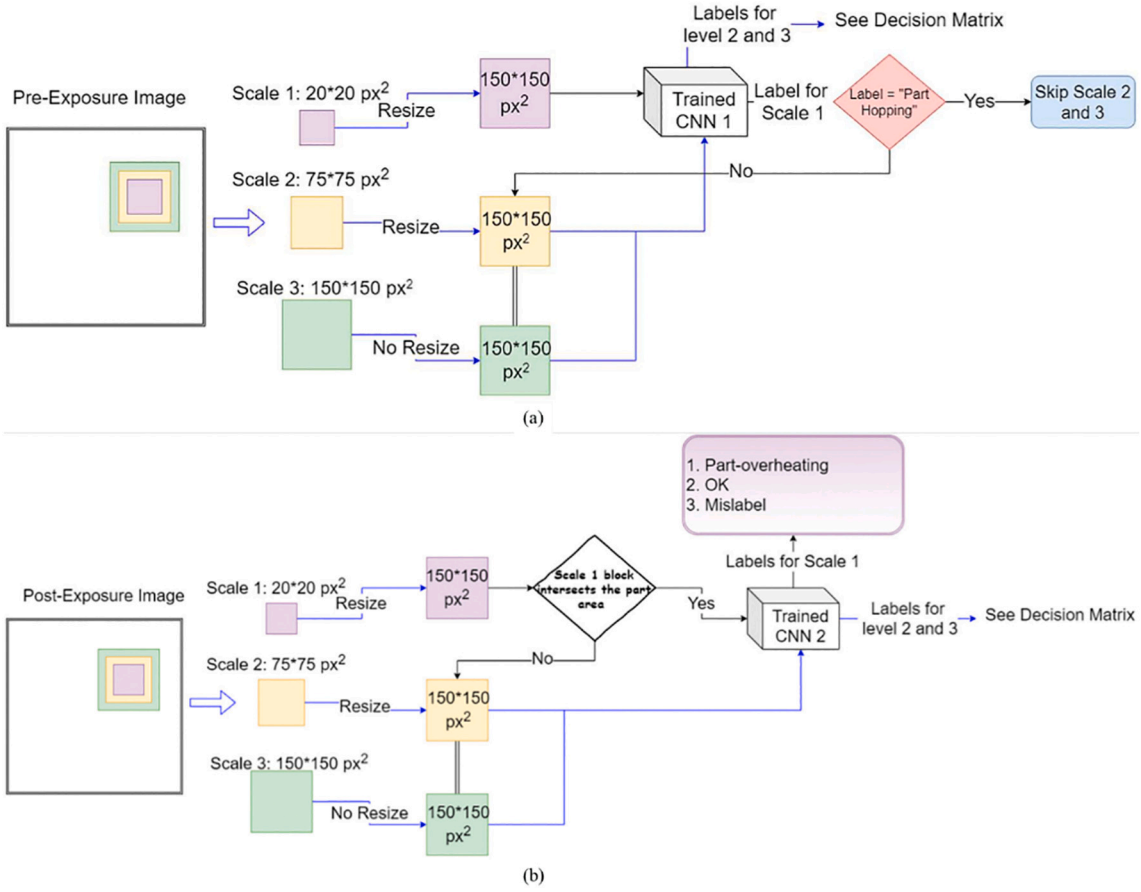

Fig. 18. Flow chart for labeling the a) pre-exposure and b) post-exposure images using CNN.
(Source: Republished with permission of John Wiley and Sons, from [82])

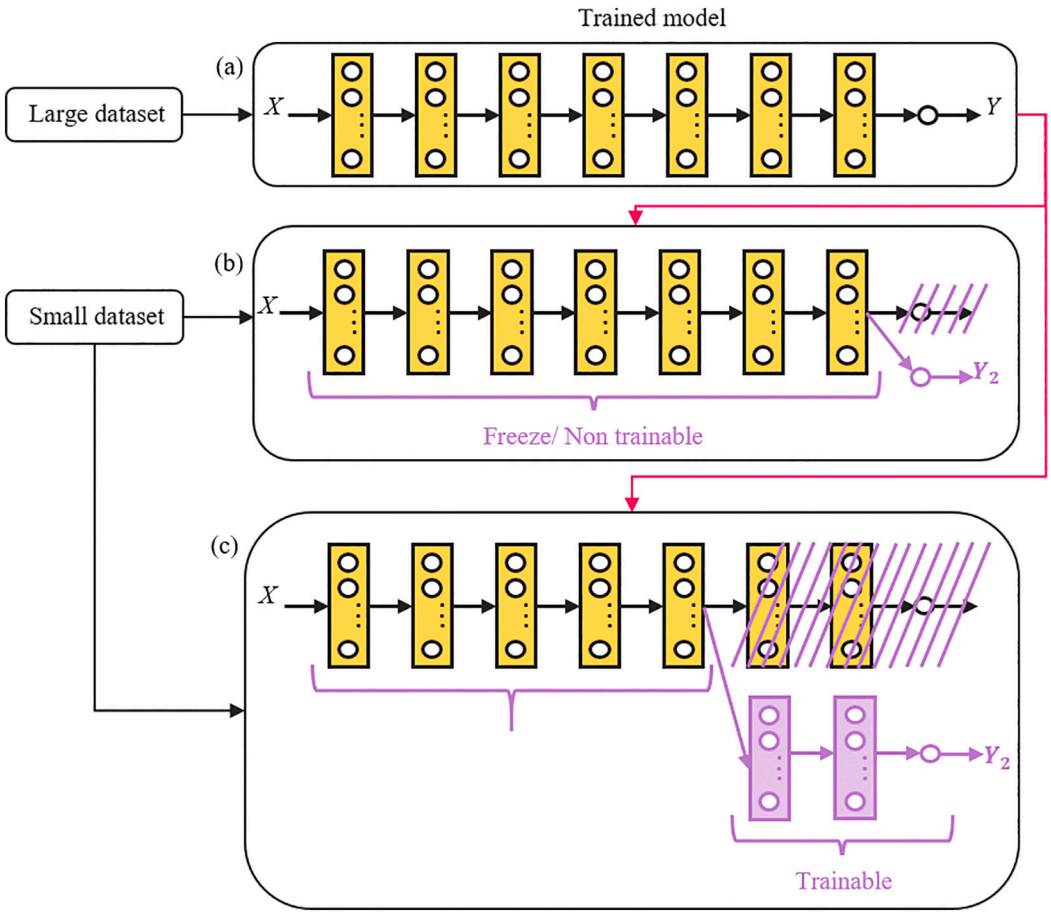

Fig. 19. a) Pre-trained model by large dataset, b) transfer learning to predict new task without any trainable parameters, and c) transfer learning to predict new task with trainable parameters.

labeled, and the program skipped the scale 2 and scale 3 analyses because when the part hopping occurs, other anomalies cannot happen at the same center. Additionally, a similar methodology was used to train the post-exposure images (CNN 2) in Fig. 18(b); however, it is impossible to identify any part hopping after the exposure step. As a result, the post-exposure images were first passed to a precondition to check whether there was an overlap between the scale block and part area or not. Thus, the following scenarios were considered:

1- The intersection was found: block scale could be labeled as overheating or "OK" part; however, if the predicted label is other than overheating or "OK", the block was labeled as misleading.
2- No intersection was found: scale 2 and scale 3 would be analyzed to identify other anomalies.

The same set of best-fitting hyperparameters resulted in the best training accuracy of CNN 1 and CNN 2 with 93.16 % and 96.20 % classification accuracy (confusion matrix), respectively, for labeling of pre- and post-exposure images to part hopping, streak, uneven powder, fine, and misleading. Then, the trained models were tested on the 2582 images captured during the printing of a benchmark part. Classification accuracies between 84 %- 97 % and 94 %- 99 % were obtained for different labels in CNN 1 and CNN 2 testing, respectively. Although the study reported that algorithms predicted anomalies successfully, it could be more comprehensive if the model could be tested for more complex geometry and compared with CT scan results [82].

More complex models were used in the study of Xing et al. [100] in which AlexNet, ResNet, SqueezeNet, InceptionV3, and vanilla-based architectures were applied to the dataset created by five laser energy spanning between 3 and 15 (J) to identify melt-pool width, length, inner area, and outer area. The research disclosed that ResNet and InceptionV3 yielded the highest F-score (96.6 %) on the test dataset, which indicated the superior performance of CNN to the manual and statistical approaches of classification such as ANOVA and Tukey's test (relied on melt pool measurements).

As mentioned previously, training deep learning from scratch and achieving high accuracy requires a large amount of data and expensive computational costs. Thus, transfer learning was introduced to help when there is a limited supply of similar training data. For applying transfer learning, weights, and other parameters are first obtained from a pre-trained model (Fig. 19. a). The pre-trained models are usually trained on the massive dataset and are mostly open-access. Then, obtained model and parameters can be reused without any tuning (Fig. 19. b) or with tuning (Fig. 19. c) to make predictions on new tasks or to be integrated into the process of training a new model.

Recently, the application of transfer learning was discussed by Pandiyan et al. [254], Klein et al. [310], and Liu et al. [315]. Pandiyan et al. [254] trained the CNN model from scratch to use it for transfer learning, whereas Klein et al. [310] used open-access networks. In Pandiyan's work, an air-borne acoustic emission sensor was used to collect acoustic signals from multiple 316 L stainless steel and bronze line tracks manufactured by variation in laser power and scan speed to create balling, lack of fusion, keyhole, and conduction mode (labels that were predicted by algorithms). In the next step, the acoustic signal was convoluted with a wavelet to calculate the continuous wavelet transform coefficients. Then, the coefficients were converted into a 2D spectrogram and linearly normalized. In total, 8000 images (Training: 5200 and Testing: 2800) were created from each material. Then, only 316 L stainless steel images

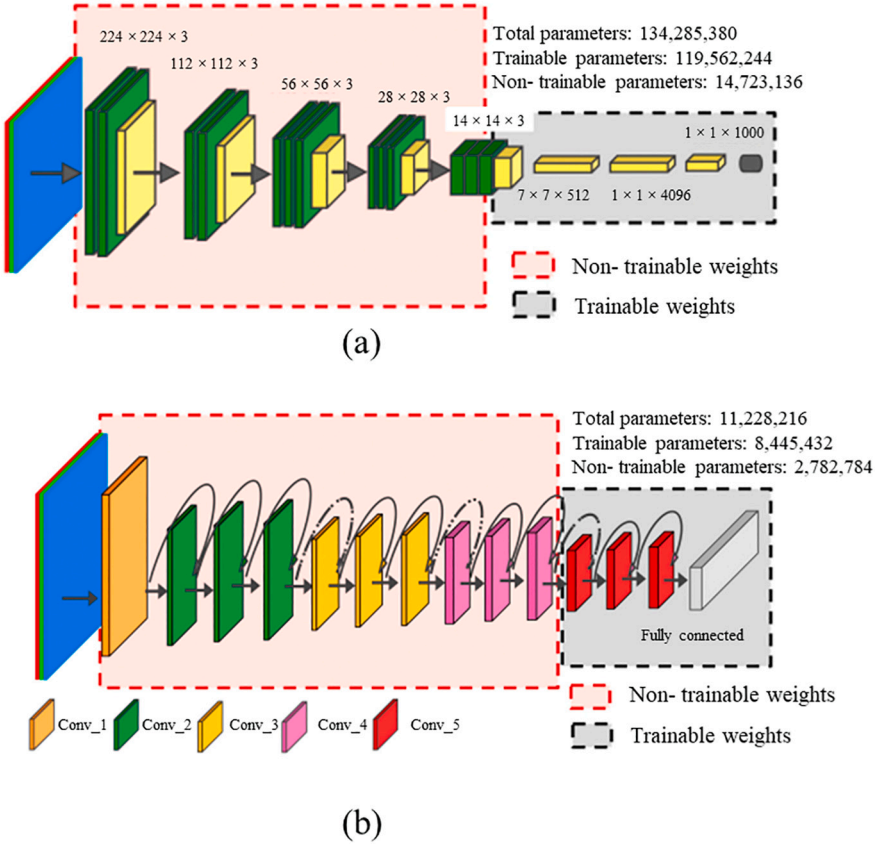

Fig. 20. The architecture of transfer learning in a) VGG-16 and b) ResNet-18 networks [254].
(Open access CC BY 4.0 license)

were fed into VGG-16 and ResNet-18 networks, which resulted in an accuracy of 96 % (trained in 18 h) and 94 % (trained in 12 h) in label classification, respectively. To apply transfer learning, VGG-16, and ResNet-18 models were partially trained with bronze images so that in the VGG-16 model, only the FC layers were trained (shown in Fig. 20 (a)), and in the ResNet-18 model, only the fifth bottleneck block layer and FC layer (Fig. 20(b)) were trained. According to ground truth data from the light microscope images of cross-sections, the final obtained accuracy of these two models in the transfer learning attempt was 85 % (trained in 9 h) and 87 % (trained in 6 h), respectively. Although the detection accuracy was reduced by 11 % and 7 % for each algorithm, the computational time was decreased to half [254]. Liu [315] explored the application of transfer learning by using VGG16 architecture pre-trained on ImageNet 2012 and DAGM 2007 datasets, comparing with SVM and fully connected classifier heads. Results showed acceptable classification accuracy on the images obtained from an in-situ monitoring system and industrial benchmarks named DAGM. In the study conducted by Klein et al. [310], three standard CNN models including VGG16, InceptionV3, and ResNet50 were used. These models were previously trained on ImageNet-dataset (see https://keras.io/api/applications/). Then, to adjust the new network, two fully connected layers and the SoftMax layer were again trained to classify porosity created by changing the print parameters. Given the actual porosity data provided by CT-scan, the final result showed the F1-score of 68 % for VGG16, 70 % for InceptionV3, and 70 % for ResNet50.

Table 16 lists some information about deep neural networks applied to the LPBF in-situ dataset and their defect target.

- Adaptive neuro-fuzzy inference system (ANFIS)

An adaptive neuro-fuzzy inference system (ANFIS) consists of an artificial neural network (ANN) and a fuzzy inference system (FIS) to estimate nonlinear functions in five layers (Fig. 21):

1) Fuzzification (layer 1 in Fig. 21) is used to compute fuzzy membership functions which could be triangular, trapezoidal, Gaussian, bell-shaped, sigmoid, etc.
2) Rule (layer 2 in Fig. 21) calculates the firing strength of a rule.
3) Normalization (layer 3 in Fig. 21) normalizes the firing strength.
4) Defuzzification (layer 4 in Fig. 21) is used to compute the weighted values of the previous node.
5) Summation (layer 5 in Fig. 21) calculates the final output by summing all outputs of layer 4 [332].

These layers are connected by weights. Weights and parameters of layer 1 and layer 4 are optimized during the training.

ANFIS has lots of applications in laser cladding to identify geometric dimensions [7]; however, only one study was conducted based on the ANFIS method in LPBF, carried out by M. Zhang et al. [328]. The model was trained to predict the fatigue life cycle of horizontal and vertical blocks printed by stainless steel 316 L using the EOS M290. Two sets of inputs were selected:

1- Process-based inputs including the layer thickness, scan speed, laser power, post-processing intensity, and maximum cyclic stress (for characterizing the loading condition, since fatigue tests were applied at a constant load ratio) with 5–1–3-3-5 Gaussian membership functions, and
2- Property-based inputs including the ultimate tensile strength, elongation to failure, and maximum cyclic stress with 4–4-4 Gaussian membership functions.

Table 16
The detailed information of the deep learning network applied to in-situ data of LPBF.

Author	Prediction	Type of network	Number of convolutional layers	Optimizer	Data size	Images pixel sizes
Caggiano et al. [65]	Porosity	Bi-stream DCNN	4	Stochastic gradient descent	Training: 840 Testing: 360	160 × 160
Zhang et al. [47]	Porosity and plume	CNN	5	Mini-Batch Gradient Descent	Training: 852 Testing: 284	227 × 227
Baumgartl et al. [131]	Delamination and spatter	Depthwise-separable convolutions	2	Not mentioned	1987	224 × 224
Yuan et al. [111]	Track parameters	CNN	3	Adam	Training: 700 Testing: 170	256 × 256
Gaikwad et al. [9]	Thin- wall	CNN	4	Stochastic gradient descent	Training: 16875 Testing: 5625	28 × 28
Shevchik et al. [266]	Porosity	SCNN	4	Gradient Descent	Not mentioned	Not mentioned
Xing et al. [100]	Melt-pool features	ResNet InceptionV3	18 48	Adam	Training:812 Testing: 88	300 × 300
Pandiyan et al. [254]	Balling Lack of Fusion keyhole	VGG-16 ResNet-18	16 18	Stochastic gradient descent	Training: 5200 Testing: 2800	512 × 512 pixels
Ansari et al. [308]	Intentional porosity	CNN	2	ADAM	Training: 2516 Validation: 1078 Testing: 1541	190 × 150

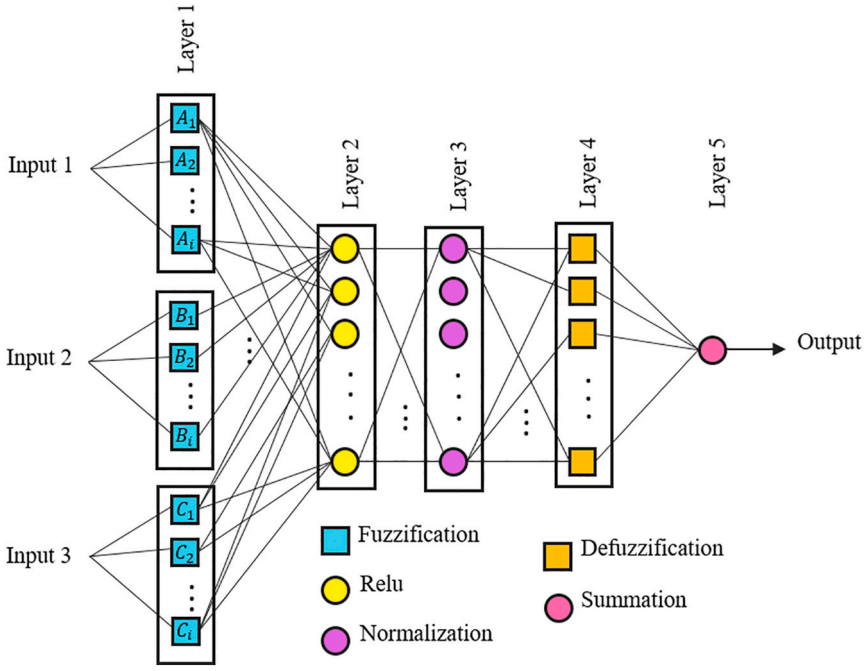

Fig. 21. The basic structure of ANFIS with three inputs and one output.

70 % of data points trained the model with nine and four rules for the process-based model and property-based model, respectively. The prediction result was evaluated by RMSE, which resulted in about 11 % to 16 %, as represented in Fig. 22, which shows the training and validation RMSE errors of the process-based and property-based models [328]. To improve the performance of the model, the construction of a large database should be considered; however, the obtained RMSE was less than the error level reported in another work which has the same percentage of input allocation [333].

- K-nearest neighbours (KNN)

KNN is a supervised learning method to find the relationship between input and output datasets by calculating the distance between a query and all other data points in four steps:

(i) Initializing K as the number of neighbours /classes (defined by the user),
(ii) Calculating the distance (d) between x and each training set
(iii) Choosing the closest K to x and labeling it as class A
(iv) Returning the mode of K labels [334]:

It should be noted that the KNN algorithm is also used as a regression model to label continuous datasets. In the regression case, instead of mode in step 4, the mean of labels should be applied. Implementation of KNN is easy; however, optimizing the number of classes could be

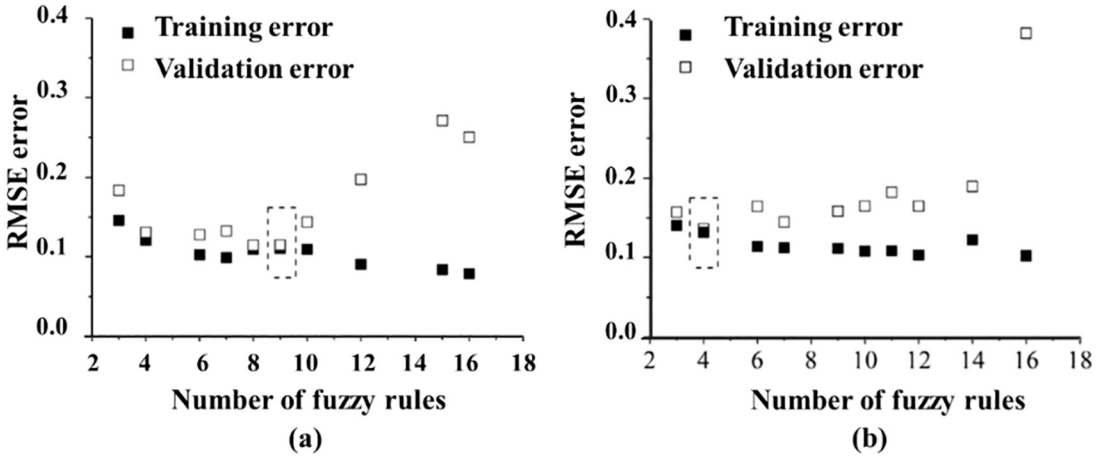

Fig. 22. Training and validation performance for the (a) process-based model and (b) property-based model using ANFIS model. (Source: Republished with permission of Elsevier, from [328]).

challenging. In addition, the algorithm is supersensitive to dataset quality and dimensions. The KNN algorithm was applied in limited studies of LPBF to compare its result with other ML methods. In Imani's study, the KNN prediction was compared with the result of SVM and feed-forward neural network (FF-NN), and the comparison resulted in poor performance of KNN [84]. Whereas, in Smoqi's study, KNN accuracy was compared with the detection of SVM, logistic regression, and CNN, which resulted in the highest prediction accuracy of porosity type and severity (ground truth values obtained through X-ray computed tomography and Archimedes (severity) and optical tomography and scanning electron microscopy (porosity type)) with KNN with the F1-score of 95 % [234].

- Random Forest

Random Forests (RF) is a supervised learning algorithm that consists of multiple decision trees. A decision tree (DT) can be used for both classification and regression tasks. The structure of the decision tree is hierarchical, consisting of the root node, branches, decision nodes, and leaf nodes (shown in Fig. 23(a)), with the following definition:

- The root node is the starting point of trees,
- Decision nodes divide the dataset into subsets, and
- Leaf nodes represent different outcomes [335].

Despite the simplicity and popularity of DT, this method can be susceptible to bias and overfitting issues. This challenge is tackled in RF since RFs select only a subset of the features instead of considering all the possible features like DT. Thus, the RF ensemble approach helps mitigate the effects of individual errors and leads to more accurate predictions. As demonstrated in Fig. 23(b), each tree produces a class prediction, and the class with the most votes becomes the final prediction. Similar to all supervised learning methods, before training an RF Model, it is necessary to set key hyperparameters: the node size, the number of trees, and the number of features sampled [335].

The application of RF to analyze the LPBF in-situ dataset was investigated in the study of Gaikwad et al. [79] Zhirnov et al. [287], Paulson et al. [197], Estalaki et al. [146], Drissi-Daoudi et al. [288],

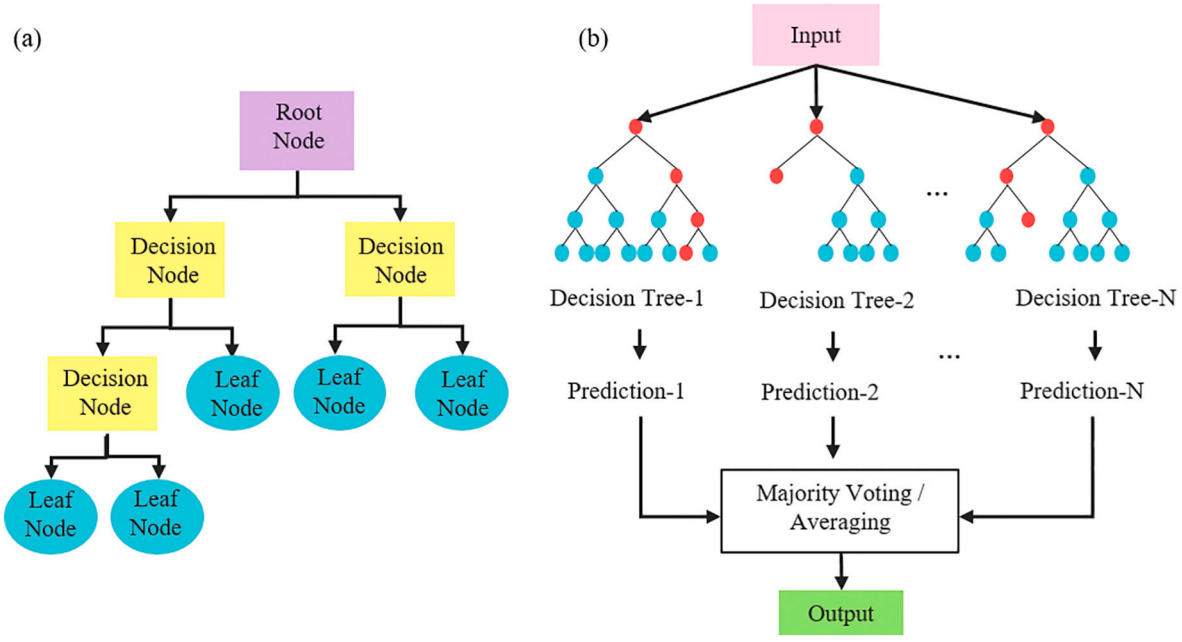

Fig. 23. The simple architecture of a) decision tree and b) random forest.

Mahmoudi et al. [109], and Williams et al. [80]. According to the mentioned studies, RF was mostly applied to predict porosity. For example, the prediction of porosity using high-speed infrared imaging was addressed in a study by Paulson et al. [197] in which the correlation between the thermal history of Ti-6Al-4V samples and subsurface porosity was investigated using RF. The input features consisted of blackbody radiances versus time signatures. The porosity classes are also identified and labeled using the X-ray images of the print and defined cut-off threshold. The model used 100 decision tree estimators with a minimum of 30 samples allowed before splitting. The primary result showed an accuracy of 86.6 % for the leave one group out cross-validation (LOGO-CV) and an accuracy of 100 % for the test set based on the RF model porosity classification (none, large, and small). In another study [288], RF was applied to data of a PAC AM4I airborne acoustic emission to detect the lack of fusion pores, conduction mode, and keyhole pores of three alloys (316 L stainless steel, bronze (CuSn8), and Inconel 718). The RF outputs were compared with the actual defect regimes obtained from X-ray tomography of parts' cross-sections. The model resulted in classification accuracy of >92 % by employing 100 decision trees and splitting based on entropy (for more information, refer to [336]). Estalaki et al. [146] also discussed the identification of defective and normal zone by applying RF. First, a FLIR SC6201 camera was used to capture thermal imaging information during the fabrication of stainless steel parts. After that, the two critical thermal features (the settling time above the apparent melting threshold (τ) and the maximum radiance (Tmax)) were calculated, saved for each voxel in the manufactured material, and fed into RF to classify each voxel as either defective or normal. The F-score of the RF was higher than 0.96 which was the best-yielded result among all other tested models such as KNN, DT, and multi-layer perceptron (MLP). In other studies, the performance of Random Forests was also compared with other supervised learning techniques. As an example, Gaikwad et al. [79] compared RF with CNN, while Williams et al. [80] compared it with KNN. In the study of Gaikwad et al. [79], first, melt pool signatures (such as melt pool temperature, shape, and size) and spatter were extracted from in-situ data of two co-axial high-speed video cameras. These extracted features were then fed into RF and CNN and the results of each method were evaluated using F-score and qualified according to X-ray computed tomography, Archimedes density, and destructive metallography measures. The highest F-score obtained from RF was 0.89 for deviation of laser spot size and 0.98 for porosity classification. However, applying CNN led to achieving better results with the F-scores of 0.97 and 0.95 for classifying the deviations of laser spot size and the porosity, respectively. In the study of Williams et al. [80], RF was found as one of the best methods along with KNN to achieve an area under the curve (AUC) of 0.91 for the detection porosity of stainless steel 316 L part fabricated by Renishaw AM250. Besides porosity, in limited studies, the application of RF was discussed in predicting the optimality of the process [287] and detecting anomalies [109]. Zhirnov et al. [287] collected acoustic signals and powder bed images to extract features for detection of lack of fusion using hard work tool steel powder. To detect the target, the RF algorithm was applied to 1484 labeled data points, including 36 different features with a low correlation between them. The model was employed to predict the optimality of the process based on the level of gas flow velocity adopted during the print of layers (highest velocity corresponding layers labeled as optimal and the rest as suboptimal) on some properties such as density and surface roughness, and the recall accuracy of the model was 0.98. To investigate anomalies and identify whether the process was in or out of control, Mahmoudi et al. [109] used a high-speed thermal imaging system. They validated their framework only for one specific type of defect (cavities). According to their claims, since measuring true melt pool temperatures during metal L-PBF is inaccurate, they rely on detecting deviations from reference conditions. In other words, their approach focuses on detecting “changes” in the process signature, rather than looking at absolute melt pool temperatures. After applying the RF algorithm with 100 decision trees, a 0.09 error rate was obtained.

3.1.2. Regression

The regression model predicts how independent variables affect the dependent variables in order to derive the relationship between independent and dependent variables. Regression algorithms could be chosen based on the input size and input type. Based on Fig. 9, three regression models were applied in the LPBF studies: 1) the Gaussian process (GP), 2) neural network (NN), and 3) random forest (RF). Table 17 lists the application of GP and NN in LPBF by highlighting their targeted defects.

- Gaussian process (GP)

GP is a random process that maps input (x) to $f(x)$ with a Gaussian distribution which is defined by mean and covariance. Then, the GP function is transferred to the posterior function to predict f^* for new input set (x^*) [341].

The GP is used to detect melt pool dimension [337–339] and porosity [340] in the LPBF process. Tapia et al. applied the GP model to the experimental measures of melt pool depth to predict melt pool depth in single-track experiments [338] and porosity [340]. A simulation model was developed using a training dataset 0f 26 samples, creating a variation in the process parameters (laser power, laser beam size combination, and scan speed). The GP prediction was made over processing parameters, which demonstrates the mean value and standard deviation of the prediction. Less than a 20 μm standard deviation (STD) value was reported for most of the points; however, areas with higher STD which are attributed to extrapolation are also indicated in the results. Then, the model was validated by resulting in a low mean absolute predictive error MAPE ≈ 6 μm [338]. In general, the result represented promising performance in a noisy environment [338]. In another study, Tapia et al. [340] discussed the use of the GP to calibrate a convenient criterion to avoid keyhole porous. Meng et al. [337] developed a Gaussian process regression to predict single-track depth. In the first step, the simulation of the melting process using the computational fluid dynamics (CFD) model was applied to 316 L and 17–4 PH stainless steel to generate an observation for training and validation. The observation was then imported to the GP regression model. In total, 24 observation points were created by the CFD model with variations in the laser power and scanning speed conditions ranging from 30 W to 60 W and 0.08 m/s to 0.28 m/s, respectively. Then, the covariance was defined with a combination of four kernels including laser power length-scale, laser scan speed length-scale, white kernel variance, and Matern kernel variance. These hyperparameters were optimized by MAPE using n-fold cross-validation to prevent overfitting of the model on the data. Finally, the prediction results were compared with the result of CFD predictions and experiments. The comparison indicated the agreement of the GP model with the experimental observation, which consequently could lead to a reduction in the computational costs of simulation [337]. Although progress was made based on Meng's study, more challenges should be addressed, such as calibration of the model using different layer thicknesses or materials.

- Neural Network (NN)

Although in Section 3.1.1, NN was introduced as a classification method, it could also be applied to predict continuous output as a regression estimator.

Yuan et al. [111] disclosed the application of CNN in the prediction of geometry features. The high-speed 10-bit Mikrotron EOsens MC1362A was used to capture video with a frame rate of 1 kHz during the fabrication of 316 L stainless steel parts under a variety of laser power and scan speed settings. A Keyence VR3000 3D microscope was installed to create the track height maps. The height map was firstly

Table 17
Regression models used to predict LPBF process signature.

Model	Reference	Detected output type																
		Porosity	Spatter	Balling	Plume	Delamination	Geometry accuracy	Overheating	Overhang	Surface roughness	Geometry distortion	Track dimension	Recoater blade	Part density	Abnormal process	Fatigue life	Melt pool temperature	Hardness	Melt pool dimension
GP	[337]																		*
	[338]																		*
	[339]																		*
	[340]	*																	
	[212]													*					
	[273]	*																	
NN	[111]											*							
	[11]											*							
	[78]	*																	
Random Forest	[238]																*		
	[220]																	*	
	[312]	*																	

denoised and secondly separated from the background, and then it was used to label the video data. The labeled dataset was fed into the CNN model to calculate track continuity, track widths, and width standard deviations. Prediction of track widths and classification of track continuity were evaluated. However, analysis of multi-scan track and other process signatures like density, residual stress, and microstructure needs further investigation. Williams et al. [273] applied the image-modality-to-image modality regression model to predict the flaws created during the LPBF process. In the study, an SRAS sensor was placed to record acoustic frequency from the building of ten samples. These samples were printed by

(i) titanium (Ti-6Al-4V) using the Renishaw AM250 machine,
(ii) nickel alloys (CM247-LC) using the ReaLizer SLM50 machine, and
(iii) titanium alloy contaminated by tungsten using a ReaLizer SLM50 machine.

The SRAS characteristics were then extracted using the Fourier transform. SRAS information (input) and optical micrograph (output) were fed into a multimodal image regression known as the DCB-MIR network. DCB-MIR is a type of convolutional network that builds upon ResNet [342] and DenseNet [343]. The similarity between the proposed model and the optical micrograph was evaluated using cosine similarity. This criterion showed the detection of a lack of fusion and scratches; however, some of the prominent pores were not identified because of the limited number of input samples. Additionally, Gaikwad et al. [11] applied a Sequential Decision Analysis Neural Network (SeDANN) model, which is indicated by the authors and is based on the physical knowledge of the process. In this study, SeDANN was applied to the collected data of a high-speed camera and pyrometer to predict the mean width of the track, the standard deviation of width, and the single-track continuity percentage. The prediction of SeDANN was compared with the CNN, LSTM, SVM, KNN, and ensemble of regression trees (CART), which outperformed all the other models.

- Random Forest (RF)

In Section 3.1.1, RF was discussed as a classification method, but it can also be applied as a regression technique for continuous variable prediction. In LPBF, RF regression was employed by Feng et al. [78], Kozjek et al. [238], Zhang et al. [220], and O'Loughlin et al. [312].

Feng et al. [78] used an optical tomography monitoring image to detect porosity in IN718 fabricated by LPBF. They found that using the abnormality of a single layer alone is not sufficient to reliably predict the occurrence of defects in a layer. Instead, it was found that defects in a layer may result from inappropriate parameters or anomalies in the current layer or subsequent layers. Therefore, features from the OT images of more than ten consecutive layers were extracted and fed into RF. According to the results, the RF model was able to accurately predict the average porosity of a small area ($1\ mm \times 1\ mm$) with a Pearson correlation coefficient of >0.95. In O'Loughlin's work [312], the prediction of voids was carried out by using QM Melt pool 3D and RF algorithm. Features of an infrared high-speed camera and photodiode were extracted using CT data to feed into the RF algorithm. The result indicated that the use of the extracted designed features yielded a better prediction than using raw signals. The detection of melt pool temperature was investigated in the study of Kozjek et al. [238] in which noteworthy features such as solid distribution, edge detection, laser times, and toolpath direction were used to train an RF algorithm, achieving a coefficient of determination (R^2) of 0.17 and a root mean square error (RMSE) of 27.88 K to predict melt pool temperature. On the other hand, Zhang et al. [220] applied RF to the collected melt pool intensity to predict the hardness of K438 high-temperature alloy components manufactured by LPBF. A microhardness tester was used to measure the specimens' microhardness along the *Z*-axis after they had

Table 18
Clustering models used in LPBF.

Model	Reference	Detected output type																		
		Porosity	Spatter	Balling	Plume	Delamination	Geometry accuracy	Overheating	Overhang	Surface roughness	Geometry distortion	Track dimension	Recoater blade	Part density	Abnormal process	Fatigue life	Melt pool temperature	Hardness	Melt pool dimension
K-means	[44]					*			*				*						
	[344]					*			*				*						
	[59]					*			*				*						
	[155]				*														
	[212]													*					
	[338]											*							
	[24]		*																
Agglomerative	[108]														*				
SOM	[217]	*																	
DBSCAN	[125]																		*

been ground and polished on the side surfaces. To form a data set, the hardness data was correlated with the melt pool radiation intensity characteristics at the corresponding locations. After applying the RF model to the data, a coefficient of determination (R^2) of 0.91 was achieved.

3.2. Unsupervised learning

Unsupervised learning allows users to cluster unlabeled data or to identify the main feature of data without any label, respectively known as clustering and data reduction methods. According to LPBF publications (Fig. 9), clustering methods used in this field are limited to K-means, agglomerative, Self-Organizing Map (SOM), and density-based spatial clustering of application with noise (DBSCAN) algorithms, while principal component analysis (PCA) and singular value decomposition (SVD) have been applied for data reduction.

3.2.1. Clustering

The clustering technique groups the unlabeled dataset according to their similarity. According to Fig. 9, K-means, agglomerative, SOM, and DBSCAN were applied in the LPBF studies. Table 18 lists the recent application of the clustering algorithms in LPBF, which was practiced to predict different defects.

- K-means

K-means is a clustering algorithm to group the unlabeled dataset by minimizing the distance of the points in one cluster using four iteration steps:

(i) Selection: choosing the K centroids (center of the cluster) randomly,
(ii) Expectation: assigning each data point to its nearest centroids,
(iii) Maximization: calculating the average of all points grouped in one cluster and then calculating a new centroid, and
(iv) Repetition: Repeating the algorithm until no changes have been observed in the centroid positions.

K-means has a relatively simple implementation, and it could guarantee convergence. However, selecting K quantity manually and being dependent on initial values may restrict the use of K-means.

K-means has been applied in LPBF to classify plumes [155], overhang structure [44,59], and delamination [44,59]. In Scime's study, the k-means algorithm was applied to detect powder-spreading anomalies. The captured images were used to train and test the model. Six filters (Gaussian, Difference of Gaussian (DoG), Oriented Line Detectors, Oriented Edge Detectors, debris, and Streak Detectors) were optimized and then convolved with 2402 image patches, as shown in Fig. 24. b. Similar features were grouped by the k-means algorithm (Fig. 24. c). Then, the fingerprint of each patch was calculated by the histogram (Fig. 24. f) and saved in a fingerprint table (Fig. 24. g). After that, the top three matches of fingerprints were selected and weighted to detect anomalies (Fig. 24. i and Fig. 24. j). The algorithm was applied on 29 builds printed using AlSi10Mg, Inconel 718 (two powder types), Ti-6Al–4V (four powder types), stainless steel 17–4, stainless steel 316 L, and a bronze alloy. The confusion matrix showed that 95 % of anomaly cases were correctly classified. Additionally, the Hamerschlag Hall model, horizontal and vertical tensile bars, and Impeller blades were analyzed to detect delamination and overhang structure, part failure, and recoater blade impact, respectively. The algorithm was a robust and valuable tool and had a relatively low computational cost, resulting in fast and accurate anomaly identification to tackle the limitation of the closed-loop controller [44]. Nonetheless, switching the current algorithm to the deep learning method could be suggested to improve its performance for integrating the model into the controller.

Colosimo et al. [59] investigated the effect of the hot spot and heated

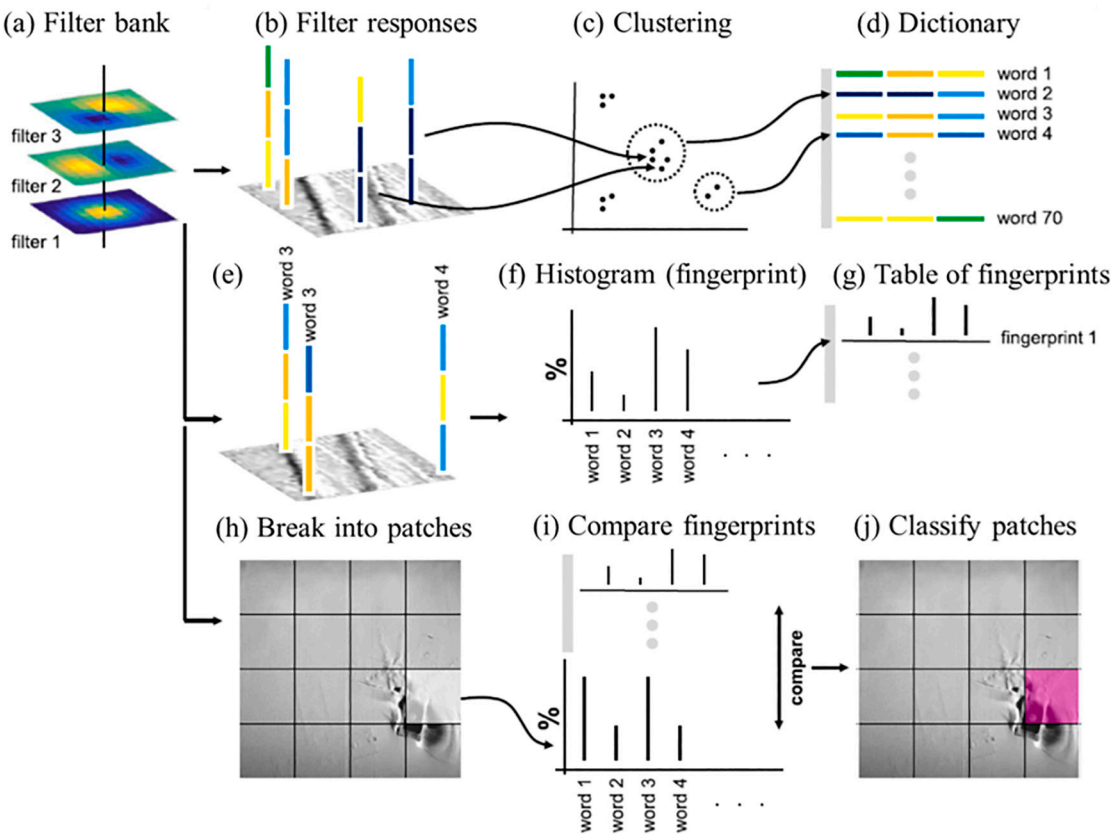

Fig. 24. Use of K-means by Scime et al. [44] in LPBF.
(Source: Republished with permission of Elsevier, from [44])

features (acute corners, overhang zones) by printing triangular-shaped features. The analysis showed that the laser heat zone could change the cooling rate and solidification, leading to local geometrical deformation. Colosimo's team has improved their research by introducing new methods to analyze big video data captured by a CMOS camera, which was installed off-axially in the Renishaw SLM system (AM250). The video images were captured from the melt pool of cylindrical coupon samples printed using AISI 316 L powder. Then, three sizes of

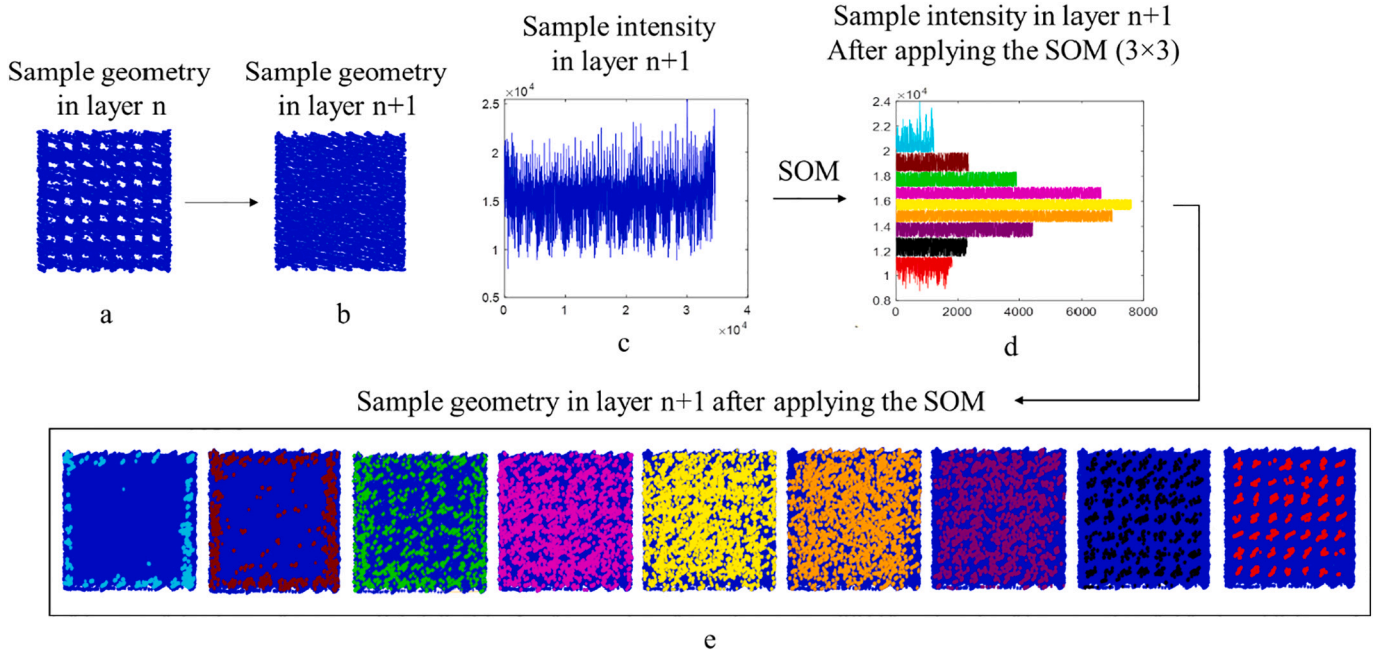

Fig. 25. a) sample geometry with artificial defects in layer *n*, b) geometry of capping layer of defects (layer *n + 1*), c) light intensity signal of capping layer of defects (layer *n + 1*), d) light intensity signal of layer *n + 1* after applying the 9 clusters SOM, and e) geometry of capping layer (*n + 1*) after applying the 9 clusters SOM
(Source: Republished with permission of Elsevier, from [217])

Table 19
Data reduction and feature extraction models used in LPBF.

PCA	[47,59,107,124,140,265,266,344]
SVD	[212,219]

the hotspot (small, medium, and large) were randomly injected into the cylindrical sample using the sigmoid pattern to generate a realistic hotspot over time. The T-mode and ST-PCA (which will be discussed in Section 3.2.2) were used to classify local hot spots. These PCA algorithms were coupled with the clustering-based alarm rule by either the recursive or moving window schemes. Finally, K-means was applied to the classified data to detect and localize the existence of hot spots. Under in-control conditions, only two clusters were identified, referring to the background pixels and the normal melting area. In the presence of a hot spot, more than two clusters were expected and obtained, which indicated the location of hot-spots [59]. Recently, K-means also was applied by Lin et al. [24] to cluster motion features under print parameters variation to eventually find its correlation with spatter.

- Agglomerative hierarchy

Agglomerative hierarchy is a hierarchical clustering approach. In this method, a bottom-up approach is used in which each observation is labeled as a cluster, and subsequently, pairs of clusters are merged. To decide which clusters should be combined, a dissimilarity measurement is needed, which is achieved by an appropriate metric and a linkage criterion.

1- The metric is defined based on the shape of the cluster. Some common metrics are Euclidean, Squared Euclidean, Manhattan, maximum, and Mahalanobis distances for numeric data. Hamming and Levenshtein distances are also applied in text and non-numeric datasets.
2- The linkage criterion measures the distance between two sets of observations. Some popular linkage criteria are complete-linkage, single-linkage, unweighted average linkage, and weighted average linkage clustering [345].

The agglomerative hierarchy was applied in the study of Fathizadan et al. [108]. First, melt pool images were taken from the fabrication of 12 Inconel 625 parts. These parts were printed with different scan paths, laser power, and scan velocity to create normal and anomaly processes. After that, the main features of melt pool images were extracted using the CAE network. The extracted features were fed into an agglomerative algorithm to automatically distinguish between anomalies and normal processes. Euclidean distance was used as a metric, and single, complete, average, and Ward were applied as linkage criteria. Next, the multivariate profile monitoring approach was used to monitor the process's stability. Finally, the result of the study was compared with numerical results to prove the accuracy of the proposed algorithm.

- Self-Organizing Map (SOM)

A SOM maps high-dimensional data into lower-dimensional spaces while maintaining the topological relationships. The algorithm clusters the dataset in five steps:

1- Initialization: weights and biases are chosen randomly.
2- *Competition:* competition phase between neurons leading to map input space to the discrete output space.
3- Cooperative: lateral interaction or topological neighbourhood is calculated, and the winner neuron is chosen.
4- Adaption: weights are updated
5- Continuation: keeps returning to step 2 until convergence [346].

This algorithm was applied once in the field of LPBF. Taherkhani *et al. [217]* applied the SOM algorithm to detect the lack of fusion from the deviation of light intensity collected from the photodiode. First, the study explored that the successive layer of lack of fusion defects could be used to detect the underneath defects. Then, two sets of experiments were designed as 1) artificial seeding defects and 2) randomized defects.

- Artificial seeding defects were designed by embedding cylindrical, spherical, and cubical voids ranging in different sizes and distributions in the coupon samples (Fig. 25(a)).
- Randomized defects were created by reducing energy input.

After collecting light intensity signals and documenting the dataset (Fig. 25(b) and Fig. 25(c)), the samples with artificial defects were used to identify the optimum number of SOM clusters. Thus, the intensity signal was tested with different cluster numbers and finally clustered into nine groups (Fig. 25(d)) and each cluster was mapped to geometry (Fig. 25(e)). The geometry of the lower cluster showed the position of lack of fusion (Fig. 25(e) right image). By comparing the result of the prediction algorithm and experimental CT data, artificial defects that were larger than 100 μm were identified. The result of randomized defects disclosed a sensitivity of 61 %- 94 % and specificity of 69 %- 93 %, depending on the process parameters.

- Density-based spatial clustering of application with noise (DBSCAN)

DBSCAN (Density-Based Spatial Clustering of Applications with Noise) is a density-based clustering algorithm that groups together dense regions of data points in the feature space and separates sparse regions. The algorithm starts by selecting a random data point as the seed for a cluster and then considers all points within a specified radius (epsilon) of the seed point as its neighbours. If adequate points (min-samples) are found within the epsilon radius, a cluster is formed, and the process is repeated for all the data points in the cluster. Points that are not within any cluster are considered noise and treated as outliers. This algorithm is useful for discovering clusters in large, complex datasets where clusters have a non-linear shape or are of varying densities. This method was applied to detect the melt pool area by Vasileska et al. [125]. In the work of Vasileska et al. [125], raw melt pool images were captured and then DBSCAN was applied to separate the melt pool zone from the background. The melt pool zone was then analyzed by other algorithms to detect its geometry.

3.2.2. *Data reduction and feature extraction*

Data reduction is typically applied to pre-process the dataset for extracting the significant features of data. According to Fig. 9, principal component analysis (PCA) and singular value decomposition (SVD) are the techniques that are mainly used for data volume/dimension reduction purposes. Table 19 lists the studies associated with the application of data reduction techniques in LPBF.

- Principal component analysis (PCA)

PCA is a clustering algorithm for finding significant features of data using the covariance matrix. After calculating the covariance matrix of data, the eigenvalue and eigenvector are also calculated. Afterwards, the eigenvalues are sorted in ascending order. An eigenvector associated with the highest eigenvalue is selected as the principal component of the data, and eigenvectors with lower eigenvalues will not be considered [347].

PCA is commonly applied to extract principal components of the dataset in LPBF [47,59,107,124,140,266,344]. For example, in Zhang's study [47], SVM was adopted with and without applying PCA to extract plume and spatter information. The aim of the investigation was to predict three classes of quality in single tracks from balling/lack of fusion to two continuous tracks with different widths which originated

from various levels of power in scanning. The comparison disclosed that pre-processing the data using PCA by selecting 33 input features, led to improving accuracy (denoted by mean classification accuracy metric) of single track classification from 89.7 % to 90.1 % while applying PCA by choosing 17 input features resulted in decreasing the accuracy from 89.2 % to 88.3 % [47]. The study showed that PCA might negatively influence performance if too many features are eliminated. Basic PCA was applied by Kwon et al. [107], Elwarfalli et al. [140], Shevchik et al. [266], and Grasso et al. [344]; however, more complex types of PCA were proposed by Colosimo et al. [59]. Colosimo et al. [59] applied and compared two types of PCA: spatially weighted PCA (ST-PCA) and T-mode PCA to detect local hot spots. ST-PCA was found to be more effective and faster than T-mode PCA. ST-PCA method was also adopted by Yan et al. [124], along with basic PCA. Recently, the application of PCA was investigated by Xu et al. [265]. The PCA was applied on the laser ultrasound dataset to extract the first three components which then were fit to ANN discussed earlier.

- Singular value decomposition (SVD)

The singular value decomposition is a clustering method to decompose a matrix (A) into two orthogonal (U and V) and one diagonal matrix (S) given by [348]:

$$A_{m\times n} = U_{m\times n}\Sigma_{n\times n}V^{T}_{n\times n} \tag{2}$$

The diagonal matrix (Σ) is a singular value. The singular values are sorted in ascending order and used to approximate A [348].

SVD was applied by Okaro et al. [219] to reduce the data dimension. The randomized SVD was used on two photodiodes datasets, which were captured in two different wavelengths: (i) thermal radiation (1100–1700 nm) and (ii) plasma emission (700–1050 nm). The SVD was applied to reduce the dimension of the data corresponding to 25 Ultimate Tensile Strength (UTS) tests, and then two Gaussian Mixture Models were trained by the extracted data to identify fault, resulting in 77 % success in detection [219].

- New data reduction approach

Recently, a new feature extraction approach was investigated by Imani et al. [84]. Four types of features:

1- Statistical
2- Multifractal
3- Graph theory, and
4- Combination of multifractal and graph theory

were applied to DSLR camera images captured from the Titanium alloy (Ti-6Al-4V) cylindrical parts. Six low energy density scenarios were considered by decreasing laser power, increasing hatching distance, and increasing scan speed. The variation of print parameters was analyzed by micro CT- scan. After applying each extraction method, the features were then classified by SVM, complex tree, linear discriminant analysis, K-Nearest neighbourhood, bagged trees, and feedforward neural network. To evaluate each algorithm, F-score was used, as shown in Table 20. The result showed that the new type of feature extraction could improve the identification of the lack of fusion pores [84]; however, the applicability of the method should be evaluated on other porosity types in the future.

3.3. Reinforcement learning

Reinforcement learning is a type of learning which is based on interactions with the environment. The environment is typically explained as the Markov decision process (MDP) [349] and modeled with the following characteristics:

- $\mathscr{S}$: a set of environment and agent states
- $\mathscr{A}$: a set of actions
- $P_a(s,\acute{s})$: probability transition at time t from state s ($s\in\mathscr{S}$) to state $\acute{s}$ under action α ($\alpha\in\mathscr{A}$) given by:

$$P_\alpha(s,\acute{s} = P_r(s_{t+1} = \acute{s} \mid s_t = \mathrm{s}, \alpha_t = \alpha) \tag{3}$$

- $R_a(s,\acute{s})$: immediate reward after the transition from s to $\acute{s}$ with action α

At each time, the agent receives the current state (s_t) and reward (r_t). On the other hand, the agent selects an action α_t from the $\mathscr{A}$ and sends it to the environment. Then, the environment moves from the current state (s_t) and current reward (r_t) to the new state (s_{t+1}) and new rewards (r_{t+1}). The goal of MDP is to learn a decision policy defined as Eq. (4) to maximize the reward function [350].

$$\pi : \mathscr{A}\times\mathscr{S}\rightarrow[0,1], \pi(\alpha,s) = P_r(\alpha_t = \alpha \mid s_t = \mathrm{s}) \tag{4}$$

Reinforcement learning is commonly applied in many engineering fields such as game theory, swarm intelligence, and welding. However, only two studies were conducted using the RL in LPBF by Knaak et al. [97] and Wasmer et al. [267]. Knaak et al. [97] conducted a study to measure surface roughness by CNN and RL algorithms. First, during the fabrication of Inconel 718 cubical samples built by nine different sets of print parameters, four photos were taken at different exposure times (120.2, 132.2, 144.2, and 156.2 ms). Images were then merged into one single HDR image. In the next step, Grey-scale HDR images were segmented into small image patches (96 × 96 pixels) using a sliding window approach. Then, each patch was labeled based on the measured roughness (S_a) using white light interferometer (WIM) and classified into five classes: 1) very low roughness ($S_a\in(0;3]$), 2) low roughness ($S_a\in(3;5]$), 3) medium roughness ($S_a\in(5,12]$), 4) high roughness ($S_a\in(12,20]$), and 5) undefined roughness (surface distortion). Also, data augmentation technique was used to reach more dataset. Then, inputs (HDR patch images) and output (the measured surface roughness) were fed to the CNN model and trained using 4-fold cross validation. Although the model had difficulties to distinguish between class 1 and class 2, the result of CNN showed the overall accuracy of 91 % to identify mean surface roughness and percentage of defective area. In the next step, according to the information gained from CNN model, the RL was designed. In RL phase, the current and agent actions were defined as follows:

1- The current action was explained as $s_t = \left(P_t, v_t, S_{amean,t}, \delta_t\right)$. P_t, v_t are respectively laser power and scan velocity and $S_{amean,t}$ (mean surface

Table 20
Accuracy of classifiers using different feature extraction methods [84].

Model	Statistical features	Graph theory features	Multifractal and lacunarity features	Combination of multifractal and graph theory
SVM	55.58 %	71.94 %	76.16 %	89.36 %
Complex tree	54.10 %	68.02 %	68.60 %	79.98 %
Linear discriminant analysis	52.72 %	63.22 %	63.02 %	82.16 %
K-Nearest neighbourhood	56.62 %	67.66 %	70.38 %	78.60 %
Bagged trees	51.06 %	72.50 %	72.64 %	85.86 %
Feedforward neural network	49.66 %	64.62 %	66.54 %	84.40 %

roughness) and δ_t (percentage of defective area) were estimated by the CNN model. For choosing an action, the model-based RL (MB-RL) [350] approach was chosen.

The reward function was defined to allocate a negative reward of −10,000 when it identified $\delta_t > 10\%$, a positive reward of +2000 for the combination of $\delta_t < 10\%$and $S_{amean,t} < 4\ \mu m$.

2- Agent action was defined as sets of tuples that consisted of a possible combination of laser power and scan velocity to increase, decrease, or apply no change to the energy density as:

Based on the current (s_t), and a given action (α), a random forest method was selected to establish a dynamic model to predict the next state (s_{t+1}). The result indicated that MB-RL optimizes the process parameters, resulting in a low surface roughness of 3.38 μm. The study also verified the relationship between surface roughness and overall part density to show the possible applications of the proposed algorithm in the industrial domain.

Additionally, Wasmer et al. [267] followed their studies [266,268] (discussed in Section 3.1.1) by applying the RL model based on the labeled data extracted from the signal of FBG. The first step involved capturing FBG data during the print of cubic samples with three quality levels (poor, medium, and high) created by changing the scanning speed. Then, the FBG data was fed to CNN to classify its features (explained in Section 3.1.1) [266,268]. Lastly, the classified features were incorporated into the model-free RL (MF-RL) [350] for classifying the parts' quality. After comparison with ground truth quality levels obtained through light microscope images of parts' cross-section, the accuracy of 74 %, 79 %, and 82 % for poor-quality, medium-quality, and high-quality levels were achieved.

4. Discussion

Laser powder bed fusion (LPBF) is a complex and multi-physics process in which various independent and interconnected physical phenomena are involved. This process is capable of producing intricate and complex parts with unique properties that depend on factors like processing parameters and microstructure. To analyze and predict different aspects of this process (including part quality, defect occurrence, and optimal processing parameters), using in-situ devices and analyzing their dataset is essential which were discussed in-detail in Sections 2 and 3. But, this section will explore the critical review of various in-situ sensing equipment used in LPBF and the different ML models applied to the in-situ dataset of LPBF processes, by comparing their strengths and limitation.

4.1. In-situ sensing equipment implemented in the LPBF systems

Two categories of in-situ sensors for LPBF were defined as radiative and non-radiative in Section 2 and these categories were divided into sub-categories. As radiative sensors, cameras, X-ray imaging, ICI, photodiode, pyrometer, fringe projection, and recoater blade sensors were explained, on the other hand, acoustic, thermocouple, and displacement sensors were discussed as non-radiative sensors. Here more discussion on their advantages and disadvantages are provided in the following paragraphs with examples of studies using the mentioned sensing systems and summarized in Table 21.

Camera sensors operating in visible to NIR wavelengths are beneficial in terms of cost and integration to industrial systems due to the suitable size of sensors compared to thermal camera sensors [351]. On the other hand, lighting conditions needed for higher-quality imaging might complicate the integration of the camera into printing machines. These sensors are mainly applied for imaging/video imaging of the

Table 21
Strengths and limitations of in-situ sensors installed in LPBF.

Sensor	Strengths	Limitations
Camera (visible to NIR)	Reasonable cost Melt pool size identification Easy integration into machines Highly practicality for industrial applications	Field of view and resolution restrictions Need to light condition and filters
Thermal Camera (NIR to LWIR)	High practicality for industrial applications Detection of temperature Non-invasive Cost-effective	Low temporal resolution Expensive Difficult calibration Precise time synchronization between process and data acquisition is needed
ICI	High-resolution and high field of view Able to detect minor height deviations in powder bed	Difficult placement of sensors Need to raster scan (time increase)
X-ray Imaging	High spatial and temporal resolution Visualize 3D reconstruction of part	Impractical in AM Expensive
Photodiode	Provide melt pool 2D intensity map (on-axial) Provide whole area 2D intensity map (off-axial) (Both are enabled by the synchronized scanner)	Contaminations of the sensor by fume and spatter Its off-axial installation has inaccurate intensity data due to gathering by-products and space radiations too.
Pyrometer	More robust to distance from the melt pool variations Good for point-wise inspection Detection of temperature Adequate sensitivity to process deviations	Contaminations of the sensor by fume and spatter
Fringe projection	High-resolution High-accuracy 3D measurements	Pre-calibration Sensitive to setup arrangement Limited field of view
Recoater blade-mounted sensor	Can measure a height map of the powder bed	Complexity is added to the machine which makes the maintenance of the machine more difficult
Acoustic	Low cost Low power supplies Easy to use	Sensitive to noise Large memory for storage is needed Amplifier is needed Performance at high frequencies reduces
Thermocouple	Wide temperature range Low initial cost Fast response Small size	Difficult recalibration Amplifier is needed Require expensive TC wire from the sensor to the recording device Fragility
Displacement	Tolerant to high magnetic fields measurement range is high	Calibration is needed Sensitive to temperature and vibration High cost

process to inspect surface-level defects, melt pool geometry, melt pool size, and location of defects. In most cases, they are used in off-axial arrangements to control a wider area of the build or to capture images from other aspects of the LPBF process, such as spatter and plume [47]. The high spatial resolution of these cameras also significantly aids the capturing of these printing by-products (spatter and plume). But, the challenges with this type of sensor should be considered since they are associated with the regulation of the field of view and resolution [8,10] and the need for image processing of the raw data for extraction of relative information for various objectives [43,44,47]. In most cases, installing additional equipment like lenses [63,93] and lighting setups [54,55] are also essential to capture high-quality images. Compared to visible-NIR camera sensors, a thermal camera is more expensive, and integration of it into commercial systems could be more difficult due to the bigger size of this type of camera and the required lighting conditions. However, thermal cameras are one of the most essential sensing methods for temperature evolution, cooling rate, and melting process imaging/ video imaging. Since thermal history is a major quality-affecting parameter in LPBF, a notable endeavour has been focused on the integration of thermal cameras for quality control and monitoring. Thermal cameras could provide important information regarding the location and size of anomalies (through 2D heatmap), melt pool geometry [131,139], spatter [132] and droplets detection [134], and temperature extraction [136,154]. The operating wavelengths also impact the functionality of these sensors. For instance, it has been reported by studies that short wavelength results in more accurate temperature data extraction of LPBF due to concerning less emissivity error [352]. The long wavelength, on the other hand, is stated to be more optimal for video imaging owing to its practicality in higher temperature ranges [352]. For instance, an LWIR thermal camera was also employed in Krauss et al. [148,158] and Schilp et al. [144] studies for monitoring the temperature gradient and thermal inhomogeneity. But in general, similar to visible-NIR camera sensors, thermal camera also encounters imaging calibration, which is very challenging. Like IR cameras, thermocouples could also be beneficial for disclosing thermal information in a wide temperature range (up to 2500 °C). Although the application of thermocouples in modeling is popular, as an in-situ monitoring device, the thermocouple is used in a few studies of LPBF and it is mostly implemented with other types of sensors like IR cameras [133] and strain gauges [278]. Some potential reasons could be 1) it requires calibration to keep its accuracy over time and the calibration is costly and time-consuming and 2) it needs an amplifier. On the other hand, ICI could eliminate the need for location coordinate calibrations of the data, since it must be installed co-axially [174]. The ICI sensing system allows for fast and time-efficient data acquisition of the morphology of powder and materials [166]. This method enables higher resolution monitoring which has resulted in deflection detection as small as 50 μm (reported in [174]). It was demonstrated in this study that this sensing approach has exceptional performance in powder bed height deviation detection [174]. It also has high practicality in terms of the corporation to control loop systems [351]. ICI has a downside of raster scanning needed after melting [352] in cases of surface topography monitoring in both horizontal and vertical directions as investigated by DePond et al. [167].

Another commonly used sensor for thermal inspection of the LPBF process is a photodiode. Photodiode sensors operate by capturing the light intensity radiation in the visible range during the process which are directly correlated with the temperature of the melt pool. Therefore, it has drawn attention to temperature and thermal monitoring without the employment of more expensive thermal camera sensors. It should also be considered that data processing of photodiode signal would be faster (lower dimension than image data) which makes it a feasible candidate for real-time quality control and integration into closed-loop feedback. On-axis mounted photodiode sensors could be synchronized with the scanner's position to provide a 2D intensity map of the melt pool from which information regarding the melt pool size [58] and the location of thermal anomalies such as overheating could be drawn [52,53]. Geometry and dimensional accuracy of the build is also explored using photodiode sensors (mapping of signals could be obtained due to coordinate data recording enabled by synchronized scanners of photodiode sensing systems). The latter was investigated in Kruth et al. [10] and Baumgartl et al. [131] study with the aid of a camera. Although the off-axis configuration of the photodiode also could be adopted for monitoring the whole area of the build but could lead to inaccuracy in melt pool intensity data since any environmental light intensity, whether from laser irradiations or ejected particles, could be recorded by the sensor. Accordingly, the main interest in photodiode utilization in LPBF is for pointwise and small region thermal information gathering, which in contrast thermal cameras are not able to achieve accurately and effectively [353]. But in general, photodiode sensors are prone to noise signals, consequently, data processing and filtering are required. Regarding other thermal sensing techniques, pyrometer sensors; which share many similarities with photodiodes; are also highly practical in LPBF applications. Pyrometers like photodiodes capture light-intensity radiation but in IR wavelengths. Therefore, a pyrometer is another effective sensing method for the extraction of temperature in the melt pool and build area. In fact, pyrometers made from a configuration of two or higher numbers of co-axis photodiodes significantly improve the temporal resolution of the sensing. This in turn enables accurate data gathering of thermal indicators such as overtime thermal intensity map evolution and temperature variations of the melt pool. Pyrometers also show notable merits in pointwise monitoring [353]. It was reported in a comparative investigation between pyrometer, camera, and acoustic sensors that the pyrometer demonstrates adequate sensitivity to process deviations while showing less sensitivity to location and distance from the monitoring area [354]. This would be highly advantageous since system calibrations and mounting complications would have less impact on the accuracy of captured data. Furthermore, co-axial mounting of pyrometers could be significantly effective for melt pool size identification because it allows for the gathering of the geometrical data by the scanner. Nevertheless, the high chance of noise signals inclusion is still a challenge in this sensing system too, like photodiodes.

It was demonstrated in the previously mentioned comparative study that although acoustic sensors show high dependency on system placement, they have the highest sensitivity to process deflections (between camera and pyrometer) [354]. Additionally, acoustic sensors are relatively inexpensive compared to other sensing techniques and are easy to implement on both in-house and commercial LPBF systems without interfering with the process. But this type of sensor is sensitive to undesired background noise and their performance drops at higher frequency ranges. To solve these issues, most of the researchers applied the low-pass filter to block high-frequency signals like noise. In the LPBF's study, the Butterworth low-pass filter has been mostly used [2,136,253–255]. The Butterworth filter has the capability to maximally flatten response within its pass-band resulting in no response ripples in its bandwidth (For more information, refer to [355]). In another aspect, the acoustic sensor could only provide information about the sound wave propagation which could be practical for early detection of porosity [252,253,264–273,254,287,288,255,258–263], but it is not enough to identify the cause of other types of defect. In contrast to the acoustic sensor, X-ray imaging is capable of capturing data for the detection of various phenomena, due to its high spatial and temporal resolution. But, X-ray imaging is mostly impractical for commercial LPBF applications because of the extensive cost of this sensing system compared to any other sensing techniques that are easily adaptable by industrial machines. In addition, its integration is much more complex than other sensors due to the bigger size of these devices and the complex calibration settings needed. Although these features make this setup not feasible for commercial systems, multiple attempts have been made to utilize it in in-house LPBF systems mainly due to its special capability of sub-surface anomaly detection. X-ray imaging also enables the 3D imaging of the build area. In addition, it could be practical for the inspection of spatter characteristics such as the direction of ejection [1].

Similar to the X-ray imaging system, the full adoption of displacement sensors, fringe projection, and recoater blade-mounted sensor in LPBF is difficult. The displacement sensor has some challenges such as 1) its dataset cannot provide information about LPBF challenges like porosity and cracks, and 2) its response is affected by vibration and temperature change which are two inseparable elements of LPBF. However, since it could measure the height, width, and thickness of an object by determining the amount of displacement of that object, its application was reported to disclose information about layer thickness and geometry distortion. Besides, fringe projection and recoater blade-mounted sensors could capture information about diffuse reflection surfaces like a height map of the powder bed [356]. Challenges of fringe projection are i) its need to pre-calibration to measure high resolution and accurate dataset [357] and ii) its sensitivity to optical setup arrangement, uneven illumination distribution, and surface reflectance which could easily lead to inaccurate image reconstruction [358]. On the other hand, the recoater blade-mounted sensor adds more complexity to the LPBF system for maintenance.

Several sensors and their applications were discussed in this study; however, the information collected using an individual sensor is often incomplete and may be noisy, making it challenging to monitor the process effectively. Thus, sensory data fusion provides a solution to this challenge by combining data from multiple sensors to create a more accurate and complete picture of the manufacturing process. Sensory data fusion [79] involves the integration of data from multiple sources to form a unified representation of the entire process which could ensure the quality of the recorded data by minimizing the noise and errors that arise from the individual sensor, while also increasing the amount of information available for quality assurance algorithms. There are three main approaches to performing sensor fusion [359], as below:

(i) Signal level fusion where the raw data collected from multiple sources are combined at the source level, which may be transmitted for further feature extraction,
(ii) Feature level fusion which involves extracting relevant features from the data collected by each sensor and then fusing these features into a single feature vector, and
(iii) Decision level fusion where models are trained on sensor-specific features delivers independent decisions, so a weighted group vote renders the final decision.

The application of data fusion is a pretty new topic in LPBF. Recently, Harbig et al. [299] showed the use of sensor-level data fusion for evaluating data from photodiodes, high-speed camera, and thermal camera for defect detection. Harbig's approach involved first mapping the sensor data to the melt-pool position, then reducing the mapped data to signal indicators based on process knowledge about defect causes and qualitative analysis of the data. Then using threshold filters absolute fluctuations, dynamic and short fluctuations were identified via a quantitative evaluation. Before a two-stage data fusion was combined, filter indicators from individual monitoring system were compared to determine the detection qualities of individual monitoring systems. One of the main challenges of sensory data fusion is the need to synchronize the data from different sensors. The sensors may have different sampling rates or different time stamps, making it difficult to combine them into a unified representation. To overcome this challenge, advanced algorithms [360] such as the Kalman filter, particle filter, and artificial neural networks are used to align the data, allowing for the accurate fusion of the information. As an example, Petrich et al. [361] used a decision-level data fusion technique through a neural network to combine multiple sensor data such as layer-wise imagery, acoustic, multi-spectral emissions, and scan vector data for flaw detection in the process. Then, the neural network is trained to make decisions by weighing the outputs based on the confidence from the network.

4.2. Machine learning models applied to in-situ data of LPBF

In this study, three categories of ML models, including supervised learning, unsupervised learning, and reinforcement learning, were discussed in Section 3. In the following sub-sections, each of these models will be critically summarized and reviewed:

- Supervised learning

Supervised learning is trained using the labeled dataset for which typically CT-scan has been used. Two supervised learning groups are classification and regression which are divided based on their type of dataset, as discussed in Sections 3.1.1 and 3.1.2. Due to the characteristics of these methods, classification was applied mostly to detect porosity, spatter, and plume, while regression was usually used to predict track dimensions and melt pool dimension. However, in general, the choice between these models depends on the available sensor data and the specific problem being addressed. Table 22 specifies the strengths and limitations of classification and regression methods.

From the classification family, SVM, NN, ANFIS, KNN, and RF were applied. SVM, a powerful classification model, can be used in LPBF for identifying defects such as spatter [43,47], and porosity [43,54,61,84], as well as optimizing process parameters to minimize the occurrence of these defects [2]. SVM performs well when the data is high-dimensional and well-separated. However, this algorithm can be sensitive to noise and may lead to poor generalization of unseen data. To minimize this challenge, the kernel function has to be carefully selected which was discussed in the study of Ye et al. [2]. The computational cost of SVMs can also be a challenge, especially for large datasets or high-dimension features [362]. A similar problem is involved with the use of Random Forest because multiple decision trees must be built and evaluated when

Table 22
Strengths and limitations of ML applied to in-situ LPBF dataset.

Model	ML category	Strengths	Limitation
SVM	Classification	Effective for high-dimensional data	Computationally expensive for large datasets Sensitivity to noisy data Careful selection of kernel function requires
NN	Classification Regression	Effective for nonlinear datasets Performs well with a large dataset Highly effective for images	Difficult to train A large number of hyperparameters
ANFIS	Classification	Effective for nonlinear datasets Performs well with a large dataset	Difficult to train A large number of hyperparameters
KNN	Classification	Easy to implement Requires minimal training	Computationally expensive for large datasets Sensitivity to the choice of k
RF	Classification Regression	Less sensitivity to noisy data Provides interpretable results	Computationally expensive for large datasets
GP	Regression	Effective for nonlinear datasets Performs well small to medium-sized datasets	Computationally expensive for large datasets Sensitivity to the choice of kernel function Sensitivity to hyperparameters selection

working with a large dataset, while it could model a smaller dataset more effectively even with the existence of noise [335], which could be particularly relevant for LPBF where the process is highly stochastic. The computational challenge of SVM and RF could be effectively addressed by neural network models because the NN model is powerful in situations where the relationship between the inputs and output is complex and non-linear. Since relating the process parameters, along with the complex recorded monitoring data to predict the quality of the fabricated part could be addressed by NN, this method was successful in the detection of porosity [66,70,84], and surface roughness [97,98]. Deep NNs (e.g., CNN, RNN, LSTM, and SNN) are another type of neural network that is particularly effective in situations where the data is in the form of images like melt-pool images or other spatial representations like acoustic sensor datasets. They could be used to quickly identify and localize defects in recorded in-situ images with high accuracy. However, training the NN model could be difficult due to the choice of selecting a large number of hyperparameters such as the number of neurons, depth of the network, loss functions, etc., making this approach prone to overfitting [330]. Also, this method requires a large amount of data, which at first glance may seem ideal for the LPBF process due to the nature of the process. But, the collected data are usually not diverse, as such different experiments need to be conducted under varying conditions to acquire a large dataset, which could be expensive and laborious. Additionally, the complexity of NNs can make them difficult to interpret, and it may be challenging to understand how the model arrived at a particular prediction [330]. So, other options could be ANFIS and KNN. The neural-fuzzy inference is a hybrid model that combines the benefits of both neural networks and fuzzy logic. This method can provide interpretable results. The fuzzy rules generated by the model can be used to explain how the input parameters affect output quality [332]. KNN is also straightforward to implement since it is a non-parametric algorithm that does not make any assumptions about the distribution of the data. On the other hand, KNN requires minimal training, making it well-suited to small datasets and a great choice for LPBF [11,84,109,234]. However, for large datasets, the method may become computationally expensive as the distance between each test point and all training points needs to be calculated [334]. Overall, the most suitable classification model for a given task is dependent on the characteristics of the dataset, the available computational resources, and the trade-off between accuracy and interpretability [341]. It is crucial to apply various models and evaluate their performance on a validation set before determining the ultimate model.

As regression methods in LPBF, GP, NN, and RF were explained in Section 3.1.2. The GP model has the potential to predict different process signatures such as melt pool dimension and porosity using a camera, temperature and thermal gradients by ICI, porosity using X-ray imaging, and temperature of the melt pool based on the thermocouple dataset. A key feature of the GP model is its ability to model complex nonlinear relationships. Additionally, it performs well on small to medium data sets. This model is also useful for determining the uncertainty of estimates, which is crucial for process control decisions [341]. However, few studies have used this model in LPBF [212,337,339], possibly due to its computational cost for large datasets as well as its high dependence on the choice of kernel function and hyperparameters. These challenges could be addressed by the neural network (NN) regression model due to its excellent capability to analyze complex nonlinear data, high-performance results on large data sets, ability to handle high-dimensional input data, and ability to model both spatial and temporal variations [363]. The NN regression algorithm is suitable to predict signatures such as geometry dimension, width dimension, and single-track continuity. For using NN, its architecture and hyperparameter selections should be carefully optimized, since it is sensitive to those factors [363]. Another alternative could be the use of an RF model which could overcome the challenges of GP and NN because RF is simple to use, requires little hyperparameter tuning, is capable of handling large and high-dimensional datasets, and has interestingly the ability to rank feature importance for controlling the LPBF process [335]. According to its advantages, the attention to this method has become popular recently to detect porosity [78,312], melt pool temperature [238], and hardness [220]. But, like other ML models, RF also has some limitations. The downside to this method is that it is not as effective as other methods on smaller datasets, and it has difficulty capturing complex nonlinear relationships which is not a challenge for NN.

- Unsupervised learning

Unsupervised machine learning is a technique used to analyze data without the use of labeled examples. This ML method has been used to analyze data generated by the LPBF process for identifying relationships between the print parameters and output properties and reducing the data dimensions by clustering and data reduction techniques.

Clustering methods applied in LPBF were K-means, SOM, Agglomerative, and DBSCAN. As previously discussed, the K-means algorithm is fast and easy to implement, and it can handle relatively large datasets; however, it is quite sensitive to initial centroids initialization. Also, it requires the number of clusters to be specified beforehand [364], which could require either significant knowledge of the data or other analytical approaches like silhouette coefficient determination, while Agglomerative clustering does not require knowledge of the number of clusters. Agglomerative clustering as a hierarchical clustering algorithm starts by treating each data point as a separate cluster and then iteratively merges the most similar clusters. This algorithm can handle noisy data [345]. Thus, it could be effective to be applied to the dataset captured by the sensor during the process to identify abnormality [108], but this method might be computationally expensive, especially for large datasets which are typically captured during the LPBF print. Another alternative method suitable for LPBF noisy data is DBSCAN, although this method is very sensitive to the choice of hyperparameters, and its results vary largely based on the density and distribution of data [365], its application on data of visible-NIR camera could be considered to predict melt pool dimension [125]. Recently, the application of SOM was discussed in LPBF. SOM is a fast and efficient algorithm that can handle high-dimensional data which make it suitable for analyzing photodiode dataset [217]. But, SOMs are sensitive to the initialization of the network and can converge to a suboptimal solution [366]. Another use of unsupervised learning is data reduction which could be useful in reducing the dimensions of the dataset. Data dimension reduction could reduce the computational burden or even something yield better performance for machine learning algorithms when analyzing the dataset is computationally expensive [367]. For example, when many parameters are involved like the LPBF process, PCA or SVD could transform them into a lower-dimensional space while retaining the most important features of the original data which might be useful for detecting spatter or porosity [47]. However, sometimes reducing too much data could result in the opposite situation like what was discussed by Zhang et al. [47].

- Reinforcement learning

Reinforcement learning (RL) algorithms have the potential to be useful in the LPBF process for enhancing the quality and efficiency of the process. Real-time monitoring and adjustments can enable them to detect defects and improve final product quality. LPBF processes can also be optimized by identifying the most efficient laser power, scanning speed, and other parameters to reduce build time and minimize material waste by RL [350]. Furthermore, they are adaptive and flexible, so they can adapt to changes in LPBF processes, such as variations in material properties, to optimize manufacturing. A notable feature of these algorithms is that they optimize a reward function to learn to achieve specific goals, one of which can be improving LPBF quality and efficiency. Moreover, their ability to learn from experience and improve their performance over time makes them useful in situations where it is

difficult to specify an optimal solution [350]. Although the potential of RL algorithms in LPBF is clear according to its feature, the use of RL in this field is not yet widespread. Only two studies have employed RL in LPBF [97,267], one to distinguish between print quality levels (poor, medium, and high) [267], and the other to forecast surface roughness [97]. Several obstacles need to be addressed before RL can be widely adopted in the AM industry. One major issue is that implementing an RL algorithm may add a layer of complexity to a complex LPBF process. Furthermore, RL models could be challenging to train and unstable in complex environments [368]. The lack of interpretability referred to as "black boxes," and high computational costs are other downsides. It can also be difficult to design reward functions that accurately reflect the desired outcomes, which is a challenge in some applications. As mentioned, the use of RL algorithms for in-situ monitoring of the LPBF process is a promising area of research, but further work is required to fully exploit its potential.

5. Future research direction

The review of studies conducted on in-situ sensors and machine learning monitoring techniques has shown that further work on the development of monitoring and control of LPBF must be carried out to enhance the robustness and stability of the process. The following suggestions are recommended for future research directions:

1- More than fifty parameters control the LPBF process. Many authors have shown the effect of process signature on product qualities; however, few studies have been conducted to establish a proper combination of such parameters leads to a high-quality print. In addition, limited studies have shown the effect of part position in the build plate on product quality [369–371]. As a result, further investigation will be needed lead to improve the repeatability of the process.

2- The development of global/adaptable in-situ data analyzing algorithms, which are compatible with a variety of LBPF systems introduced by different OEMs, will have a broad impact on the adoption of LBPF for serial production. In addition, the expansion of materials that will be covered by these algorithms will be a tremendous step toward the wider use of LPBF.

3- There is a need to combine artificial intelligence methods with physics-based models of LPBF. These requirements can be materialized in the form of physics-based constrained machine learning models that involve theoretical modeling of the process along with machine learning algorithms. An example of this is in the generative artificial intelligence models used for topology optimization that allow the generation of several optimized structures within a short amount of time.

4- More advanced and faster sensing devices should be used to obtain high-resolution data. In addition, the calibration of sensors should be addressed to the extensive adoption of in-situ sensors in the academic and industrial domains. For instance, if the sensitive wavelength range of radiative sensors is not similar to the wavelength optimized for the scanner mirror and f-theta lens, the chromatic aberration phenomenon occurs. Additionally, off-axial in-situ sensors gather data from different angles and distances, resulting in geometric distortion. Therefore, there is a huge demand for advanced in-situ sensors and calibration methods that can sample the process at a higher frequency.

5- High-frequency data is repeatedly captured and recorded during the process. Thus, data reduction is demanded to extract relevant features. In the literature, PCA and SVD were used to extract the most significant features of data; however, more advanced methods, such as Spatially Weighted Principal Component Analysis and Neural Auto-encoder could be used to highlight the most significant features.

6- Currently, there is a lack of standards for workflow and best practices for the laser powder bed fusion additive manufacturing process, which researchers could use to validate their machine learning models. This is unlike ImageNet [372], which serves as a standard dataset for computer vision tasks. An established dataset in the LPBF field would help to standardize the industry by providing a common set of data and metrics for evaluating the performance of different machine learning models, and also allow researchers to better understand the capabilities and limitations of various machine learning methods. A positive step is the Additive Manufacturing Metrology Testbed (AMMT) at the National Institute of Standards and Technology (NIST), which offers a process monitoring dataset consisting of in-situ process monitoring data, such as melt-pool and slice layer images, collected using a Mikrontron EOSens 3CL and a Basler acA3800-10 g camera, respectively [118].

7- Further investigations are required to be concentrated on the artificial generation of relative and accurate in-situ data sets relying upon ML models capable of artificial data generation using limited experimental data, such as the variational autoencoder (VAE) algorithm. These techniques could intensively aid the challenge of lack of sufficient data set needed for deep learning application, which leads to reliable modeling of LPBF parameters relations and reaching realistic decision making in terms of the final quality of products. These techniques could also eliminate a major portion of time-consuming experimental and simulation works employed for dataset gathering.

8- Machine learning algorithms could tackle many challenges of process monitoring. ML methods allow for feature extraction and analysis of the extracted dataset in a minimum time. Hence, the algorithms are appropriate for dealing with the LPBF process in real-time. However, most ML algorithms applied on the LPBF are passive supervised learning, which is time-consuming and expensive in terms of costs and human efforts to train/test the experiment and simulate each input set. In this regard, exploring more unsupervised and reinforcement learning methods in the future could be highly beneficial in terms of real-time LPBF process quality control.

9- Aside from unsupervised and reinforcement-based algorithms, the inefficiency in time and expense of conventional supervised learning algorithms could also be addressed by active supervised learning algorithms, which could be one of the most important potential directions of future study. Active learning aims to choose a small dataset when the labeling is difficult, time-consuming, or expensive. Additionally, it can dynamically pose queries during the training process to label new data points [373]. Therefore, expanding the application of active learning in LPBF is recommended.

10- Applying the data analysis methods for real-time defect detection is another fundamental challenge in LPBF. In literature, most of the studies have analyzed offline in-situ data. Currently, the speed of the process limits the online detection of defects. As a result, maintaining the processing speed is a considerable problem, which can mainly be seen in online defect detection and reliable alarm rule processes.

11- Few studies have been published regarding the development of the controller to change the print parameters in real-time. On the other hand, all of them have applied the controller on an in-house developed system that limits the challenge of duplication of their findings for further progress. Although many commercial vendors (EOS, SLM solution, Concept, Renishaw, Trumpf, and B6 Sigma) have introduced their sensing modules and analysis toolboxes to capture and analyze the in-situ data, only the decrypted data are provided/accessible, and the manufacturers protect the raw dataset.

Declaration of competing interest

The authors have no conflict of interest to declare.

Acknowledgment

The authors appreciate the financial support of Natural Sciences and Engineering Research Council of Canada (NSERC) Network for Holistic Innovation in Additive Manufacturing (HI-AM).

References

[1] Toyserkani E, Sarker D, Ibhadode OO, Liravi F, Russo P, Taherkhani K. Metal additive manufacturing. 1st ed. John Wiley; 2021. https://doi.org/10.1002/9781119210801.
[2] Ye D, Hong GS, Zhang Y, Zhu K, Fuh JYH. Defect detection in selective laser melting technology by acoustic signals with deep belief networks. Int J Adv Manuf Technol 2018;96:2791–801. https://doi.org/10.1007/s00170-018-1728-0.
[3] Gibson I, Rosen DW, Stucker B. Additive manufacturing technologies: rapid prototyping to direct digital manufacturing. Springer; 2010. https://doi.org/10.1007/978-1-4419-1120-9.
[4] Osakada K, Shiomi M. Flexible manufacturing of metallic products by selective laser melting of powder. Int J Mach Tool Manuf 2006;46:1188–93. https://doi.org/10.1016/j.ijmachtools.2006.01.024.
[5] Yadroitsev I, Bertrand P, Smurov I. Parametric analysis of the selective laser melting process. Appl Surf Sci 2007;253:8064–9. https://doi.org/10.1016/j.apsusc.2007.02.088.
[6] Kempen K, Thijs L, Yasa E, Badrossamay M, Verheecke W, Kruth JP. Process optimization and microstructural analysis for selective laser melting of AlSi10Mg. In: 22nd Annu. Int. Solid Free. Fabr. Symp. - An Addit. Manuf. Conf. SFF. 2011; 2011. p. 484–95.
[7] Toyserkani E, Khajepour A, Corbin SFSS. Laser cladding. CRC PRESS LLC; 2004. https://doi.org/10.2351/1.521888.
[8] Berumen S, Bechmann F, Lindner S, Kruth JP, Craeghs T. Quality control of laser- and powder bed-based additive manufacturing (AM) technologies. Phys Procedia 2010;5:617–22. https://doi.org/10.1016/j.phpro.2010.08.089.
[9] Gaikwad A, Imani F, Rao P, Yang H, Reutzel E. Design rules and in-situ quality monitoring of thin-wall features made using laser powder bed fusion. In: ASME 2019 14th Int. Manuf. Sci. Eng. Conf. MSEC 2019. 58745; 2019, V001T01A039. https://doi.org/10.1115/MSEC2019-3035.
[10] Kruth J, Mercelis P, Van Vaerenbergh J, Craeghs T. Feedback control of selective laser melting. In: Proc 3rd Int Conf Adv Res Virtual Rapid Prototyp; 2007. p. 521–8.
[11] Gaikwad A, Giera B, Guss GM, Forien JB, Matthews MJ, Rao P. Heterogeneous sensing and scientific machine learning for quality assurance in laser powder bed fusion – a single-track study. Addit Manuf 2020;36:101659. https://doi.org/10.1016/j.addma.2020.101659.
[12] Aminzadeh M, Kurfess T. In-situ monitoring of dimensional accuracy in additive manufacturing by layerwise detection of geometric errors. In: Proc. - ASPE 2015 Spring Top. Meet. Achiev. Precis. Toler. Addit. Manuf; 2015. p. 151–4.
[13] Caltanissetta F, Grasso M, Petrò S, Colosimo BM. Characterization of in-situ measurements based on layerwise imaging in laser powder bed fusion. Addit Manuf 2018;24:183–99. https://doi.org/10.1016/j.addma.2018.09.017.
[14] Gaikwad A, Imani F, Yang H, Reutzel E, Rao P. In situ monitoring of thin-wall build quality in laser powder bed fusion using deep learning. Smart Sustain Manuf Syst 2019;3:98–121. https://doi.org/10.1520/SSMS20190027.
[15] Pagani L, Grasso M, Scott PJ, Colosimo BM. Automated layerwise detection of geometrical distortions in laser powder bed fusion. Addit Manuf 2020;36:101435. https://doi.org/10.1016/j.addma.2020.101435.
[16] Aminzadeh M, Kurfess T. Vision-based inspection system for dimensional accuracy in powder-bed additive manufacturing. In: ASME 2016 11th Int. Manuf. Sci. Eng. Conf. MSEC 2016. 2; 2016, V002T04A042. https://doi.org/10.1115/MSEC2016-8674.
[17] Li Z, Liu X, Wen S, He P, Zhong K, Wei Q, et al. In situ 3D monitoring of geometric signatures in the powder-bed-fusion additive manufacturing process via vision sensing methods. Sensors (Switzerland) 2018;18:1180. https://doi.org/10.3390/s18041180.
[18] Vallabh CKP, Zhao X. Single-camera two-wavelength imaging Pyrometry for melt Pool temperature measurement and monitoring in laser powder bed fusion based additive manufacturing. J Manuf Process 2021;79:486–500.
[19] Mazzoleni L, Demir AG, Caprio L, Pacher M, Previtali B. Real-time observation of melt Pool in selective laser melting: spatial, temporal, and wavelength resolution criteria. IEEE Trans Instrum Meas 2020;69:1179–90. https://doi.org/10.1109/TIM.2019.2912236.
[20] Mazzoleni L, Caprio L, Pacher M, Demir AG, Previtali B. External illumination strategies for melt pool geometry monitoring in SLM. JOM 2019;71:928–37. https://doi.org/10.1007/s11837-018-3209-1.
[21] Ma H, Mao Z, Feng W, Yang Y, Hao C, Zhou J, et al. Online in-situ monitoring of melt pool characteristic based on a single high-speed camera in laser powder bed fusion process. Appl Therm Eng 2022;211:118515. https://doi.org/10.1016/j.applthermaleng.2022.118515.
[22] Hooper PA. Melt pool temperature and cooling rates in laser powder bed fusion. Addit Manuf 2018;22:548–59. https://doi.org/10.1016/j.addma.2018.05.032.
[23] Craeghs T, Clijsters S, Kruth JP, Bechmann F, Ebert MC. Detection of process failures in Layerwise laser melting with optical process monitoring. Phys Procedia 2012;39:753–9. https://doi.org/10.1016/j.phpro.2012.10.097.
[24] Lin X, Wang Q, Fuh JYH, Zhu K. Motion feature based melt pool monitoring for selective laser melting process. J Mater Process Technol 2022;303. https://doi.org/10.1016/j.jmatprotec.2022.117523.
[25] Zhang W, Ma H, Zhang Q, Fan S. Prediction of powder bed thickness by spatter detection from coaxial optical images in selective laser melting of 316L stainless steel. Mater Des 2022;213. https://doi.org/10.1016/j.matdes.2021.110301.
[26] Tan Z, Fang Q, Li H, Liu S, Zhu W, Yang D. Neural network based image segmentation for spatter extraction during laser-based powder bed fusion processing. Opt Laser Technol 2020;130:106347. https://doi.org/10.1016/j.optlastec.2020.106347.
[27] Barrett C, Carradero C, Harris E, Rogers K, MacDonald E, Conner B. Statistical analysis of spatter velocity with high-speed stereovision in laser powder bed fusion. Prog Addit Manuf 2019;4:423–30. https://doi.org/10.1007/s40964-019-00094-6.
[28] Barrett C, Carradero C, Harris E, McKnight J, Walker J, MacDonald E, et al. Low cost, high speed stereovision for spatter tracking in laser powder bed fusion. In: Solid Free. Fabr. 2018 Proc. 29th Annu. Int. Solid Free. Fabr. Symp. - An Addit. Manuf. Conf. SFF 2018; 2020. p. 2122–34.
[29] Nassar AR, Gundermann MA, Reutzel EW, Guerrier P, Krane MH, Weldon MJ. Formation processes for large ejecta and interactions with melt pool formation in powder bed fusion additive manufacturing. Sci Rep 2019;9:1–11. https://doi.org/10.1038/s41598-019-41415-7.
[30] Bidare P, Bitharas I, Ward RM, Attallah MM, Moore AJ. Fluid and particle dynamics in laser powder bed fusion. Acta Mater 2018;142:107–20. https://doi.org/10.1016/j.actamat.2017.09.051.
[31] Bidare P, Bitharas I, Ward RM, Attallah MM, Moore AJ. Laser powder bed fusion in high-pressure atmospheres. Int J Adv Manuf Technol 2018;99:543–55. https://doi.org/10.1007/s00170-018-2495-7.
[32] Ye D, Hsi Fuh JY, Zhang Y, Hong GS, Zhu K. In situ monitoring of selective laser melting using plume and spatter signatures by deep belief networks. ISA Trans 2018;81:96–104. https://doi.org/10.1016/j.isatra.2018.07.021.
[33] Taheri Andani M, Dehghani R, Karamooz-Ravari MR, Mirzaeifar R, Ni J. A study on the effect of energy input on spatter particles creation during selective laser melting process. Addit Manuf 2018;20:33–43. https://doi.org/10.1016/j.addma.2017.12.009.
[34] Liu Y, Yang Y, Mai S, Wang D, Song C. Investigation into spatter behavior during selective laser melting of AISI 316L stainless steel powder. Mater Des 2015;87:797–806. https://doi.org/10.1016/j.matdes.2015.08.086.
[35] Eschner E, Staudt T, Schmidt M. 3D particle tracking velocimetry for the determination of temporally resolved particle trajectories within laser powder bed fusion of metals. Int J Extrem Manuf 2019;1:035002. https://doi.org/10.1088/2631-7990/ab3de9.
[36] Schwerz C, Raza A, Lei X, Nyborg L, Hryha E, Wirdelius H. In-situ detection of redeposited spatter and its influence on the formation of internal flaws in laser powder bed fusion. Addit Manuf 2021;47:102370. https://doi.org/10.1016/j.addma.2021.102370.
[37] Eschner E, Staudt T, Schmidt M. Correlation of spatter behavior and process zone formation in powder bed fusion of metals. CIRP Ann 2020;69:209–12. https://doi.org/10.1016/j.cirp.2020.04.092.
[38] Yang D, Li H, Liu S, Song C, Yang Y, Shen S, et al. In situ capture of spatter signature of SLM process using maximum entropy double threshold image processing method based on genetic algorithm. Opt Laser Technol 2020;131:106371. https://doi.org/10.1016/j.optlastec.2020.106371.
[39] Yang L, Lo L, Ding S, Özel T. Monitoring and detection of meltpool and spatter regions in laser powder bed fusion of super alloy Inconel 625. Prog Addit Manuf 2020;5:367–78. https://doi.org/10.1007/s40964-020-00140-8.
[40] Repossini G, Laguzza V, Grasso M, Colosimo BM. On the use of spatter signature for in-situ monitoring of laser powder bed fusion. Addit Manuf 2017;16:35–48. https://doi.org/10.1016/j.addma.2017.05.004.
[41] Zhang Y, Fuh JYH, Ye D, Hong GS. In-situ monitoring of laser-based PBF via off-axis vision and image processing approaches. Addit Manuf 2019;25:263–74. https://doi.org/10.1016/j.addma.2018.10.020.
[42] Ly S, Rubenchik AM, Khairallah SA, Guss G, Matthews MJ. Metal vapor micro-jet controls material redistribution in laser powder bed fusion additive manufacturing. Sci Rep 2017;7:1–12. https://doi.org/10.1038/s41598-017-04237-z.
[43] Scime L, Beuth J. Using machine learning to identify in-situ melt pool signatures indicative of flaw formation in a laser powder bed fusion additive manufacturing process. Addit Manuf 2019;25:151–65. https://doi.org/10.1016/j.addma.2018.11.010.
[44] Scime L, Beuth J. Anomaly detection and classification in a laser powder bed additive manufacturing process using a trained computer vision algorithm. Addit Manuf 2018;19:114–26. https://doi.org/10.1016/j.addma.2017.11.009.
[45] Yin J, Wang D, Yang L, Wei H, Dong P, Ke L, et al. Correlation between forming quality and spatter dynamics in laser powder bed fusion. Addit Manuf 2020;31:100958. https://doi.org/10.1016/j.addma.2019.100958.
[46] Yin J, Yang LL, Yang X, Zhu H, Wang D, Ke L, et al. High-power laser-matter interaction during laser powder bed fusion. Addit Manuf 2019;29:100778. https://doi.org/10.1016/j.addma.2019.100778.

[47] Zhang Y, Hong GS, Ye D, Zhu K, Fuh JYH. Extraction and evaluation of melt pool, plume and spatter information for powder-bed fusion AM process monitoring. Mater Des 2018;156:458–69. https://doi.org/10.1016/j.matdes.2018.07.002.
[48] Prasad Vallabh CK, Xiong Y, Zhao X. In-situ monitoring of laser powder bed fusion process anomalies via a comprehensive analysis of off-axis camera data. In: ASME 2020 15th Int. Manuf. Sci. Eng. Conf. MSEC 2020. 1. American Society of Mechanical Engineers; 2020. https://doi.org/10.1115/MSEC2020-8300.
[49] Zheng H, Li H, Lang L, Gong S, Ge Y. Effects of scan speed on vapor plume behavior and spatter generation in laser powder bed fusion additive manufacturing. J Manuf Process 2018;36:60–7. https://doi.org/10.1016/j.jmapro.2018.09.011.
[50] Islam M, Purtonen T, Piili H, Salminen A, Nyrhilä O. Temperature profile and imaging analysis of laser additive manufacturing of stainless steel. Phys Procedia 2013;41:835–42. https://doi.org/10.1016/j.phpro.2013.03.156.
[51] Zhang Y, Soon HG, Ye D, Fuh JYH, Zhu K. Powder-bed fusion process monitoring by machine vision with hybrid convolutional neural networks. IEEE Trans Industr Inform 2020;16:5769–79. https://doi.org/10.1109/TII.2019.2956078.
[52] Clijsters S, Craeghs T, Buls S, Kempen K, Kruth JP. In situ quality control of the selective laser melting process using a high-speed, real-time melt pool monitoring system. Int J Adv Manuf Technol 2014;75:1089–101. https://doi.org/10.1007/s00170-014-6214-8.
[53] Craeghs T, Bechmann F, Berumen S, Kruth JP. Feedback control of layerwise laser melting using optical sensors. Phys Procedia 2010;5:505–14. https://doi.org/10.1016/j.phpro.2010.08.078.
[54] Gobert C, Reutzel EW, Petrich J, Nassar AR, Phoha S. Application of supervised machine learning for defect detection during metallic powder bed fusion additive manufacturing using high resolution imaging. Addit Manuf 2018;21:517–28. https://doi.org/10.1016/j.addma.2018.04.005.
[55] Petrich J, Gobert C, Phoha S, Nassar AR, Reutzel EW. Machine learning for defect detection for PBFAm using high resolution layerwise imaging coupled with post-build CT scans. In: Solid Free. Fabr. 2017 Proc. 28th Annu. Int. Solid Free. Fabr. Symp. - An Addit. Manuf. Conf. SFF 2017. Solid freeform fabrication 2017: Proceedings of the 28th annual international solid freeform fabrication symposium - an additive manufacturing conference, SFF 2017; 2017. p. 1363–81.
[56] Lu Y, Wang Y. Physics based compressive sensing to monitor temperature and melt flow in laser powder bed fusion. Addit Manuf 2021;47:102304. https://doi.org/10.1016/j.addma.2021.102304.
[57] Grasso M, Laguzza V, Semeraro Q, Colosimo BM. In-process monitoring of selective laser melting: spatial detection of defects via image data analysis. J Manuf Sci Eng Trans ASME 2017;139:1–16. https://doi.org/10.1115/1.4034715.
[58] Van Gestel C. Study of physical phenomena of selective laser melting towards increased productivity. Thesis EPFL 2015:117. https://doi.org/10.1016/0168-9002(90)90810-S.
[59] Colosimo BM, Grasso M. Spatially weighted PCA for monitoring video image data with application to additive manufacturing. J Qual Technol 2018;50:391–417. https://doi.org/10.1080/00224065.2018.1507563.
[60] Angelone R, Caggiano A, Teti R, Spierings A, Staub A, Wegener K. Bio-intelligent selective laser melting system based on convolutional neural networks for in-process fault identification. Procedia CIRP 2020;88:612–7. https://doi.org/10.1016/j.procir.2020.05.107.
[61] Li J, Cao L, Xu J, Wang S, Zhou Q. In situ porosity intelligent classification of selective laser melting based on coaxial monitoring and image processing. Meas J Int Meas Confed 2022;187:110232. https://doi.org/10.1016/j.measurement.2021.110232.
[62] Ulbricht A, Mohr G, Altenburg SJ, Oster S, Maierhofer C, Bruno G. Can potential defects in lpbf be healed from the laser exposure of subsequent layers? A quantitative study. Metals (Basel) 2021;11:1012. https://doi.org/10.3390/met11071012.
[63] Zur Jacobsmuhlen J, Kleszczynski S, Schneider D, Witt G. High resolution imaging for inspection of Laser Beam Melting systems. In: 2013 IEEE Int. Instrum. Meas. Technol. Conf. IEEE; 2013. p. 707–12. https://doi.org/10.1109/I2MTC.2013.6555507.
[64] Aminzadeh M, Kurfess TR. Online quality inspection using Bayesian classification in powder-bed additive manufacturing from high-resolution visual camera images. J Intell Manuf 2019;30:2505–23. https://doi.org/10.1007/s10845-018-1412-0.
[65] Caggiano A, Zhang J, Alfieri V, Caiazzo F, Gao R, Teti R. Machine learning-based image processing for on-line defect recognition in additive manufacturing. CIRP Ann 2019;68:451–4. https://doi.org/10.1016/j.cirp.2019.03.021.
[66] Snow Z, Diehl B, Reutzel EW, Nassar A. Toward in-situ flaw detection in laser powder bed fusion additive manufacturing through layerwise imagery and machine learning. J Manuf Syst 2021;59:12–26. https://doi.org/10.1016/j.jmsy.2021.01.008.
[67] Caprio L, Demir AG, Previtali B. Observing molten pool surface oscillations during keyhole processing in laser powder bed fusion as a novel method to estimate the penetration depth. Addit Manuf 2020;36:101470. https://doi.org/10.1016/j.addma.2020.101470.
[68] Aminzadeh M, Kurfess T. In-situ quality inspection of laser powder-bed fusion using high-resolution visual camera images. In: Solid Free. Fabr. 2016 Proc. 27th Annu. Int. Solid Free. Fabr. Symp. - An Addit. Manuf. Conf. SFF 2016, The University of Texas at Austin; 2016. p. 1412–27.
[69] Bartlett JL, Jarama A, Jones J, Li X. Prediction of microstructural defects in additive manufacturing from powder bed quality using digital image correlation. Mater Sci Eng A 2020;794:140002. https://doi.org/10.1016/j.msea.2020.140002.
[70] Scime L, Siddel D, Baird S, Paquit V. Layer-wise anomaly detection and classification for powder bed additive manufacturing processes: a machine-agnostic algorithm for real-time pixel-wise semantic segmentation. Addit Manuf 2020;36:101453. https://doi.org/10.1016/j.addma.2020.101453.
[71] Williams RJ, Piglione A, Rønneberg T, Jones C, Pham MS, Davies CM, et al. In situ thermography for laser powder bed fusion: effects of layer temperature on porosity, microstructure and mechanical properties. Addit Manuf 2019;30. https://doi.org/10.1016/j.addma.2019.100880.
[72] Colosimo BM, Grossi E, Caltanissetta F, Grasso M. Penelope: a novel prototype for in situ defect removal in LPBF. JOM 2020;72:1332–9. https://doi.org/10.1007/s11837-019-03964-0.
[73] Lu QY, Nguyen NV, Hum AJW, Tran T, Wong CH. Identification and evaluation of defects in selective laser melted 316L stainless steel parts via in-situ monitoring and micro computed tomography. Addit Manuf 2020;35:101287. https://doi.org/10.1016/j.addma.2020.101287.
[74] Lu QY, Nguyen NV, Hum AJW, Tran T, Wong CH. Optical in-situ monitoring and correlation of density and mechanical properties of stainless steel parts produced by selective laser melting process based on varied energy density. J Mater Process Technol 2019;271:520–31. https://doi.org/10.1016/j.jmatprotec.2019.04.026.
[75] Bruna-Rosso C, Demir AG, Previtali B. Selective laser melting finite element modeling: validation with high-speed imaging and lack of fusion defects prediction. Mater Des 2018;156:143–53. https://doi.org/10.1016/j.matdes.2018.06.037.
[76] Bamberg J, Zenzinger G, Ladewig A. In-process control of selective laser melting by quantitative optical tomography. Palaios 2007;22:143–54.
[77] Zenzinger G, Bamberg J, Ladewig A, Hess T, Henkel B, Satzger W. Process monitoring of additive manufacturing by using optical tomography. AIP Conf Proc 2015;1650(1):164–70. https://doi.org/10.1063/1.4914606.
[78] Feng S, Chen Z, Bircher B, Ji Z, Nyborg L, Bigot S. Predicting laser powder bed fusion defects through in-process monitoring data and machine learning. Mater Des 2022;222:111115. https://doi.org/10.1016/J.MATDES.2022.111115.
[79] Gaikwad A, Williams RJ, de Winton H, Bevans BD, Smoqi Z, Rao P, et al. Multi phenomena melt pool sensor data fusion for enhanced process monitoring of laser powder bed fusion additive manufacturing. Mater Des 2022;221:110919. https://doi.org/10.1016/J.MATDES.2022.110919.
[80] Williams RJ, de Winton H, Fernandez V, Hooper PA. Localised porosity detection in laser powder bed fusion using in-situ monitoring. SSRN Electron J 2022. https://doi.org/10.2139/ssrn.4255024.
[81] Donadello S, Motta M, Demir AG, Previtali B. Monitoring of laser metal deposition height by means of coaxial laser triangulation. Opt Lasers Eng 2019;112:136–44. https://doi.org/10.1016/j.optlaseng.2018.09.012.
[82] Yadav P, Rigo O, Arvieu C, Le Guen E, Lacoste E. Data treatment of in situ monitoring systems in selective laser melting machines. Adv Eng Mater 2021;23:1–15. https://doi.org/10.1002/adem.202001327.
[83] Abdelrahman M, Reutzel EW, Nassar AR, Starr TL. Flaw detection in powder bed fusion using optical imaging. Addit Manuf 2017;15:1–11. https://doi.org/10.1016/j.addma.2017.02.001.
[84] Imani F, Gaikwad A, Montazeri M, Rao P, Yang H, Reutzel E. Layerwise in-process quality monitoring in laser powder bed fusion. In: ASME 2018 13th Int. Manuf. Sci. Eng. Conf. MSEC 2018. 51357; 2018, V001T01A038. https://doi.org/10.1115/MSEC2018-6477.
[85] Dinh DM, Muller N, Quinsat Y. Layering defects detection in laser powder bed fusion using embedded vision system. Comput Aided Des Appl 2021;18:1111–8. https://doi.org/10.14733/cadaps.2021.1111-1118.
[86] Mohr G, Altenburg SJ, Ulbricht A, Heinrich P, Baum D, Maierhofer C, et al. In-situ defect detection in laser powder bed fusion by using thermography and optical tomography—comparison to computed tomography. Metals (Basel) 2020;10:103. https://doi.org/10.3390/met10010103.
[87] Forien JB, Calta NP, DePond PJ, Guss GM, Roehling TT, Matthews MJ. Detecting keyhole pore defects and monitoring process signatures during laser powder bed fusion: a correlation between in situ pyrometry and ex situ X-ray radiography. Addit Manuf 2020;35:101336. https://doi.org/10.1016/j.addma.2020.101336.
[88] Kim FH, Yeung H, Garboczi EJ. Characterizing the effects of laser control in laser powder bed fusion on near-surface pore formation via combined analysis of in-situ melt pool monitoring and X-ray computed tomography. Addit Manuf 2021;48:102372. https://doi.org/10.1016/j.addma.2021.102372.
[89] Furumoto T, Alkahari MR, Ueda T, Aziz MSA, Hosokawa A. Monitoring of laser consolidation process of metal powder with high speed video camera. Phys Procedia 2012;39:706–66. https://doi.org/10.1016/j.phpro.2012.10.098.
[90] Furumoto T, Ueda T, Alkahari MR, Hosokawa A. Investigation of laser consolidation process for metal powder by two-color pyrometer and high-speed video camera. CIRP Ann - Manuf Technol 2013;62:223–6. https://doi.org/10.1016/j.cirp.2013.03.032.
[91] Williams RJ, Piglione A, Rønneberg T, Jones C, Pham MS, Davies CM, et al. In situ thermography for laser powder bed fusion: effects of layer temperature on porosity, microstructure and mechanical properties. Addit Manuf 2019;30:100880. https://doi.org/10.1016/J.ADDMA.2019.100880.
[92] Lane B, Yeung H. Process monitoring dataset from the additive manufacturing metrology testbed (AMMT): overhang part X4. J Res Natl Inst Stand Technol 2021;125:1–18. https://doi.org/10.6028/jres.125.027.
[93] Kleszczynski S, Zur Jacobsmühlen J, Sehrt JT, Witt G. Error detection in laser beam melting systems by high resolution imaging. Int Solid Free Fabr Symp SFF 2012;2012:975–87.
[94] zur Jacobsmühlen J, Kleszczynski S, Witt G, Merhof D. Elevated region area measurement for quantitative analysis of laser beam melting process stability. In:

26th Int. Solid Free. Fabr. Symp. Austin, TX. 26th International Solid Freeform Fabrication Symposium; Austin, TX; 2015. p. 6.
[95] Lane B, Whitenton E, Moylan S. Multiple sensor detection of process phenomena in laser powder bed fusion. In: Thermosense Therm. Infrared Appl. XXXVIII. 9861. SPIE; 2016. p. 20–8. https://doi.org/10.1117/12.2224390.
[96] Yeung H, Lane B, Fox J. Part geometry and conduction-based laser power control for powder bed fusion additive manufacturing. Addit Manuf 2019;30:100844. https://doi.org/10.1016/j.addma.2019.100844.
[97] Knaak C, Masseling L, Duong E, Abels P, Gillner A. Improving build quality in laser powder bed fusion using high dynamic range imaging and model-based reinforcement learning. IEEE Access 2021;9:55214–31. https://doi.org/10.1109/ACCESS.2021.3067302.
[98] Niklas G, Hoff C, Hermsdorf J, Kaierle S, Overmeyer L. Hyperspectral imaging for prediction of surface roughness in laserpowder bed fusion. Int J Adv Manuf Technol 2021;115:1249–58. https://doi.org/10.1007/s00170-021-07274-1.
[99] Yang Z, Lu Y, Yeung H, Krishnamurty S. Investigation of deep learning for real-time melt pool classification in additive manufacturing. In: IEEE Int. Conf. Autom. Sci. Eng; 2019. p. 640–7. https://doi.org/10.1109/COASE.2019.8843291.
[100] Xing W, Chu X, Lyu T, Lee CG, Zou Y, Rong Y. Using convolutional neural networks to classify melt pools in a pulsed selective laser melting process. J Manuf Process 2022;74:486–99. https://doi.org/10.1016/J.JMAPRO.2021.12.030.
[101] Pacher M, Mazzoleni L, Caprio L, Demir AG, Previtali B. Estimation of melt pool size by complementary use of external illumination and process emission in coaxial monitoring of selective laser melting. J Laser Appl 2019;31:022305. https://doi.org/10.2351/1.5096117.
[102] Fox JC, Lane BM, Yeung H. Measurement of process dynamics through coaxially aligned high speed near-infrared imaging in laser powder bed fusion additive manufacturing. Thermosense Therm. Infrared Appl. XXXIX, vol. 10214, SPIE; 2017, p. 34–50. doi:https://doi.org/10.1117/12.2263863.
[103] Cheng B, Lydon J, Cooper K, Cole V, Northrop P, Chou K. Infrared thermal imaging for melt pool analysis in SLM: a feasibility investigation. Virtual Phys Prototyp 2018;13:8–13. https://doi.org/10.1080/17452759.2017.1392685.
[104] Ma P, He X, Wang A. Design of online measurement system for molten pool morphology in selective laser melting (SLM) process. Proc. - 2021 3rd Int. Conf. Artif. Intell. Adv. Manuf. AIAM 2021, 2021. doi:https://doi.org/10.1109/AIAM54119.2021.00049.
[105] Vasileska E, Demir AG, Colosimo BM, Previtali B. Layer-wise control of selective laser melting by means of inline melt pool area measurements. J Laser Appl 2020;32:022057. https://doi.org/10.2351/7.0000108.
[106] Lane B, Grantham S, Yeung H, Zarobila C, Fox J. Performance characterization of process monitoring sensors on the NIST additive manufacturing metrology testbed. In: Solid Free. Fabr. 2017 Proc. 28th Annu. Int. Solid Free. Fabr. Symp. - An Addit. Manuf. Conf. SFF 2017, The University of Texas at Austin; 2020. p. 1279–88.
[107] Kwon O, Kim HG, Ham MJ, Kim W, Kim GH, Cho JH, et al. A deep neural network for classification of melt-pool images in metal additive manufacturing. J Intell Manuf 2020;31:375–86. https://doi.org/10.1007/s10845-018-1451-6.
[108] Fathizadan S, Ju F, Lu Y. Deep representation learning for process variation management in laser powder bed fusion. Addit Manuf 2021;42:101961. https://doi.org/10.1016/j.addma.2021.101961.
[109] Mahmoudi M, Ezzat AA, Elwany A. Layerwise anomaly detection in laser powder-bed fusion metal additive manufacturing. J Manuf Sci Eng Trans ASME 2019;141:031002. https://doi.org/10.1115/1.4042108.
[110] Scime L, Beuth J. A multi-scale convolutional neural network for autonomous anomaly detection and classification in a laser powder bed fusion additive manufacturing process. Addit Manuf 2018;24:273–86. https://doi.org/10.1016/j.addma.2018.09.034.
[111] Yuan B, Guss GM, Wilson AC, Hau-Riege SP, DePond PJ, McMains S, et al. Machine-learning-based monitoring of laser powder bed fusion. Adv Mater Technol 2018;3:1800136. https://doi.org/10.1002/admt.201800136.
[112] Yuan B, Giera B, Guss G, Matthews M, McMains S. Semi-supervised convolutional neural networks for in-situ video monitoring of selective laser melting. In: Proc. - 2019 IEEE Winter Conf. Appl. Comput. Vision, WACV 2019; 2019. p. 744–53. https://doi.org/10.1109/WACV.2019.00084.
[113] Scipioni Bertoli U, Guss G, Wu S, Matthews MJ, Schoenung JM. In-situ characterization of laser-powder interaction and cooling rates through high-speed imaging of powder bed fusion additive manufacturing. Mater Des 2017;135:385–96. https://doi.org/10.1016/j.matdes.2017.09.044.
[114] Yeung H, Lane B. A residual heat compensation based scan strategy for powder bed fusion additive manufacturing. Manuf Lett 2020;25:56–9. https://doi.org/10.1016/j.mfglet.2020.07.005.
[115] Rombouts M, Kruth JP, Froyen L, Mercelis P. Fundamentals of selective laser melting of alloyed steel powders. CIRP Ann - Manuf Technol 2006;55:187–92. https://doi.org/10.1016/S0007-8506(07)60395-3.
[116] Craeghs T, Kruth J-P. Online monitoring and quality control of selective laser melting using optical sensors. In: Proc. 4th Int. Conf. Opt. Meas. Tech. Struct. Syst; 2009. p. 131–40.
[117] Gökhan Demir A, De Giorgi C, Previtali B. Design and implementation of a multisensor coaxial monitoring system with correction strategies for selective laser melting of a maraging steel. J Manuf Sci Eng Trans ASME 2018;140:041003. https://doi.org/10.1115/1.4038568.
[118] Lane B, Yeung H. Process monitoring dataset from the additive manufacturing metrology testbed (AMMT): "Three-dimensional scan strategies". J Res Natl Inst Stand Technol 2019;124:1. https://doi.org/10.6028/jres.124.033.
[119] Lane B, Mekhontsev S, Grantham S, Vlasea ML, Whiting J, Yeung H, et al. Design, developments, and results from the NIST additive manufacturing metrology testbed (AMMT). In: Solid Free. Fabr. 2016 Proc. 27th Annu. Int. Solid Free. Fabr. Symp. - An Addit. Manuf. Conf. SFF 2016; 2016. p. 1145–60.
[120] Taheri Andani M, Dehghani R, Karamooz-Ravari MR, Mirzaeifar R, Ni J. Spatter formation in selective laser melting process using multi-laser technology. Mater Des 2017;131:460–9. https://doi.org/10.1016/j.matdes.2017.06.040.
[121] Yang Z, Lu Y, Yeung H, Krishnamurty S. From scan strategy to melt pool prediction: a neighboring-effect modeling method. J Comput Inf Sci Eng 2020;20:051001. https://doi.org/10.1115/1.4046335.
[122] Milaat FA, Yang Z, Ko H, Jones AT. Prediction of melt pool geometry using deep neural networks. In: Proc. ASME Des. Eng. Tech. Conf. 85376; 2021, V002T02A037. https://doi.org/10.1115/DETC2021-69259.
[123] Foster B, Reutzel E, Nassar A, Hall BT, Brown S, Dickman C. Optical, layerwise monitoring of powder bed fusion. In: Solid Free. Fabr. Symp. Proc. 26th annual international solid freeform fabrication symposium; 2015. p. 295–307. p. 13.
[124] Yan H, Grasso M, Paynabar K, Colosimo BM. Real-time detection of clustered events in video-imaging data with applications to additive manufacturing. IISE Trans 2022;54:464–80. https://doi.org/10.1080/24725854.2021.1882013.
[125] Vasileska E, Demir AG, Colosimo BM, Previtali B. A novel paradigm for feedback control in LPBF: layer-wise correction for overhang structures. Adv Manuf 2022;10. https://doi.org/10.1007/s40436-021-00379-6.
[126] Raplee J, Gockel J, List F, Carver K, Foster S, McFalls T, et al. Towards process consistency and in-situ evaluation of porosity during laser powder bed additive manufacturing. Science and Technology of Welding and Joining 2020;25:679–89. https://doi.org/10.1080/13621718.2020.1823654.
[127] Foster SJ, Carver K, Dinwiddie RB, List F, Unocic KA, Chaudhary A, et al. Process-defect-structure-property correlations during laser powder bed fusion of alloy 718: role of in situ and ex situ characterizations. Metall Mater Trans A Phys Metall Mater Sci 2018;49:5775–98. https://doi.org/10.1007/s11661-018-4870-2.
[128] McNeil JL, Sisco K, Frederick C, Massey M, Carver K, List F, et al. In-situ monitoring for defect identification in nickel alloy complex geometries fabricated by L-PBF additive manufacturing. Metall Mater Trans A Phys Metall Mater Sci 2020;51:6528–45. https://doi.org/10.1007/s11661-020-06036-0.
[129] Wakai Y, Ogura T, Nakano S, Sato N, Kajino S, Suzuki S. Melting behavior in laser powder bed fusion revealed by in situ X-ray and thermal imaging. Int J Adv Manuf Technol 2020;110:1047–59. https://doi.org/10.1007/s00170-020-05828-3.
[130] Heigel JC, Lane BM, Levine LE. In situ measurements of melt-pool length and cooling rate during 3D builds of the metal AM-bench artifacts. Integr Mater Manuf Innov 2020;9:31–53. https://doi.org/10.1007/s40192-020-00170-8.
[131] Baumgartl H, Tomas J, Buettner R, Merkel M. A deep learning-based model for defect detection in laser-powder bed fusion using in-situ thermographic monitoring. Prog Addit Manuf 2020;5:277–85. https://doi.org/10.1007/s40964-019-00108-3.
[132] Yakout M, Phillips I, Elbestawi MA, Fang Q. In-situ monitoring and detection of spatter agglomeration and delamination during laser-based powder bed fusion of invar 36. Opt Laser Technol 2021;136:106741. https://doi.org/10.1016/j.optlastec.2020.106741.
[133] Mohr G, Nowakowski S, Altenburg SJ, Maierhofer C, Hilgenberg K. Experimental determination of the emissivity of powder layers and bulk material in laser powder bed fusion using infrared thermography and thermocouples. Metals (Basel) 2020;10:1–36. https://doi.org/10.3390/met10111546.
[134] Bayle F, Doubenskaia M. Selective laser melting process monitoring with high speed infra-red camera and pyrometer. Fundam Laser Assist Micro-and Nanotechnol 2008;6985:39–46. https://doi.org/10.1117/12.786940.
[135] Reza Yavari M, Williams RJ, Cole KD, Hooper PA, Rao P. Thermal modeling in metal additive manufacturing using graph theory: experimental validation with laser powder bed fusion using in situ infrared thermography data. J Manuf Sci Eng Trans ASME 2020;142:121005. https://doi.org/10.1115/1.4047619.
[136] Plotnikov Y, Henkel D, Burdick J, French A, Sions J, Bourne K. Infrared-assisted acoustic emission process monitoring for additive manufacturing. In: AIP Conf. Proc. 2102; 2019, 020006. https://doi.org/10.1063/1.5099710.
[137] Lane B, Moylan S, Whitenton EP, Ma L. Thermographic measurements of the commercial laser powder bed fusion process at NIST. Rapid Prototyp J 2016;22:778–87. https://doi.org/10.1108/RPJ-11-2015-0161.
[138] Mohr G, Scheuschner N, Hilgenberg K. In situ heat accumulation by geometrical features obstructing heat flux and by reduced inter layer times in laser powder bed fusion of AISI 316L stainless steel. In: Procedia CIRP. 94. Elsevier B.V; 2020. p. 155–60. https://doi.org/10.1016/j.procir.2020.09.030.
[139] Doubenskaia MA, Smurov IY, Teleshevskiy VI, Bertrand P, Zhirnov IV. Determination of true temperature in selective laser melting of metal powder using infrared camera. Mater Sci Forum 2015;834:93–102. https://doi.org/10.4028/www.scientific.net/msf.834.93.
[140] Elwarfalli H, Papazoglou D, Erdahl D, Doll A, Speltz J. In situ process monitoring for laser-powder bed fusion using convolutional neural networks and infrared tomography. In: Proc. IEEE Natl. Aerosp. Electron. Conf. NAECON, vol. 2019-July. Institute of Electrical and Electronics Engineers Inc; 2019. p. 323–7. https://doi.org/10.1109/NAECON46414.2019.9058251.
[141] Mohr G, Altenburg SJ, Hilgenberg K. Effects of inter layer time and build height on resulting properties of 316L stainless steel processed by laser powder bed fusion. Addit Manuf 2020;32:101080. https://doi.org/10.1016/j.addma.2020.101080.
[142] Alldredge J, Slotwinski J, Storck S, Kim S, Goldberg A, Montalbano T. In-situ monitoring and modeling of metal additive manufacturing powder bed fusion. In: AIP Conf. Proc. 1949; 2018, 020007. https://doi.org/10.1063/1.5031504.

[143] Kolb T, Elahi R, Seeger J, Soris M, Scheitler C, Hentschel O, et al. Camera signal dependencies within coaxial melt pool monitoring in laser powder bed fusion. Rapid Prototyp J 2020;26:100–6. https://doi.org/10.1108/RPJ-01-2019-0022.
[144] Schilp J, Seidel C, Krauss H, Weirather J. Investigations on temperature fields during laser beam melting by means of process monitoring and multiscale process modelling. Adv Mech Eng 2014;6:217584. https://doi.org/10.1155/2014/217584.
[145] Heigel JC, Lane B, Levine L, Phan T, Whiting J. In situ thermography of the metal bridge structures fabricated for the 2018 additive manufacturing benchmark test series (AM-Bench 2018). J Res Natl Inst Stand Technol 2020;125. https://doi.org/10.6028/JRES.125.005.
[146] Estalaki SM, Lough CS, Landers RG, Kinzel EC, Luo T. Predicting defects in laser powder bed fusion using in-situ thermal imaging data and machine learning. Addit Manuf 2022;58:103008. https://doi.org/10.1016/j.addma.2022.103008.
[147] Moylan S, Whitenton E, Lane B, Slotwinski J. Infrared thermography for laser-based powder bed fusion additive manufacturing processes. AIP Conf Proc 2014;1581:1191–6. https://doi.org/10.1063/1.4864956.
[148] Krauss H, Zeugner T, Zaeh MF. Layerwise monitoring of the selective laser melting process by thermography. Phys Procedia 2014;56:64–71. https://doi.org/10.1016/j.phpro.2014.08.097.
[149] Lough CS, Wang X, Smith CC, Landers RG, Bristow DA, Drallmeier JA, et al. Correlation of SWIR imaging with LPBF 304L stainless steel part properties. Addit Manuf 2020;35:101359. https://doi.org/10.1016/j.addma.2020.101359.
[150] Lough CS, Wang X, Landers RG, Bristow DA, Drallmeier JA, Kinzel EC. In-situ local part qualification of slm 304l stainless steel through voxel based processing of SWIR imaging data. In: Solid Free. Fabr. 2019 Proc. 30th Annu. Int. Solid Free. Fabr. Symp. - An Addit. Manuf. Conf. SFF 2019; 2019. p. 1611–25.
[151] Dunbar AJ, Nassar AR. Assessment of optical emission analysis for in-process monitoring of powder bed fusion additive manufacturing. Virtual Phys Prototyp 2018;13:14–9. https://doi.org/10.1080/17452759.2017.1392683.
[152] Molnar B, Heigel JC, Whitenton E. In situ thermography during laser powder bed fusion of a nickel superalloy 625 artifact with various overhangs and supports. J Res Natl Inst Stand Technol 2020;126:1–12. https://doi.org/10.6028/JRES.126.005.
[153] Ansari MJ, Nguyen DS, Park HS. Investigation of SLM process in terms of temperature distribution and melting pool size: modeling and experimental approaches. Materials (Basel) 2019;12:1272. https://doi.org/10.3390/ma12081272.
[154] Jalalahmadi B, Liu J, Rios J, Slotwinski J, Peitsch C, Goldberg A, et al. In-process defect monitoring and correction in additive manufacturing of aluminum alloys. In: Vert. Flight Soc. - Forum 75 Futur. Vert. Flight - Proc. 75th Annu. Forum Technol. Disp; 2019. p. 14.
[155] Grasso M, Demir AG, Previtali B, Colosimo BM. In situ monitoring of selective laser melting of zinc powder via infrared imaging of the process plume. Robot Comput Integr Manuf 2018;49:229–39. https://doi.org/10.1016/j.rcim.2017.07.001.
[156] Thombansen U, Gatej A, Pereira M. Process observation in fiber laser–based selective laser melting. Optim Eng 2014;54:011008. https://doi.org/10.1117/1.oe.54.1.011008.
[157] Liu T, Lough CS, Sehhat H, Ren YM, Christofides PD, Kinzel EC, et al. In-situ infrared thermographic inspection for local powder layer thickness measurement in laser powder bed fusion. Addit Manuf 2022;55:102873. https://doi.org/10.1016/J.ADDMA.2022.102873.
[158] Krauss H, Eschey C, Zaeh MF. Thermography for monitoring the selective laser melting process. In: 23rd Annu. Int. Solid Free. Fabr. Symp. - An Addit. Manuf. Conf. SFF 2012; 2012. p. 999–1014.
[159] Lane B, Whitenton EP. Calibration and measurement procedures for a high magnification thermal camera. Natl Inst Stand Technol 2015. https://doi.org/10.6028/NIST.IR.8098.
[160] Özel T, Shaurya A, Altay A, Yang L. Process monitoring of meltpool and spatter for temporal-spatial modeling of laser powder bed fusion process. Procedia CIRP 2018;74:102–6. https://doi.org/10.1016/j.procir.2018.08.049.
[161] Oster S, Fritsch T, Ulbricht A, Mohr G, Bruno G, Maierhofer C, et al. On the registration of thermographic in situ monitoring data and computed tomography reference data in the scope of defect prediction in laser powder bed fusion. Metals (Basel) 2022;12:947. https://doi.org/10.3390/met12060947.
[162] Lough CS, Liu T, Wang X, Brown B, Landers RG, Bristow DA, et al. Local prediction of laser powder bed fusion porosity by short-wave infrared imaging thermal feature porosity probability maps. J Mater Process Technol 2022;302:117473. https://doi.org/10.1016/j.jmatprotec.2021.117473.
[163] Zhang H, Vallabh CKP, Zhao X. Registration and fusion of large-scale melt pool temperature and morphology monitoring data demonstrated for surface topography prediction in LPBF. Addit Manuf 2022;58:103075. https://doi.org/10.1016/j.addma.2022.103075.
[164] Hell SW, Weinreb RN. High resolution imaging in microscopy and ophthalmology: new frontiers in biomedical optics. Springer; 2019. https://doi.org/10.1007/978-3-030-16638-0_7.
[165] Huang D, Swanson EA, Lin CP, Schuman JS, Stinson WG, Chang W, et al. Optical coherence tomography. Science (80-) 1991;254:1178–81. https://doi.org/10.1126/science.1957169.
[166] Kanko JA, Sibley AP, Fraser JM. In situ morphology-based defect detection of selective laser melting through inline coherent imaging. J Mater Process Technol 2016;231:488–500. https://doi.org/10.1016/j.jmatprotec.2015.12.024.
[167] DePond PJ, Guss G, Ly S, Calta NP, Deane D, Khairallah S, et al. In situ measurements of layer roughness during laser powder bed fusion additive manufacturing using low coherence scanning interferometry. Mater Des 2018;154:347–59. https://doi.org/10.1016/j.matdes.2018.05.050.
[168] Hee MR, Puliafito CA, Wong C, Duker JS, Reichel E, Rutledge B, et al. Quantitative assessment of macular edema with optical coherence tomography. Arch Ophthalmol 1995;113:1019–29. https://doi.org/10.1001/archopht.1995.01100080071031.
[169] Hee MR, Puliafito CA, Duker JS, Reichel E, Coker JG, Wilkins JR, et al. Topography of diabetic macular edema with optical coherence tomography. Ophthalmology 1998;105:360–70. https://doi.org/10.1016/S0161-6420(98)93601-6.
[170] Chinn SR, Swanson EA, Fujimoto JG. Optical coherence tomography using a frequency-tunable optical source. Opt Lett 1997;22:340–2. https://doi.org/10.1364/ol.22.000340.
[171] Potsaid B, Gorczynska I, Srinivasan VJ, Chen Y, Jiang J, Cable A, et al. Ultrahigh speed spectral / Fourier domain OCT ophthalmic imaging at 70,000 to 312,500 axial scans per second. Opt Express 2008;16:15149–69. https://doi.org/10.1364/oe.16.015149.
[172] Leitgeb R, Hitzenberger C, Fercher A. Performance of fourier domain vs time domain optical coherence tomography. Opt Express 2003;11:889–94. https://doi.org/10.1364/oe.11.000889.
[173] Lough CS, Escano LI, Qu M, Smith CC, Landers RG, Bristow DA, et al. In-situ optical emission spectroscopy of selective laser melting. J Manuf Process 2020;53:336–41. https://doi.org/10.1016/j.jmapro.2020.02.016.
[174] Neef A, Seyda V, Herzog D, Emmelmann C, Schönleber M, Kogel-Hollacher M. Low coherence interferometry in selective laser melting. Phys Procedia 2014;56:82–9. https://doi.org/10.1016/j.phpro.2014.08.100.
[175] Fleming TG, Nestor SGL, Allen TR, Boukhaled MA, Smith NJ, Fraser JM. Tracking and controlling the morphology evolution of 3D powder-bed fusion in situ using inline coherent imaging. Addit Manuf 2020;32:100978. https://doi.org/10.1016/j.addma.2019.100978.
[176] Cullity BD, Stock SR. Elements of X-ray diffraction. 3rd ed. Prentice-Hall; 2001. https://doi.org/citeulike-article-id:3998040.
[177] Zhao C, Fezzaa K, Cunningham RW, Wen H, De Carlo F, Chen L, et al. Real-time monitoring of laser powder bed fusion process using high-speed X-ray imaging and diffraction. Sci Rep 2017;7:1–11. https://doi.org/10.1038/s41598-017-03761-2.
[178] Sinclair L, Leung CLA, Marussi S, Clark SJ, Chen Y, Olbinado MP, et al. In situ radiographic and ex situ tomographic analysis of pore interactions during multilayer builds in laser powder bed fusion. Addit Manuf 2020;36:101512. https://doi.org/10.1016/j.addma.2020.101512.
[179] Leung CLA, Marussi S, Atwood RC, Towrie M, Withers PJ, Lee PD. In situ X-ray imaging of defect and molten pool dynamics in laser additive manufacturing. Nat Commun 2018;9:1–9. https://doi.org/10.1038/s41467-018-03734-7.
[180] Calta NP, Wang J, Kiss AM, Martin AA, Depond PJ, Guss GM, et al. An instrument for in situ time-resolved X-ray imaging and diffraction of laser powder bed fusion additive manufacturing processes. Rev Sci Instrum 2018;89:055101. https://doi.org/10.1063/1.5017236.
[181] Calta NP, Martin AA, Hammons JA, Nielsen MH, Roehling TT, Fezzaa K, et al. Pressure dependence of the laser-metal interaction under laser powder bed fusion conditions probed by in situ X-ray imaging. Addit Manuf 2020;32:101084. https://doi.org/10.1016/j.addma.2020.101084.
[182] Lhuissier P, Bataillon X, Maestre C, Sijobert J, Cabrol E, Bertrand P, et al. In situ 3D X-ray microtomography of laser-based powder-bed fusion (L-PBF)—a feasibility study. Addit Manuf 2020;34:101271. https://doi.org/10.1016/j.addma.2020.101271.
[183] Gould B, Wolff S, Parab N, Zhao C, Lorenzo-Martin MC, Fezzaa K, et al. In situ analysis of laser powder bed fusion using simultaneous high-speed infrared and X-ray imaging. JOM 2021;73:201–11. https://doi.org/10.1007/s11837-020-04291-5.
[184] Martin AA, Calta NP, Khairallah SA, Wang J, Depond PJ, Fong AY, et al. Dynamics of pore formation during laser powder bed fusion additive manufacturing. Nat Commun 2019;10:1–10. https://doi.org/10.1038/s41467-019-10009-2.
[185] Guo Q, Zhao C, Qu M, Xiong L, Escano LI, Hojjatzadeh SMH, et al. In-situ characterization and quantification of melt pool variation under constant input energy density in laser powder bed fusion additive manufacturing process. Addit Manuf 2019;28:600–9. https://doi.org/10.1016/j.addma.2019.04.021.
[186] Chen Y, Clark SJ, Leung CLA, Sinclair L, Marussi S, Olbinado MP, et al. In-situ synchrotron imaging of keyhole mode multi-layer laser powder bed fusion additive manufacturing. Appl Mater Today 2020;20:100650. https://doi.org/10.1016/j.apmt.2020.100650.
[187] Bidare P, Maier RRJ, Beck RJ, Shephard JD, Moore AJ. An open-architecture metal powder bed fusion system for in-situ process measurements. Addit Manuf 2017;16:177–85. https://doi.org/10.1016/j.addma.2017.06.007.
[188] Vallejos JM, Barriobero-Vila P, Gussone J, Haubrich J, Kelm K, Stark A, et al. In situ high-energy synchrotron X-ray diffraction reveals the role of texture on the activation of slip and twinning during deformation of laser powder bed fusion Ti–6Al–4V. Adv Eng Mater 2021;23:20015556. https://doi.org/10.1002/adem.202001556.
[189] Choo H, Koehler MR, White LP, Ren Y, Morin D, Garlea E. Influence of defect characteristics on tensile deformation of an additively manufactured stainless steel: evolutions of texture and intergranular strain. Mater Sci Eng A 2020;791:139637. https://doi.org/10.1016/j.msea.2020.139637.
[190] Parab ND, Zhao C, Cunningham R, Escano LI, Fezzaa K, Everhart W, et al. Ultrafast X-ray imaging of laser–metal additive manufacturing processes. J Synchrotron Radiat 2018;25:1467–77. https://doi.org/10.1107/S1600577518009554.

[191] Sun T, Tan W, Chen L, Rollett A. In situ/operando synchrotron x-ray studies of metal additive manufacturing. MRS Bull 2020;45:927–33. https://doi.org/10.1557/mrs.2020.275.
[192] Voisin T, Calta NP, Khairallah SA, Forien JB, Balogh L, Cunningham RW, et al. Defects-dictated tensile properties of selective laser melted Ti-6Al-4V. Mater Des 2018;158:113–26. https://doi.org/10.1016/j.matdes.2018.08.004.
[193] Guo Q, Zhao C, Escano LI, Young Z, Xiong L, Fezzaa K, et al. Transient dynamics of powder spattering in laser powder bed fusion additive manufacturing process revealed by in-situ high-speed high-energy x-ray imaging. Acta Mater 2018;151:169–80. https://doi.org/10.1016/j.actamat.2018.03.036.
[194] Young ZA, Guo Q, Parab ND, Zhao C, Qu M, Escano LI, et al. Types of spatter and their features and formation mechanisms in laser powder bed fusion additive manufacturing process. Addit Manuf 2020;36:101438. https://doi.org/10.1016/j.addma.2020.101438.
[195] Leung CLA, Marussi S, Towrie M, Atwood RC, Withers PJ, Lee PD. The effect of powder oxidation on defect formation in laser additive manufacturing. Acta Mater 2019;166:294–305. https://doi.org/10.1016/j.actamat.2018.12.027.
[196] Young ZA, Coday MM, Guo Q, Qu M, Hojjatzadeh SMH, Escano LI, et al. Uncertainties induced by processing parameter variation in selective laser melting of Ti6Al4V revealed by in-situ X-ray imaging. Materials (Basel) 2022;15:530. https://doi.org/10.3390/ma15020530.
[197] Paulson NH, Gould B, Wolff SJ, Stan M, Greco AC. Correlations between thermal history and keyhole porosity in laser powder bed fusion. Addit Manuf 2020;34:101213. https://doi.org/10.1016/j.addma.2020.101213.
[198] Hojjatzadeh SMH, Parab ND, Yan W, Guo Q, Xiong L, Zhao C, et al. Pore elimination mechanisms during 3D printing of metals. Nat Commun 2019;10:1–8. https://doi.org/10.1038/s41467-019-10973-9.
[199] Guo Q, Zhao C, Qu M, Xiong L, Hojjatzadeh SMH, Escano LI, et al. In-situ full-field mapping of melt flow dynamics in laser metal additive manufacturing. Addit Manuf 2020;31:100939. https://doi.org/10.1016/j.addma.2019.100939.
[200] Bobel A, Hector LG, Chelladurai I, Sachdev AK, Brown T, Poling WA, et al. In situ synchrotron X-ray imaging of 4140 steel laser powder bed fusion. Materialia 2019;6:100306. https://doi.org/10.1016/j.mtla.2019.100306.
[201] Calta NP, Thampy V, Lee DRC, Martin AA, Ganeriwala R, Wang J, et al. Cooling dynamics of two titanium alloys during laser powder bed fusion probed with in situ X-ray imaging and diffraction. Mater Des 2020;195:108987. https://doi.org/10.1016/j.matdes.2020.108987.
[202] Hojjatzadeh SMH, Guo Q, Parab ND, Qu M, Escano LI, Fezzaa K, et al. In-situ characterization of pore formation dynamics in pulsed wave laser powder bed fusion. Materials (Basel) 2021;14:2936. https://doi.org/10.3390/ma14112936.
[203] Uhlmann E, Krohmer E, Schmeiser F, Schell N, Reimers W. A laser powder bed fusion system for in situ x-ray diffraction with high-energy synchrotron radiation. Rev Sci Instrum 2020;91:075104. https://doi.org/10.1063/1.5143766.
[204] Schmeiser F, Krohmer E, Schell N, Uhlmann E, Reimers W. Experimental observation of stress formation during selective laser melting using in situ X-ray diffraction. Addit Manuf 2020;32:101028. https://doi.org/10.1016/j.addma.2019.101028.
[205] Wakai Y, Ogura T, Suzuki S, Nakano S, Kajino S. In-situ observation of metal powder melting behavior using X-ray and thermal imaging. In: Proc. Int. Astronaut. Congr. IAC. 2019-Octob. International Astronautical Federation, IAF; 2019.
[206] Radovanović S, Annema AJ, Nauta B. A 3-Gb/s optical detector in standard CMOS for 850-nm optical communication. IEEE J Solid-State Circuits 2005;40:1706–17. https://doi.org/10.1109/JSSC.2005.852030.
[207] Fédéli JM, Virot L, Vivien L, Hartmann JM, Bogumilowicz Y, Marris-Morini D, et al. High-performance waveguide-integrated germanium PIN photodiodes for optical communication applications. In: 2014 7th Int. Silicon-Germanium Technol. Device Meet; 2014. p. 131–2. https://doi.org/10.1109/ISTDM.2014.6874690.
[208] Gilblom DL, Yoo SK, Ventura P. Operation and performance of a color image sensor with layered photodiodes. In: Infrared Technol Appl XXIX. 5074; 2003. p. 318–31. https://doi.org/10.1117/12.498557.
[209] Hunt CE, Carpenter A, Voss LF, Scott RC, Shao Q, Looker Q, et al. P-i-n high-speed photodiodes for X-ray and infrared imagers fabricated by in situ-doped APCVD germanium homoepitaxy. IEEE Trans Electron Devices 2020;67:3235–41. https://doi.org/10.1109/TED.2020.3006810.
[210] Nadipalli VK, Andersen SA, Nielsen JS, Pedersen DB. Considerations for interpreting in-situ photodiode sensor data in pulsed mode laser powder bed fusion. In: Proc Jt Spec Interes Gr Meet between Euspen ASPE Adv Precis Addit Manuf; 2019. p. 66–9.
[211] Bisht M, Ray N, Verbist F, Coeck S. Correlation of selective laser melting-melt pool events with the tensile properties of Ti-6Al-4V ELI processed by laser powder bed fusion. Addit Manuf 2018;22:302–6. https://doi.org/10.1016/j.addma.2018.05.004.
[212] Jayasinghe S, Paoletti P, Sutcliffe C, Dardis J, Jones N, Green PL. Automatic quality assessments of laser powder bed fusion builds from photodiode sensor measurements. Prog Addit Manuf 2022;7:143–60. https://doi.org/10.1007/s40964-021-00219-w.
[213] Egan DS, Ryan CM, Parnell AC, Dowling DP. Using in-situ process monitoring data to identify defective layers in Ti-6Al-4V additively manufactured porous biomaterials. J Manuf Process 2021;64:1248–54. https://doi.org/10.1016/j.jmapro.2021.03.002.
[214] Taherkhani K, Sheydaeian E, Eischer C, Otto M, Toyserkani E. Development of a defect-detection platform using photodiode signals collected from the melt pool of laser powder-bed fusion. Addit Manuf 2021;46:102152. https://doi.org/10.1016/J.ADDMA.2021.102152.
[215] Yavari R, Riensche A, Tekerek E, Jacquemetton L, Halliday H, Vandever M, et al. Digitally twinned additive manufacturing: detecting flaws in laser powder bed fusion by combining thermal simulations with in-situ meltpool sensor data. Mater Des 2021;211:110167. https://doi.org/10.1016/j.matdes.2021.110167.
[216] Schwerz C, Nyborg L. Linking in situ melt pool monitoring to melt pool size distributions and internal flaws in laser powder bed fusion. Metals (Basel) 2021;11:1856. https://doi.org/10.3390/met11111856.
[217] Taherkhani K, Eischer C, Toyserkani E. An unsupervised machine learning algorithm for in-situ defect-detection in laser powder-bed fusion. Manuf Process 2022;81:476–89. https://doi.org/10.1016/j.jmapro.2022.06.074.
[218] Coeck S, Bisht M, Plas J, Verbist F. Prediction of lack of fusion porosity in selective laser melting based on melt pool monitoring data. Addit Manuf 2018;25:347–56. https://doi.org/10.1016/j.addma.2018.11.015.
[219] Okaro IA, Jayasinghe S, Sutcliffe C, Black K, Paoletti P, Green PL. Automatic fault detection for laser powder-bed fusion using semi-supervised machine learning. Addit Manuf 2019;27:42–53. https://doi.org/10.1016/j.addma.2019.01.006.
[220] Zhang T, Zhou X, Zhang P, Duan Y, Cheng X, Wang X, et al. Hardness prediction of laser powder bed fusion product based on melt pool radiation intensity. Materials (Basel) 2022;15:1–15. https://doi.org/10.3390/ma15134674.
[221] Montazeri M, Nassar AR, Dunbar AJ, Rao P. In-process monitoring of porosity in additive manufacturing using optical emission spectroscopy. IISE Trans 2020;52:500–15. https://doi.org/10.1080/24725854.2019.1659525.
[222] Artzt K, Siggel M, Kleinert J, Riccius J, Requena G, Haubrich J. Pyrometric-based melt pool monitoring study of CuCr1Zr processed using L-PBF. Materials (Basel) 2020;13:1–22. https://doi.org/10.3390/ma13204626.
[223] Pandiyan V, Masinelli G, Claire N, Le-Quang T, Hamidi-Nasab M, de Formanoir C, et al. Deep learning-based monitoring of laser powder bed fusion process on variable time-scales using heterogeneous sensing and operando X-ray radiography guidance. Addit Manuf 2022;58:103007. https://doi.org/10.1016/J.ADDMA.2022.103007.
[224] Fu T, Tan P, Pang C, Zhao H, Shen Y. Fast fiber-optic multi-wavelength pyrometer. Rev Sci Instrum 2011;82:064902. https://doi.org/10.1063/1.3596567.
[225] Haines MP, Peter NJ, Babu SS, Jägle EA. In-situ synthesis of oxides by reactive process atmospheres during L-PBF of stainless steel. Addit Manuf 2020;33:101178. https://doi.org/10.1016/j.addma.2020.101178.
[226] Pavlov M, Doubenskaia M, Smurov I. Pyrometric analysis of thermal processes in SLM technology. Phys Procedia 2010;5:523–31. https://doi.org/10.1016/j.phpro.2010.08.080.
[227] Zouhri W, Dantan JY, Häfner B, Eschner N, Homri L, Lanza G, et al. Optical process monitoring for laser-powder bed fusion (L-PBF). CIRP J Manuf Sci Technol 2020;31. https://doi.org/10.1016/j.cirpj.2020.09.001.
[228] Renken V, von Freyberg A, Schünemann K, Pastors F, Fischer A. In-process closed-loop control for stabilising the melt pool temperature in selective laser melting. Prog Addit Manuf 2019;4:411–21. https://doi.org/10.1007/s40964-019-00083-9.
[229] Morris A, Langari R. Measurement and instrumentation. Third Edit. Academic Press; 2021.
[230] Herman I P. Optical diagnostics for thin film processing. Academic Press; 1996.
[231] Dixon J. Industrial radiation thermometry. Meas Control 1987;20:11–6. https://doi.org/10.1177/002029408702000603.
[232] Furumoto T, Ueda T, Kobayashi N, Yassin A, Hosokawa A, Abe S. Study on laser consolidation of metal powder with Yb:fiber laser-evaluation of line consolidation structure. J Mater Process Technol 2009;209:5973–80. https://doi.org/10.1016/j.jmatprotec.2009.07.017.
[233] Mitchell JA, Ivanoff TA, Dagel D, Madison JD, Jared B. Linking pyrometry to porosity in additively manufactured metals. Addit Manuf 2020;31:100946. https://doi.org/10.1016/j.addma.2019.100946.
[234] Smoqi Z, Gaikwad A, Bevans B, Kobir MH, Craig J, Abul-Haj A, et al. Monitoring and prediction of porosity in laser powder bed fusion using physics-informed meltpool signatures and machine learning. J Mater Process Technol 2022;304:117550. https://doi.org/10.1016/J.JMATPROTEC.2022.117550.
[235] Gutknecht K, Haferkamp L, Cloots M, Wegener K. Determining process stability of Laser Powder Bed Fusion using pyrometry. In: Procedia CIRP. 95. Elsevier B.V; 2020. p. 127–32. https://doi.org/10.1016/j.procir.2020.01.147.
[236] Francis J, Bian L. Deep learning for distortion prediction in laser-based additive manufacturing using big data. Manuf Lett 2019;20:10–4. https://doi.org/10.1016/j.mfglet.2019.02.001.
[237] Chivel Y. Optical in-process temperature monitoring of selective laser melting. Phys Procedia 2013;41:904–10. https://doi.org/10.1016/j.phpro.2013.03.165.
[238] Kozjek D, Carter FM, Porter C, Mogonye JE, Ehmann K, Cao J. Data-driven prediction of next-layer melt pool temperatures in laser powder bed fusion based on co-axial high-resolution Planck thermometry measurements. J Manuf Process 2022;79:81–90. https://doi.org/10.1016/J.JMAPRO.2022.04.033.
[239] Zhang B, Land WS, Ziegert J, Davies A. In situ monitoring of laser powder bed fusion additive manufacturing using digital fringe projection technique. In: Proc. - ASPE 2015 Spring Top. Meet. Achiev. Precis. Toler. Addit. Manuf. American Society for Precision Engineering, ASPE; 2015. p. 47–52.
[240] Zhang B, Ziegert J, Farahi F, Davies A. In situ surface topography of laser powder bed fusion using fringe projection. Addit Manuf 2016;12:100–7. https://doi.org/10.1016/j.addma.2016.08.001.
[241] Zhang B, Ziegert J, Davies A. In situ surface metrology of laser powder bed fusion processes using fringe projection. In: Proc. - ASPE/euspen 2016 Summer Top. Meet. Dimens. Accuracy Surf. Finish Addit. Manuf. American Society for Precision Engineering, ASPE; 2016. p. 119–24.

[242] Land WS, Zhang B, Ziegert J, Davies A. In-situ metrology system for laser powder bed fusion additive process. Procedia Manuf 2015;1:393–403. https://doi.org/10.1016/j.promfg.2015.09.047.
[243] Kalms M, Narita R, Thomy C, Vollertsen F, Bergmann RB. New approach to evaluate 3D laser printed parts in powder bed fusion-based additive manufacturing in-line within closed space. Addit Manuf 2019;26:161–5. https://doi.org/10.1016/j.addma.2019.01.011.
[244] Dickins A, Widjanarko T, Sims-Waterhouse D, Thompson A, Lawes S, Senin N, et al. Multi-view fringe projection system for surface topography measurement during metal powder bed fusion. J Opt Soc Am 2020;37:B93–105. https://doi.org/10.1364/josaa.396186.
[245] Dickins A, Widjanarko T, Lawes S, Stravroulakis P, Leach R. Design of a multi-sensor in-situ inspection system for additive manufacturing. In: Proc. -2018 ASPE euspen summer top. meet. adv. precis. addit. manuf; 2018. p. 248–52.
[246] Zhang H, Vallabh CKP, Xiong Y, Zhao X. A systematic study and framework of fringe projection profilometry with improved measurement performance for in-situ LPBF process monitoring. Measurement 2022;191:110796. https://doi.org/10.1016/J.MEASUREMENT.2022.110796.
[247] Barrett C, MacDonald E, Conner B, Persi F. Micron-level layer-wise surface profilometry to detect porosity defects in powder bed fusion of inconel 718. JOM 2018;70:1844–52. https://doi.org/10.1007/s11837-018-3025-7.
[248] Pedersen DB, Eiriksson ER, Aanaes H, Hansen HN. In-situ monitoring in additive manufacturing using contact image sensors. In: Proc. - ASPE/euspen 2016 summer top. meet. dimens. accuracy surf. finish addit. manuf; 2016. p. 114–8.
[249] Tan Phuc L, Seita M. A high-resolution and large field-of-view scanner for in-line characterization of powder bed defects during additive manufacturing. Mater Des 2019;164:107562. https://doi.org/10.1016/j.matdes.2018.107562.
[250] Fischer FG, Birk N, Rooney L, Jauer L, Schleifenbaum JH. Optical process monitoring in laser powder bed fusion using a recoater-based line camera. Addit Manuf 2021;47:102218.
[251] Fraden J. Handbook of Modern Sensors. Fourth. Springer; 2004. https://doi.org/10.1007/b97321.
[252] Kouprianoff D, Luwes N, Yadroitsava I. Acoustic emission technique for online detection of fusion defects for single tracks during metal laser powder bed fusion. In: Solid Free. Fabr. 2018 Proc. 29th Annu. Int. Solid Free. Fabr. Symp. - An Addit. Manuf. Conf. SFF 2018; 2020. p. 2087–96.
[253] Pandiyan V, Drissi-Daoudi R, Shevchik S, Masinelli G, Logé R, Wasmer K. Analysis of time, frequency and time-frequency domain features from acoustic emissions during Laser Powder-Bed fusion process. In: Procedia CIRP. 94. Elsevier B.V; 2020. p. 392–7. https://doi.org/10.1016/j.procir.2020.09.152.
[254] Pandiyan V, Drissi-Daoudi R, Shevchik S, Masinelli G, Le-Quang T, Logé R, et al. Deep transfer learning of additive manufacturing mechanisms across materials in metal-based laser powder bed fusion process. J Mater Process Technol 2022;303:117531. https://doi.org/10.1016/j.jmatprotec.2022.117531.
[255] Pandiyan V, Drissi-Daoudi R, Shevchik S, Masinelli G, Le-Quang T, Logé R, et al. Semi-supervised monitoring of laser powder bed fusion process based on acoustic emissions. Virtual Phys Prototyp 2021;16:481–97. https://doi.org/10.1080/17452759.2021.1966166.
[256] Rieder H, Dillhöfer A, Spies M, Bamberg J, Hess T. Online monitoring of additive manufacturing processes using ultrasound. In: Proc 11th Eur Conf Non-destructive Test. 1; 2014. p. 2194–201.
[257] Rieder H, Spies M, Bamberg J, Henkel B. On- and offline ultrasonic characterization of components built by SLM additive manufacturing. In: AIP conf. Proc. 1706; 2016, 130002. https://doi.org/10.1063/1.4940605.
[258] Park SH, Alnuaimi H, Hayes A, Sitkiewicz M, Amjad U, Muralidharan K, et al. Nonlinear acoustic technique for monitoring porosity in additively manufactured parts. J Nondestruct Eval Diagnostics Progn Eng Syst 2022;5. https://doi.org/10.1115/1.4053252.
[259] Eschner N, Weiser L, Häfner B, Lanza G. Classification of specimen density in laser powder bed fusion (L-PBF) using in-process structure-borne acoustic process emissions. Addit Manuf 2020;34:101324. https://doi.org/10.1016/j.addma.2020.101324.
[260] Eschner N, Weiser L, Häfner B, Lanza G. Development of an acoustic process monitoring system for selective laser melting (SLM). In: Solid Free. Fabr. 2018 Proc. 29th Annu. Int. Solid Free. Fabr. Symp. - An Addit. Manuf. Conf. SFF 2018; 2020. p. 13–5.
[261] Everton S, Dickens P, Tuck C, Dutton B. Using laser ultrasound to detect subsurface defects in metal laser powder bed fusion components. JOM 2018;70:378–83. https://doi.org/10.1007/s11837-017-2661-7.
[262] Everton SK, Dickens P, Tuck C, Dutton B. Identification of sub-surface defects in parts produced by additive manufacturing, using laser generated ultrasound. In: Mater. Sci. Technol. Conf. Exhib. 2016, MS T 2016. 1. Association for Iron and Steel Technology, AISTECH; 2016. p. 141–8.
[263] Everton S, Dickens P, Tuck C, Dutton B. Evaluation of laser ultrasonic testing for inspection of metal additive manufacturing. In: Laser 3D Manuf. II. 9353. SPIE; 2015. p. 145–52. https://doi.org/10.1117/12.2078768.
[264] Everton S, Dickens P, Tuck C, Dutton B, Wimpenny D. The use of laser ultrasound to detect defects in laser melted parts. In: TMS 2017 146th Annu. Meet. Exhib. Suppl. Proc. Cham: Springer; 2017. p. 105–16.
[265] Xu W, Li X, Zhang J. Multi-feature fusion imaging via machine learning for laser ultrasonic based defect detection in selective laser melting part. Opt Laser Technol 2022;150. https://doi.org/10.1016/j.optlastec.2022.107918.
[266] Shevchik SA, Kenel C, Leinenbach C, Wasmer K. Acoustic emission for in situ quality monitoring in additive manufacturing using spectral convolutional neural networks. Addit Manuf 2018;21:598–604. https://doi.org/10.1016/j.addma.2017.11.012.
[267] Wasmer K, Le-Quang T, Meylan B, Shevchik SA. In situ quality monitoring in AM using acoustic emission: a reinforcement learning approach. J Mater Eng Perform 2019;28:666–72. https://doi.org/10.1007/s11665-018-3690-2.
[268] Wasmer K, Kenel C, Leinenbach C, Shevchik SA. In situ and real-time monitoring of powder-bed AM by combining acoustic emission and artificial intelligence. In: Ind. Addit. Manuf. - Proc. Addit. Manuf. Prod. Appl. - AMPA2017. Cham: Springer; 2017. p. 200–9.
[269] Smith RJ, Li W, Coulson J, Clark M, Somekh MG, Sharples SD. Spatially resolved acoustic spectroscopy for rapid imaging of material microstructure and grain orientation. Meas Sci Technol 2014;25:055902. https://doi.org/10.1088/0957-0233/25/5/055902.
[270] Smith RJ, Hirsch M, Patel R, Li W, Clare AT, Sharples SD. Spatially resolved acoustic spectroscopy for selective laser melting. J Mater Process Technol 2016;236:93–102. https://doi.org/10.1016/j.jmatprotec.2016.05.005.
[271] Dryburgh P, Patel R, Pieris DM, Hirsch M, Li W, Sharples SD, et al. Spatially resolved acoustic spectroscopy for texture imaging in powder bed fusion nickel superalloys. In: AIP Conf. Proc., vol. 2102. AIP Publishing LLC; 2019, 020004. https://doi.org/10.1063/1.5099708.
[272] Hirsch M, Dryburgh P, Catchpole-Smith S, Patel R, Parry L, Sharples SD, et al. Targeted rework strategies for powder bed additive manufacture. Addit Manuf 2018;19:127–33. https://doi.org/10.1016/j.addma.2017.11.011.
[273] Williams J, Dryburgh P, Clare A, Rao P, Samal A. Defect detection and monitoring in metal additive manufactured parts through deep learning of spatially resolved acoustic spectroscopy signals. Smart Sustain Manuf Syst 2018;2:204–26. https://doi.org/10.1520/SSMS20180035.
[274] Zhang JXJ, Hoshino K. Mechanical transducers: cantilevers, acoustic wave sensors, and thermal sensors. Mol Sens Nanodevices 2019:311–412. https://doi.org/10.1016/b978-0-12-814862-4.00006-5.
[275] Slotwinski JA, Garboczi EJ, Hebenstreit KM. Porosity measurements and analysis for metal additive manufacturing process control. J Res Natl Inst Stand Technol 2014;119:494. https://doi.org/10.6028/jres.119.019.
[276] Islam T, Mukhopadhyay SC, Suryadevara NK. Smart sensors and internet of things: a postgraduate paper. IEEE Sens J 2017;17:577–84. https://doi.org/10.1109/JSEN.2016.2630124.
[277] Welch AJ, MJC Van Gemert. Optical-thermal response of laser-irradiated tissue. 2011. https://doi.org/10.1007/978-90-481-8831-4.
[278] Dunbar AJ. Analysis of the laser powder bed fusion additive manufacturing process through experimental measurement and finite element modeling. Thesis Pennsylvania State Univ 2016.
[279] Van Belle L, Vansteenkiste G, Boyer JC. Investigation of residual stresses induced during the selective laser melting process. Key Eng Mater 2013;554:1828–34. https://doi.org/10.4028/www.scientific.net/KEM.554-557.1828.
[280] Omron Corporation. Displacement sensor technical guide. Omron Corp; 2017. https://assets.omron.eu/downloads/manual/en/q257_displacement_sensor_technical_manual_en.pdf.
[281] Biegler M, Marko A, Graf B, Rethmeier M. Finite element analysis of in-situ distortion and bulging for an arbitrarily curved additive manufacturing directed energy deposition geometry. Addit Manuf 2018;24:264–72. https://doi.org/10.1016/j.addma.2018.10.006.
[282] Biegler M, Graf B, Rethmeier M. Assessing the predictive capability of numerical additive manufacturing simulations via in-situ distortion measurements on a LMD component during build-up. Procedia CIRP 2018;74:158–62. https://doi.org/10.1016/j.procir.2018.08.069.
[283] Williams RJ, Davies CM, Hooper PA. In situ monitoring of the layer height in laser powder bed fusion. Mater Des Process Commun 2021;3:e173. https://doi.org/10.1002/mdp2.173.
[284] Havermann D, Mathew J, MacPherson WN, Maier RRJ, Hand DP. Temperature and strain measurements with Fiber Bragg gratings embedded in stainless steel 316. J Light Technol 2015;33:2474–9. https://doi.org/10.1109/JLT.2014.2366835.
[285] Hehr A, Norfolk M, Kominsky D, Boulanger A, Davis M, Boulware P. Smart build-plate for metal additive manufacturing processes. Sensors (Switzerland) 2020;20:360. https://doi.org/10.3390/s20020360.
[286] Liu R, Vogt BD, Yang H. Gaussian process monitoring of layerwise-dependent imaging data. IEEE Robot Autom Lett 2021;6:8029–36. https://doi.org/10.1109/LRA.2021.3102625.
[287] Zhirnov I, Panahi N, Åsberg M, Krakhmalev P. Process quality assessment with imaging and acoustic monitoring during laser powder bed fusion. Procedia CIRP 2022;111:363–7. https://doi.org/10.1016/J.PROCIR.2022.08.167.
[288] Drissi-Daoudi R, Pandiyan V, Logé R, Shevchik S, Masinelli G, Ghasemi-Tabasi H, et al. Differentiation of materials and laser powder bed fusion processing regimes from airborne acoustic emission combined with machine learning. Virtual Phys Prototyp 2022;17. https://doi.org/10.1080/17452759.2022.2028380.
[289] Fuchs L, Eischer C. In-process monitoring systems for metal additive manufacturing. In: EOS White Pap; 2018. p. 1–20. https://www.semanticscholar.org/paper/In-process-monitoring-systems-for-metal-additive-Fuchs-Eischer/0b4a7bbeff6c2faec5d67c0f0c23a47bf2f45991.
[290] SLM Solution. Melt Pool Monitoring (MPM) System by SLM Solutions. Report1; 2016. https://pdf.aeroexpo.online/pdf/slm-solutions-gmbh/melt-pool-monitoring-mpm/170578-4425.html.
[291] SLM Solution. Laser power monitoring. Report n.d.:1–2. https://www.slm-solutions.com/fileadmin/user_upload/downloads/de/603xx171025-01-001-lpm_web.pdf.
[292] SLM Solution. Large format selective laser melting. Report n.d.:6. https://www.slm-solutions.com/fileadmin/Content/Machines/SLM_R_800_Web.pdf.

[293] ConceptLaser. Achieve the highest possible quality in series production thanks to LaserCUSING ®. Report. 2015. p. 1–4. https://www.concept-laser.de/fileadmin/user_upload/1603_QM_Prospect_EN.pdf.
[294] Renishaw. InfiniAM spectral – energy input and melt pool emissions monitoring for AM systems. Report. 2017. p. 1–5. http://resources.renishaw.com/en/details/data-sheet-renam-500q–99032.
[295] Trumpf. Monitoring TruPrint. Report n.d. https://www.trumpf.com/en_CA/products/services/services-machines-systems-and-lasers/monitoring-analysis/monitoring-truprint/.
[296] Sigma Additive Solutions. PrintRite3D INSPECT. Report n.d.:1. https://sigmalabsinc.com/wp-content/uploads/2018/10/Sigma-Labs-PrintRite3D-INSPECT-2.pdf.
[297] Solutions SA. PRINTRITE3D® CONTOURTM. Report n.d. https://pdf.directindustry.com/pdf/sigma-labs/printrite3d-contour/197081-750853.html.
[298] Stratonics I. ThermaViz®: the innovative two-wavelength imaging pyrometer. Report. 2015. p. 1–16. http://stratonics.com/wp-content/uploads/2016/03/ThermaViz-Operating-Manual-2015.04.03.pdf.
[299] Harbig J, Wenzler DL, Baehr S, Kick MK, Merschroth H, Wimmer A, et al. Methodology to determine melt Pool anomalies in powder bed fusion of metals using a laser beam by means of process monitoring and sensor data fusion. Materials (Basel) 2022;15:1265. https://doi.org/10.3390/ma15031265.
[300] Ren YM, Zhang Y, Ding Y, Wang Y, Christofides PD. Computational fluid dynamics-based in-situ sensor analytics of direct metal laser solidification process using machine learning143; 2020. p. 107069.
[301] Yadav P, Singh VK, Joffre T, Rigo O, Arvieu C, Le Guen E, et al. Inline drift detection using monitoring systems and machine learning in selective laser melting. Adv Eng Mater 2020;22:2000660. https://doi.org/10.1002/adem.202000660.
[302] Gobert C, Arrieta E, Belmontes A, Wicker RB, Medina F, McWilliams B. Conditional generative adversarial networks for in-situ layerwise additive manufacturing data. In: Solid Free. Fabr. 2019 Proc. 30th Annu. Int. Solid Free. Fabr. Symp. - An Addit. Manuf. Conf. SFF 2019, University of Texas at Austin; 2019. p. 192–201.
[303] Höfflin D, Rosilius M, Seitz P, Schiffler A, Hartmann J. Opto-thermal investigation of additively manufactured steel samples as a function of the hatch distance. Sensors 2022;22:46. https://doi.org/10.3390/s22010046.
[304] Dursun G, Pehlivanogullari B, Sen C, Orhangul A. An investigation upon overhang zones by using finite element modelling and in-situ monitoring systems. Procedia CIRP 2020;93:1253–8. https://doi.org/10.1016/j.procir.2020.04.118.
[305] Pauzon C, Mishurova T, Fischer M, Ahlström J, Fritsch T, Bruno G, et al. Impact of contour scanning and helium-rich process gas on performances of alloy 718 lattices produced by laser powder bed fusion. Mater Des 2022;215:110501.
[306] Artzt K, Mishurova T, Bauer PP, Gussone J, Barriobero-Vila P, Evsevleev S, et al. Pandora's box-influence of contour parameters on roughness and subsurface residual stresses in laser powder bed fusion of Ti-6Al-4V. Materials (Basel) 2020;13:3348. https://doi.org/10.3390/ma13153348.
[307] Alberts D, Schwarze D, Witt G. In situ melt pool monitoring and the correlation to part density of Inconel® 718 for quality assurance in selective laser melting. In: 2017 Int. Solid Free. Fabr. Symp., University of Texas at Austin; 2020. p. 1481–94.
[308] Ansari MA, Crampton A, Garrard R, Cai B, Attallah M. A convolutional neural network (CNN) classification to identify the presence of pores in powder bed fusion images. Int J Adv Manuf Technol 2022;120:5133–50. https://doi.org/10.1007/s00170-022-08995-7.
[309] Lapointe S, Guss G, Reese Z, Strantza M, Matthews MJ, Druzgalski CL. Photodiode-based machine learning for optimization of laser powder bed fusion parameters in complex geometries. Addit Manuf 2022;53:102687. https://doi.org/10.1016/J.ADDMA.2022.102687.
[310] Klein J, Jaretzki M, Schwarzenberger M, Ihlenfeldt S, Drossel WG. Automated porosity assessment of parts produced by laser powder bed fusion using convolutional neural networks. Procedia CIRP 2021;104:1434–9. https://doi.org/10.1016/j.procir.2021.11.242.
[311] Toeppel T, Schumann P, Ebert M-C, Bokkes T, Funke K, Werner M, et al. 3D analysis in laser beam melting based on real-time process monitoring. In: Mater Sci Technol Conf Exhib 2016, MS T 2016. 1; 2016. p. 123–32.
[312] O'Loughlin S, Dutton B, Semaj G, Snell E, Rindler J, Groeber MA. Towards in-process prediction of voids in laser powder bed fusion. JOM 2021;73:3240–9. https://doi.org/10.1007/s11837-021-04885-7.
[313] Boos E, Schwarzenberger M, Jaretzki M. Melt Pool monitoring using fuzzy based anomaly detection in laser beam melting. Proc Met Addit Manuf Conf Örebro, Sweden 2020:1–11.
[314] Egan DS, Dowling DP. Influence of process parameters on the correlation between in-situ process monitoring data and the mechanical properties of Ti-6Al-4V non-stochastic cellular structures. Addit Manuf 2019;30. https://doi.org/10.1016/j.addma.2019.100890.
[315] Liu X, Mileo A. A deep learning approach to defect detection in additive manufacturing of titanium alloys. In: Proc. 32nd Annu. Int. Solid Free. Fabr. Symp., University of Texas at Austin; 2021. p. 423–36.
[316] Keaveney S, Shmeliov A, Nicolosi V, Dowling DP. Investigation of process by-products during the selective laser melting of Ti6AL4V powder. Addit Manuf 2020;36:101514. https://doi.org/10.1016/j.addma.2020.101514.
[317] Belloli F, Demir AG, Previtali B. Understanding the deformation mechanisms of horizontal internal channels during the LPBF of 18Ni300 maraging steel. J Manuf Process 2021;71:237–48. https://doi.org/10.1016/j.jmapro.2021.07.063.
[318] Colosimo BM, Garghetti F, Pagani L, Grasso M. A novel method for in-process inspection of lattice structures via in-situ layerwise imaging. Manuf Lett 2022;32:67–72. https://doi.org/10.1016/J.MFGLET.2022.03.004.
[319] Donegan SP, Schwalbach EJ, Groeber MA. Multimodal registration and fusion of in situ and ex situ metal additive manufacturing data. JOM 2021;73:3250–62. https://doi.org/10.1007/s11837-021-04883-9.
[320] Megahed M, Mindt HW, Willems J, Dionne P, Jacquemetton L, Craig J, et al. LPBF right the first time—the right mix between modeling and experiments. Integr Mater Manuf Innov 2019;8:194–216. https://doi.org/10.1007/s40192-019-00133-8.
[321] Karayagiz K, Elwany A, Tapia G, Franco B, Johnson L, Ma J, et al. Numerical and experimental analysis of heat distribution in the laser powder bed fusion of Ti-6Al-4V. IISE Trans 2019;51:136–52. https://doi.org/10.1080/24725854.2018.1461964.
[322] Lott P, Schleifenbaum H, Meiners W, Wissenbach K, Hinke C, Bültmann J. Design of an optical system for the in situ process monitoring of selective laser melting (SLM). Phys Procedia 2011;12:683–90. https://doi.org/10.1016/j.phpro.2011.03.085.
[323] Grasso M, Colosimo BM. A statistical learning method for image-based monitoring of the plume signature in laser powder bed fusion. Robot Comput Integr Manuf 2019;57:103–15. https://doi.org/10.1016/j.rcim.2018.11.007.
[324] DeCost BL, Jain H, Rollett AD, Holm EA. Computer vision and machine learning for autonomous characterization of AM powder feedstocks. JOM 2017;69:456–65. https://doi.org/10.1007/s11837-016-2226-1.
[325] Bao H, Wu S, Wu Z, Kang G, Peng X, Withers PJ. A machine-learning fatigue life prediction approach of additively manufactured metals. Eng Fract Mech 2021;242:107508. https://doi.org/10.1016/j.engfracmech.2020.107508.
[326] Ertay DS, Kamyab S, Vlasea M, Azimifar Z, Ma T, Rogalsky AD, et al. Toward subsurface pore prediction capabilities for laser powder bed fusion using data science. J Manuf Sci Eng 2021;143:071016. https://doi.org/10.1115/1.4050461.
[327] Zhang Y, Yang S, Dong G, Zhao YF. Predictive manufacturability assessment system for laser powder bed fusion based on a hybrid machine learning model. Addit Manuf 2021;41:101946. https://doi.org/10.1016/j.addma.2021.101946.
[328] Zhang M, Sun CN, Zhang X, Goh PC, Wei J, Hardacre D, et al. High cycle fatigue life prediction of laser additive manufactured stainless steel: a machine learning approach. Int J Fatigue 2019;128:105194. https://doi.org/10.1016/j.ijfatigue.2019.105194.
[329] Shalev-Shwartz S, Ben-David S. Understanding machine learning: from theory to algorithms. Cambridge University Press; 2014. https://doi.org/10.1017/CBO9781107298019.
[330] Goodfellow Ian, Bengio Yoshua, AC. Deep Learning - Ian Goodfellow, Yoshua Bengio. Aaron Courville: Google Books; 2016.
[331] Alzubaidi L, Zhang J, Humaidi AJ, Al-Dujaili A, Duan Y, Al-Shamma O, et al. Review of deep learning: concepts, CNN architectures, challenges, applications, future directions. J Big Data 2021;8. https://doi.org/10.1186/s40537-021-00444-8.
[332] Karaboga D, Kaya E. Adaptive network based fuzzy inference system (ANFIS) training approaches: a comprehensive survey. Artif Intell Rev 2019;52:2263–93. https://doi.org/10.1007/s10462-017-9610-2.
[333] Vassilopoulos AP, Bedi R. Adaptive neuro-fuzzy inference system in modelling fatigue life of multidirectional composite laminates. Comput Mater Sci 2008;43:1086–93. https://doi.org/10.1016/j.commatsci.2008.02.028.
[334] Kramer O. Dimensionality reduction with unsupervised nearest neighbors. Springer; 2013. https://doi.org/10.1007/978-3-642-38652-7.
[335] Belgiu M, Drăgu L. Random forest in remote sensing: a review of applications and future directions. ISPRS J Photogramm Remote Sens 2016;114. https://doi.org/10.1016/j.isprsjprs.2016.01.011.
[336] Bishop CM, Saxe AM, McClelland JL, Ganguli S, Pedregosa F, Varoquaux G, et al. Scikit-learn: machine learning in {P}ython. J Mach Learn Res 2011;12:2825–30.
[337] Meng L, Zhang J. Process design of laser powder bed fusion of stainless steel using a Gaussian process-based machine learning model. JOM 2020;72:420–8. https://doi.org/10.1007/s11837-019-03792-2.
[338] Tapia G, Khairallah S, Matthews M, King WE, Elwany A. Gaussian process-based surrogate modeling framework for process planning in laser powder-bed fusion additive manufacturing of 316L stainless steel. Int J Adv Manuf Technol 2018;94:3591–603. https://doi.org/10.1007/s00170-017-1045-z.
[339] Kamath C. Data mining and statistical inference in selective laser melting. Int J Adv Manuf Technol 2016;86:1659–77. https://doi.org/10.1007/s00170-015-8289-2.
[340] Tapia G, Elwany AH, Sang H. Prediction of porosity in metal-based additive manufacturing using spatial Gaussian process models. Addit Manuf 2016;12:282–90. https://doi.org/10.1016/j.addma.2016.05.009.
[341] Murphy KP. Machine learning: A probabilistic perspective (adaptive computation and machine learning series). MIT Press; 2012.
[342] He K, Zhang X, Ren S, Sun J. Deep residual learning for image recognition. In: Proc. IEEE Comput. Soc. Conf. Comput. Vis. Pattern Recognit; 2016. p. 770–8. https://doi.org/10.1109/CVPR.2016.90.
[343] Huang G, Liu Z, Van Der Maaten L, Weinberger KQ. Densely connected convolutional networks. In: Proc. - 30th IEEE Conf. Comput. Vis. Pattern Recognition, CVPR 2017; 2017. p. 4700–8. https://doi.org/10.1109/CVPR.2017.243.
[344] Grasso M, Colosimo BM. Process defects and in situ monitoring methods in metal powder bed fusion: a review. Meas Sci Technol 2017;28:044005. https://doi.org/10.1088/1361-6501/aa5c4f.
[345] Nielsen F. Hierarchical clustering BT - introduction to HPC with MPI for data science. Springer: Springer; 2016 [p. 195–211].
[346] Self Organizing Maps - Applications and Novel Algorithm Design. 2012. doi:10.5772/566.
[347] Smith LI. A tutorial on principal components analysis introduction. 2002.

[348] Hopcroft J, Kannan R. Computer science theory for the information age. In: Markov Chains. Introd. to Queueing Syst. with Telecommun. Appl; 2012. p. 93–177.
[349] Van Otterlo M, Wiering M. Reinforcement learning and markov decision processes. Adapt Learn Optim 2012;12:3–42. https://doi.org/10.1007/978-3-642-27645-3_1.
[350] Sutton RS, Barto AG. Reinforcement learning: an introduction (2nd edition 2018). MIT Press; 2018.
[351] Hou ZJ, Wang Q, Zhao CG, Zheng J, Tian JM, Ge XH, et al. Online monitoring technology of metal powder bed fusion processes: a review. Materials (Basel) 2022;15. https://doi.org/10.3390/ma15217598.
[352] Grasso M, Remani A, Dickins A, Colosimo BM, Leach RK. In-situ measurement and monitoring methods for metal powder bed fusion: an updated review. Meas Sci Technol 2021;32. https://doi.org/10.1088/1361-6501/ac0b6b.
[353] Chua CK, Wong CH, Yeong WY. Standards, quality control, and measurement sciences in 3D printing and additive manufacturing. 2017.
[354] Gutknecht K, Cloots M, Sommerhuber R, Wegener K. Mutual comparison of acoustic, pyrometric and thermographic laser powder bed fusion monitoring. Mater Des 2021;210:110036. https://doi.org/10.1016/j.matdes.2021.110036.
[355] Ellis G. Control system design guide. Fourth Edi 2012. https://doi.org/10.1016/B978-0-12-385920-4.01001-8.
[356] Wang M, Zhang Q, Li Q, Wu Z, Chen C, Xu J, et al. Research on morphology detection of metal additive manufacturing process based on fringe projection and binocular vision. Appl Sci 2022;12. https://doi.org/10.3390/app12189232.
[357] Liu Y, Blunt L, Gao F, Jiang X. A simple calibration method for a fringe projection system embedded within an additive manufacturing machine. Machines 2021;9. https://doi.org/10.3390/machines9090200.
[358] Pineda J, Marrugo AG, Romero LA. Developing a robust acquisition system for fringe projection profilometry. J Phys Conf Ser 2019;1247. https://doi.org/10.1088/1742-6596/1247/1/012053.
[359] Tempelman JR, Wachtor AJ, Flynn EB, Depond PJ, Forien JB, Guss GM, et al. Sensor fusion of pyrometry and acoustic measurements for localized keyhole pore identification in laser powder bed fusion. J Mater Process Technol 2022;308. https://doi.org/10.1016/j.jmatprotec.2022.117656.
[360] Fung ML, Chen MZQ, Chen YH. Sensor fusion: a review of methods and applications. In: Proc. 29th Chinese Control Decis. Conf. CCDC 2017; 2017. https://doi.org/10.1109/CCDC.2017.7979175.
[361] Petrich J, Snow Z, Corbin D, Reutzel EW. Multi-modal sensor fusion with machine learning for data-driven process monitoring for additive manufacturing. Addit Manuf 2021;48. https://doi.org/10.1016/j.addma.2021.102364.
[362] Kotsiantis SB, Sotiris B, Zaharakis I, Pintelas P. Supervised machine learning: a review of classification techniques. Emerg Artif Intell Appl Comput Eng 2007;160: 3–24. https://doi.org/10.31449/inf.v31i3.148.
[363] Gallo C. Artificial neural networks tutorial. In: Encycl. Inf. Sci. Technol. 3rd ed. 2014. p. 6369–78. https://doi.org/10.4018/978-1-4666-5888-2.ch626.
[364] Pham DT, Dimov SS, Nguyen CD. Selection of K in K-means clustering. Proc Inst Mech Eng Part C J Mech Eng Sci 2005;219:103–19. https://doi.org/10.1243/095440605X8298.
[365] Schubert E, Sander J, Ester M, Kriegel HP, Xu X. DBSCAN revisited, revisited: why and how you should (still) use DBSCAN. ACM Trans Database Syst 2017;42. https://doi.org/10.1145/3068335.
[366] Kamimura R. Information-theoretic approach to interpret internal representations of self-organizing maps. Self Organ Maps - Appl Nov Algorithm Des 2011. https://doi.org/10.5772/13272.
[367] Gewers FL, Ferreira GR, De Arruda HF, Silva FN, Comin CH, Amancio DR, et al. Principal component analysis: a natural approach to data exploration. ACM Comput Surv 2021;54. https://doi.org/10.1145/3447755.
[368] Nan Wang H, Liu N, Yun Zhang Y, Wei Feng D, Huang F, Sheng Li D, et al. Deep reinforcement learning: a survey. Front Inf Technol Electron Eng 2020;21: 1726–44. https://doi.org/10.1631/FITEE.1900533.
[369] Vallabh CKP, Zhao X. Continuous comprehensive monitoring of melt pool morphology under realistic printing scenarios with laser powder bed fusion. 3D Print Addit Manuf 2021. https://doi.org/10.1089/3dp.2021.0060.
[370] Reijonen J, Revuelta A, Riipinen T, Ruusuvuori K, Puukko P. On the effect of shielding gas flow on porosity and melt pool geometry in laser powder bed fusion additive manufacturing. Addit Manuf 2020;32:101030. https://doi.org/10.1016/j.addma.2019.101030.
[371] Ferrar B, Mullen L, Jones E, Stamp R, Sutcliffe CJ. Gas flow effects on selective laser melting (SLM) manufacturing performance. J Mater Process Technol 2012; 212. https://doi.org/10.1016/j.jmatprotec.2011.09.020.
[372] Deng J, Dong W, Socher R, Li L-J, Li Kai, Fei-Fei Li. ImageNet: a large-scale hierarchical image database. 2010. https://doi.org/10.1109/cvpr.2009.5206848.